GENERATION OF SPIN CURRENT AND MANIPULATION OF MAGNETIC MOMENT IN MAGNETIC THIN FILM HETEROSTRUCTURES

A Dissertation

Presented to the Faculty of the Graduate School

of Cornell University

In Partial Fulfillment of the Requirements for the Degree of

Doctor of Philosophy

by

Yongxi Ou

August 2018

GENERATION OF SPIN CURRENT AND MANIPULATION OF MAGNETIC MOMENT IN THIN FILM HETEROSTRUCTURES

Yongxi Ou, Ph. D.

Cornell University 2018

In this thesis, I summarize my research on the generation of spin current via the spin Hall effect (SHE) in various material systems, the behaviors of the spin-orbit torques (SOTs) which result from the injection of spin current into an adjacent ferromagnet (FM) in the thin film heterostructures under different interfacial and ambient conditions, the engineering of perpendicular magnetic anisotropy (PMA) at the FM/oxide interface, and how to use this effect together with the large SOTs to manipulate the magnetic moment in magnetic tunnel junctions (MTJs). Accordingly, the thesis consists of four sections for the experimental details regarding the above aspects.

In the first study, I focused on the behavior of the SOTs generated in normal metal (NM)/FM/oxide heterostructures under different interfacial and ambient conditions. By varying the spin current sources and controlling the different interfaces, the strength of the SOTs can be efficiently modified, pointing out the physical origins and mechanism of the generation and transfer of these SOTs in the NM/FM/oxide heterostructures.

In the second study, I explored the SHE in various material systems beyond conventional heavy metals. These material systems include antiferromagnetic alloys

and ferromagnetic alloys near the magnetic transition temperatures. By employing spin torque ferromagnetic resonance and the harmonic response technique, I was able to quantify the strength of the SHE in those material systems under both room temperature and low temperature ambient conditions.

In the third part, I explained the discovery and manipulation of the PMA at the FM/oxide interface by inserting an ultrathin metallic dusting layer. I demonstrated that with this dusting technique, the PMA can be greatly enhanced and efficiently modified by the types of the dusting material, the amount of that material, and the post-fabrication process involving the dusting layer.

In the last part, I showed that by combing the strong SHE in the heavy metal tungsten (W) and the PMA effect from the dusting technique, MTJs with fast, reliable switching and low switching current can be realized in three-terminal nanoscale devices, demonstrating their great potential as a building block for the next generation memory storage elements.

BIOGRAPHICAL SKETCH

Yongxi Ou was born in Guangzhou, Guangdong Province in China in 1988. He received his elementary and high school education in the city of Dongguan after his family moved to that city when he was young. Later he got admitted to Peking University and studied as an undergraduate student majoring in physics in Beijing. He spent his junior year in the research group of Prof. Dapeng Yu doing research on the field emission from graphene and his senior year in the group of Prof. Jian Wang where he learned the basic knowledge of topological insulator. After receiving the bachelor's degree from Peking University in 2012, Yongxi continued to pursue physics study overseas and was admitted to the graduate program in the physics department in Cornell University. After the first year serving as a teaching assistant in Cornell, he joined as a research assistant in Prof. Robert Buhrman's group where he spent five years doing research on magnetics and spintronics. After receiving his PhD degree and graduating from Cornell in 2018, Yongxi will continue his academia career as a postdoc.

To my mother.

ACKNOWLEDGMENTS

First of all, I would like to thank my advisor Prof. Bob Buhrman. Since I entered the research group in the summer of 2013, Bob has given me countless supports and instructions for both the scientific research and various aspects in my personal life. In Bob's lab, his hands-off style provides the students enough freedom to explore the interesting topics in the cutting-edge applied physics research. At the same time, Bob inspires me with his rich experience and sharp intuition in research, which always guides me in my own physics study as well. Without doubt, I will continue to benefit from Bob's wisdom in a number of aspects in my future career.

I would like to thank Prof. Dan Ralph, who has given me many important and invaluable advices during my graduate study and in our many times' collaborations. I always admire Dan's careful and strict thinking in research. His intelligent and intuitive viewpoints in physics are truly inspiring as which I would expect and learn from an excellent physicist.

I am also grateful to Prof. Erich Mueller for serving as my special committee member. I have been impressed by Erich's style on how to consider a specific physical question and how to relate it to the knowledge background I already have. During my A exam preparation, his inspiring questions and discussions taught me how to think as an independent researcher.

I also owe great thanks to many former members in Buhrman group. Yun Li was my mentor when I joined the group. She patiently showed me how to carry out important

experiments in our study. Though she graduated soon, I still thank her supports at the beginning of my graduate research. Junbo Park was always helpful and I learned a lot from him as the manager of one of our important lab facilities, ion mill, of which I became the successor manager as well. He was a sincere friend in life and I enjoyed spending time with him chatting with topics about Asian cultures. Praveen Gowtham impressed me with his broad knowledge and it was an enjoyable experience discussing research with him. Graham Rowland worked as a postdoc in Buhrman group and he was extremely intelligent in programing and research. We, including me, still benefit from his well-written measurement programs on various setups in the lab today. Graham was also very friendly and he was always willing to help when I encountered issues in my measurements. Luis Henrique Vilela Leão and Sriharsha Aradhya were also postdocs in the group. Luis's intelligence in deriving equations and formulas, and Sri's diligent attitude toward research were inspiring to me. Their carefree personality also made them great friends. Minh-Hai Nguyen joined the group at the same time as me, and we have spent many memorable moments during our graduate study both as friends and colleagues.

I want to thank Chi-Feng Pai specially. Although he is much senior to me, Chi-Feng always treated me frankly and sincerely. We shared many similar ideas in research and he gave me supports many times. Outside of research, we enjoyed discussing numerous topics on cultures and life. He is a great friend to me and I will continue to cherish our friendship in the future.

I should also thank the current group members in Buhrman group. Shengjie Shi and I were admitted to Cornell from China at the same year as graduate students. We have been friends since then and our relationship has become deeper since he joined Buhrman group. Shengjie is an extremely kind and calm person and I am grateful to share my graduate life studying with him. Ryan Tapping is a junior graduate student. We spent a lot of time together performing experiments and he is a very helpful research assistant. I learnt a lot from him about western culture. The two postdocs, Lijun Zhu and Arnab Bose, are also helpful for their valuable comments in research and in the daily managements of our lab.

I would also like to express my thanks to members in Prof. Dan Ralph's group, including Colin Jermain who was very friendly to chat with, Greg Stiehl who gave me valuable suggestions and Neal Reynolds who helped me a lot during low temperature ferromagnetic resonance experiments.

Finally, I would like to thank my family. Through my graduate years, their trust and spiritual supports helped me overcome the difficulties again and again in my research and life.

TABLE OF CONTENTS

LIST OF FIGURES

CHAPTER 1

INTRODUCTION

In this chapter, I will first discuss some basic background for the spin generation using transport methods in the magnetic thin film heterostructures utilizing the spin filter effect and the spin-orbit coupling effect. Then I will provide some discussion on the phenomena of spin transfer torque. Lastly, I will give a short introduction to the anisotropic magnetoresistance, giant magnetoresistance and tunnel magnetoresistance.

From the point of view of both fundamental physics research and engineering device applications, there are two key questions lying in the heart of the field of *spintronics* [1,2]. The first question is how can we polarize the spin, of the charge carriers for example, in a given material system? And the second question is how can we detect the signal from the spin in that system? To generate polarized spins, typically we have to create a nonequilibrium spin population in the system. This can be realized by optical methods known as optical pumping where the spin polarization can result from the absorption of the angular momentum of the incident circular polarized light [3]. In a transport system instead, the nonequilibrium spin population can have the form of a spin current that represents a flow of electrons with a certain polarized spin direction [4]. In a ferromagnetic thin film heterostructure that may include non-magnetic, ferromagnetic and insulating layers (see Fig. 1.1 for illustration), there can be two efficient ways to generate a spin current. One way utilizes the spin filter effect where the electron spin is polarized into the majority or minority population direction

when the electrons flow through a magnetized system; while the other method relies on the spin-orbit coupling effect even though there is no magnetization in the materials.

To detect the signal from a net spin polarization in conductive electron system, one relies on the fact that as a fundamental property, the electron's spin carries angular momentum. Considering the transport scenario, if a spin current is injected into a system having a net magnetization, the angular momentum of the spin current can be transferred to the magnetization, an effect known as the *spin transfer torque* [5]. This transferred spin momentum to the magnetized system can result in the changing of the direction for the magnetic moments if the spin transfer torque is large enough, and at the same time, the status of the magnetization can be read out via different types of magnetoresistance effects where the resistance of the system depends on the relative configuration of the magnetic moment relative to either the electrical current direction or the polarization of another magnetic moment.

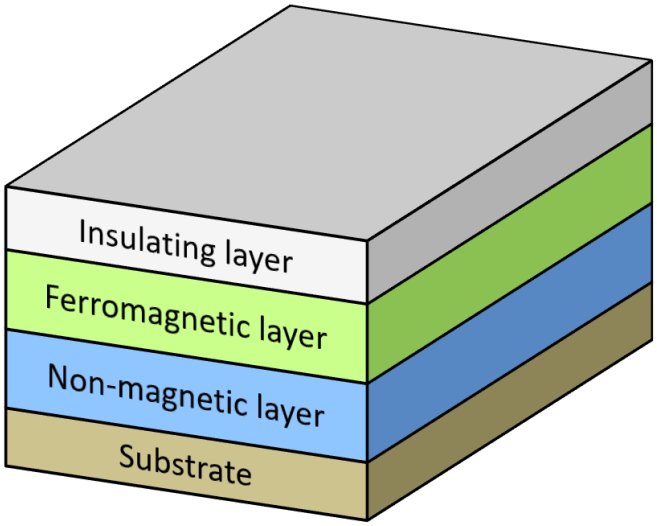

Figure 1.1: Schematic for an example of ferromagnetic thin film heterostructure.

1.1 Spin current generation via spin filter effect

In a ferromagnet, its spontaneous magnetization breaks time-reversal symmetry. This spontaneous magnetization also results in different densities of states at the Fermi surface for electrons with spin parallel or antiparallel to the magnetization due to the exchange spin splitting (see Fig. 1.2 for illustration).

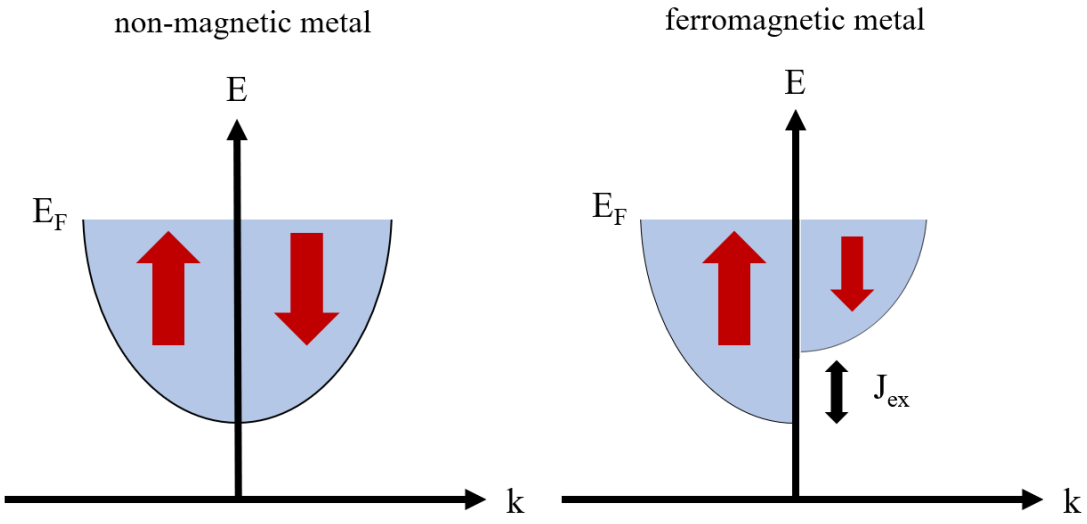

Figure 1.2: Illustration of the density of state for spin in a non-magnetic metal and ferromagnetic metal. J_{ex} is the exchange interaction energy corresponding to the spin splitting in the ferromagnet.

Conventionally, these two spin states are called majority and minority spin, with the former (majority) has a larger spin population than the latter (minority), thereby resulting in an unbalanced spin polarization inside a ferromagnet. In the transport scenario, when the electron current flows or tunnels through a ferromagnet, the originally unpolarized spin of the electrons becomes polarized due to the above effect.

When this electron flow leaves the ferromagnet and enters into an adjacent non-magnetic metal, the polarized spin persists within a certain spatial range until it becomes unpolarized again due to the spin relaxation (see Fig. 1.3). This is the basic concept lying in the pioneering work on spin injection dated back to the 1980s [6,7].

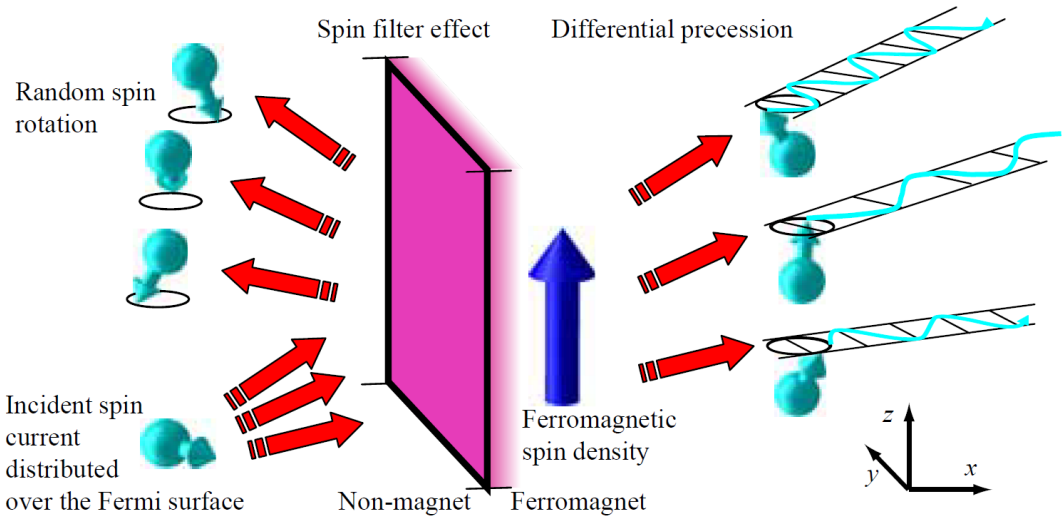

Fig. 1.3: Illustration of the spin filter effect in the generation of spin current. Figure reproduced from Stiles and Miltat [3].

1.2 Spin current generation via spin-orbit coupling

1.2.1 Spin-orbit coupling

Spin-orbit coupling can be understood via classical electromagnetism and special relativity. As known in classical electromagnetism, where an electron moves around a nucleus feels an effective magnetic field:

$$\mathbf{B} = -\frac{\mathbf{v}\times\mathbf{E}}{c^2} \tag{1.1}$$

where **v** is the velocity of the electron, **E** is the electric field in which the electron is travelling and *c* is the speed of light. Notice that **v** can be expressed via the momentum **p** and the mass of the electron m_e, then:

$$\mathbf{B} = -\frac{\mathbf{v}\times\mathbf{E}}{c^2} = \frac{\mathbf{E}\times\mathbf{p}}{m_e c^2} \tag{1.2}$$

This effective magnetic field **B** is exerted on the magnetic moment **μ** carried by the electron's spin $\mathbf{S}$, and thereby resulting in the Zeeman interaction energy:

$$H_{SO} = -\frac{1}{2}\boldsymbol{\mu}\bullet\mathbf{B} = (-g\mu_B\frac{\mathbf{S}}{2\hbar})\bullet(\frac{\mathbf{E}\times\mathbf{p}}{m_e c^2}) = \frac{g\mu_B}{2m_e c^2\hbar}\mathbf{S}\bullet(\nabla V\times\mathbf{p}) \tag{1.3}$$

where g is the electron spin g-factor, μ_B is the Bohr magneton, $\hbar$ is the Planck constant and the 1/2 factor accounts for the correction from the Thomas precession. Assuming the central field approximation, the electric potential *V* will only depend on the radius between the electron and the nucleus, therefore $\nabla V = \nabla V(\mathbf{r}) \propto \mathbf{r}$. It is not difficult to

see that the Zeeman energy is proportional to the product of the spin and the orbital angular momentum **L**:

$$H_{SO} \sim \mathbf{S}\bullet(\nabla V(\mathbf{r})\times\mathbf{p}) \sim \mathbf{S}\bullet(\mathbf{r}\times\mathbf{p}) = \mathbf{S}\bullet\mathbf{L} \tag{1.4}$$

The derivation here can be regarded as a simple example to show the concept of spin-orbit interaction (or spin-orbit coupling). Generally speaking, not only the orbital electron of an atom or molecule, but also the itinerant electrons in a given conducting system can experience the spin-orbit coupling effect, and in the following sections I will discuss two specific scenarios to introduce how the spin-orbit coupling can generate a net spin polarization.

1.2.2 Spin polarization due to spin-orbit coupling in systems with spatial inversion asymmetry

The so-called inverse spin galvanic effect (ISGE) may exist in a structure without spatial inversion symmetry [8], and such an effect can often has a form of the Rashba type spin-orbit coupling [9]:

$$H_R = \frac{\alpha_R}{\hbar}\boldsymbol{\sigma}\bullet(\mathbf{z}\times\mathbf{p}) \tag{1.5}$$

where $\boldsymbol{\sigma}$ is the Pauli matrix, **z** is the direction normal to the spatial inversion symmetry breaking plane and α_R is the Rashba parameter. Originally, the Rashba type spin-orbit coupling was proposed as a model [10] to explain the electron spin resonance phenomenon with spin-orbit splitting observed in experiments on two dimensional

GaAs-(AlGa)As semiconductor heterostructures [11,12]. In those quantum well structures with inversion asymmetry along the growth direction (e.g. **z**), the Rashba model suggests an interfacial electric field in that direction, $\mathbf{E} = E_z \mathbf{z}$. Due to the spin-orbit coupling, when the electron flows in an in-plane direction (e.g. $\mathbf{v} \| \mathbf{x}$), it feels an effective magnetic field, referred as the Rashba field, that is transverse to both the symmetry breaking direction and the flow direction (i.e. **y**). In the presence of this effective magnetic field, the spin of the electron has the Hamiltonian described by Eq.(1.3) and the spin will precess around the Rashba field, which results in the spin polarization in that field direction. This spin-momentum locking effect is illustrated in Fig. 1.4:

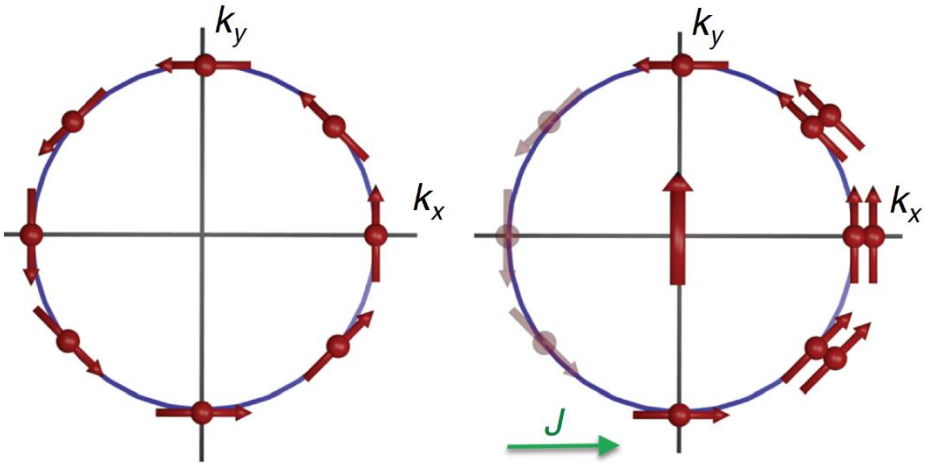

Figure 1.4: Spin-momentum locking in the electron states on the Fermi surface. Figure reproduced from Sinova et al. [8].

Although it was firstly proposed for the two dimensional semiconductor heterostructures, the Rashba model has also been used to describe the spin-orbit splitting at the surface of heavy metals [13,14] and in topological insulator systems [15]. In the early 2010s, the Rashba model was proposed to explain the spin-orbit torque observed in the normal metal/ferromagnet (NM/FM) heterostructures [16,17], although later it was demonstrated that the spin-orbit torque in NM/FM heterostructures may be better explained by the spin Hall effect in the bulk of the NM.

1.2.3 Spin polarization due to the spin Hall effect

Phenomenologically speaking, the spin Hall effect (SHE) describes a transverse spin current J_s generated by a longitudinal charge current J_c. The transverse spin current carries spin with its polarization in the direction perpendicular to the plane defined by the charge and spin current:

$$\mathbf{J}_s \sim \boldsymbol{\sigma} \times \mathbf{J}_c, \quad \mathrm{J_s} = \theta_{SH} \frac{\hbar}{2e} \mathrm{J_c} \tag{1.6}$$

where $\boldsymbol{\sigma}$ is spin polarization direction, e is the charge of electron and θ_{SH} is known as the spin Hall angle (or ratio) that can be related to the ratio of spin Hall conductivity σ_{xy}^{SH} to the longitudinal resistivity σ_{xx}:

$$\theta_{SH} = \frac{\sigma_{xy}^{SH}}{\sigma_{xx}} \tag{1.7}$$

As shown in Fig. 1.5, the SHE can be analogous to the anomalous Hall effect (AHE). However, the transverse spin current in the SHE is a pure spin current (i.e. the net charge current is zero) while in the AHE the transverse net charge current is nonzero due to the different concentrations of the majority and minority spins that are deflected.

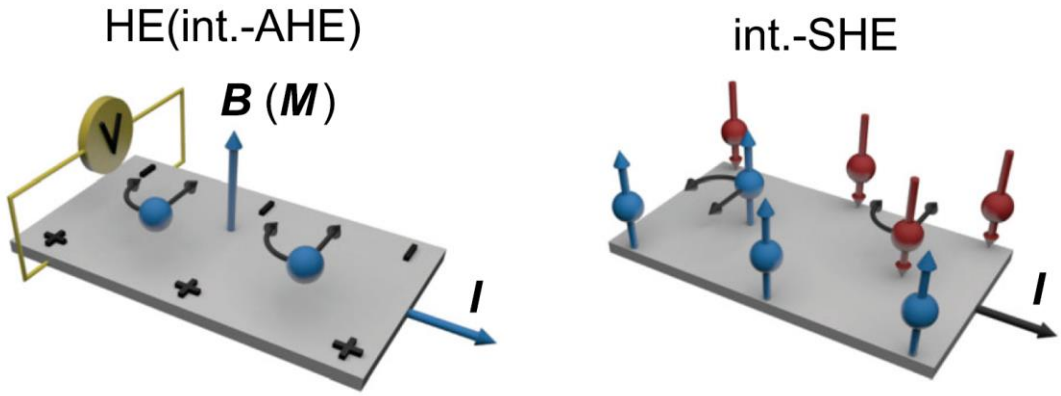

Figure 1.5: Illustration of the anomalous Hall effect and spin Hall effect. Figure reproduced from Sinova et al. [8]

The microscopic origin of the SHE lies with the spin-orbit interaction that results in the generation of the spin current. In particular, there are two mechanisms that can be responsible for the SHE: (a) the intrinsic mechanism that depends only on the electronic band structure of the material and (b) the extrinsic mechanism that relates to the electron wave packet experiencing a displacement during transport due to the spin-orbit coupling between the conduction electron and the impurity or structural disorder. The intrinsic mechanism of the SHE can be quite well described in the context of the well-studied

AHE [18] and the theory of the intrinsic SHE was first proposed by Karplus and Luttinger [19] in the 1950s and remodified recently with the Berry phases and Berry curvature language [20,21]. The intrinsic SHE was first observed experimentally in a two dimensional semiconductor system [22]. As for the extrinsic SHE, the exploration in theory can be dated back to the 1970s by Dyakonov and Perel [23] based on the idea of asymmetric scattering by Mott [24], and was later reexamined and developed around 2000 [25,26]. The first experimental observation of extrinsic SHE was also in a semiconductor system [27].

The intrinsic SHE can be described using a two-dimensional Rashba model (Eq.1.5) in systems with spatial inversion asymmetry [28], although as a more general case in which there is even no inversion asymmetry, the intrinsic spin Hall conductivity may be better calculated by the Berry phase and Berry curvature in the momentum space [29]:

$$\sigma_{xy}^{SH-\text{intrinsic}} = \frac{e}{\hbar}\sum_{\mathbf{k}}\Omega^{z}(\mathbf{k}) = \frac{e}{\hbar}\sum_{\mathbf{k}}\sum_{n} f_{\mathbf{k}n}\Omega_{n}^{z}(\mathbf{k}) \tag{1.8}$$

$$\Omega_{n}^{z}(\mathbf{k}) = \sum_{n'\neq n}\frac{2\,\mathrm{Im}\left[\left\langle \mathbf{k}n \mid j_{x}^{z} \mid \mathbf{k}n'\right\rangle\left\langle \mathbf{k}n' \mid v_{y} \mid \mathbf{k}n\right\rangle\right]}{\left(\varepsilon_{\mathbf{k}n}-\varepsilon_{\mathbf{k}n'}\right)^{2}} \tag{1.9}$$

where $\Omega_{n}^{z}(\mathbf{k})$ is the Berry curvature that describes the geometric property of the Bloch wavefunction in the nth band, $f_{\mathbf{k}n}$ is the Fermi distribution function, j_{x}^{z} is the spin current operator and v_{y} is the velocity operator. Within the Berry curvature model, the intrinsic SHE can be understood and evaluated from the viewpoint of the topological

properties of the Bloch state near the Fermi level in a band structure. For example, *ab initio* calculations such as density function calculation [29] and microscopic tight-binding calculations [30] have been utilized to quantitively predict the intrinsic spin Hall conductivity in some 4d and 5d metals (shown in Fig. 1.6 and Fig. 1.7).

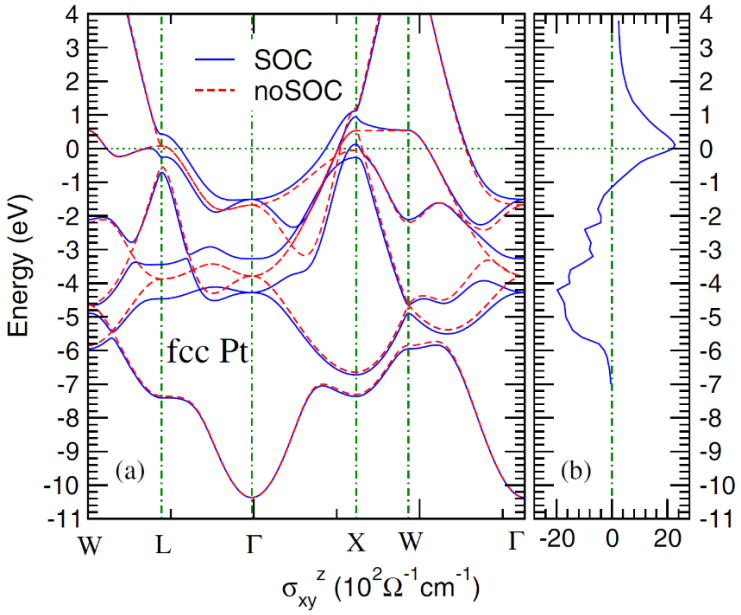

Figure 1.6: Result of a density function calculation of the intrinsic spin Hall conductivity of Pt, with the (a) band structure and (b) spin Hall conductivity of Pt. Figure reproduced from Guo et al. [29].

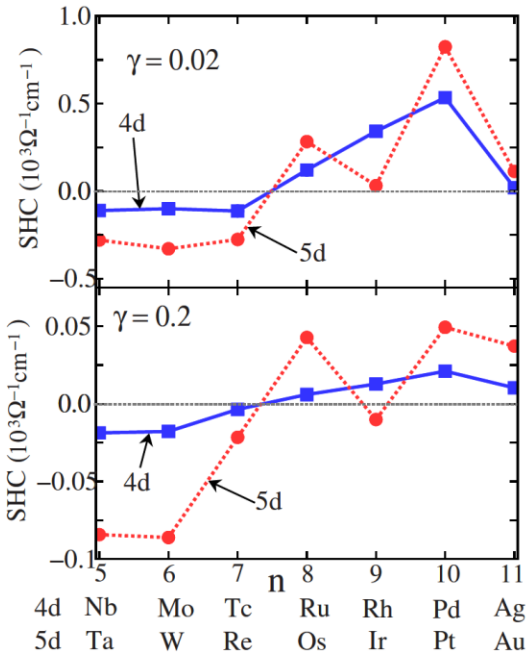

Figure 1.7: Microscopic tight-binding calculations of the intrinsic spin Hall conductivity for some 4d and 5d metals. Figure reproduced from Tanaka et al. [30].

The extrinsic mechanism SHE is typically categorized into two different types: (a) the skew-scattering contribution and (b) the side jump contribution. In the skew-scattering mechanism, due to the presence of the spin-orbit coupling, the scattering of the electron wave packet is asymmetric with respect to the spin polarization. As a result, spins polarized in opposite directions will contribute to the spin current flowing in opposite directions, thereby creating a nonequilibrium spin polarization. In the skew-scattering case, the corresponding contribution to the Hall conductivity (AHE or SHE) is proportional the Bloch state transport lifetime τ, therefore the spin Hall resistivity can be evaluated as:

$$\rho_{xy}^{SH-skew} \approx \sigma_{xy}^{SH-skew} \rho_{xx}^{2} \sim \rho_{xx} \tag{1.10}$$

First principle calculations have been performed to study the skew-scattering contribution in certain material systems for example in [31,32] (Fig. 1.8).

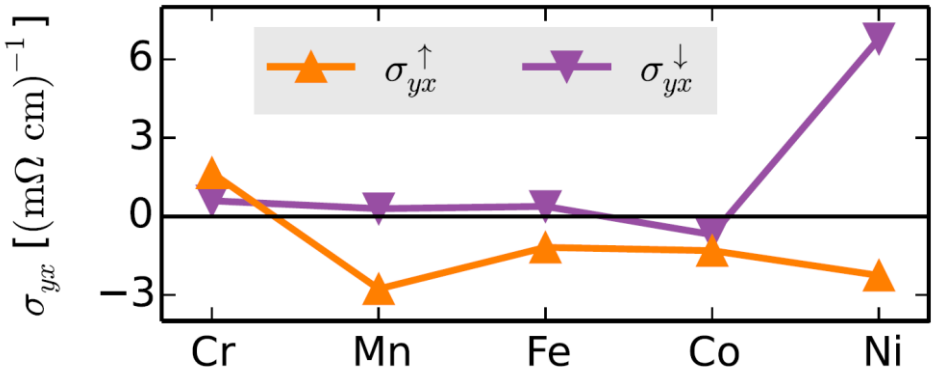

Figure 1.8: *ab initio* calculations of the skew-scattering spin Hall conductivity in Pt with some 3d magnetic impurities. $\sigma_{xy}^{\uparrow}$ and $\sigma_{xy}^{\downarrow}$ correspond to the conductivities for spin up and spin down electrons respectively. Figure reproduced from Zimmermann et al. [32].

A simple picture of the side-jump contribution is that the electron wave packet with incident wave vector **k,** when scattering off an impurity with spin-orbit interaction $H_{SO} \sim \mathbf{S}\bullet\mathbf{L}$ (Eq. 1.4), will have a displacement transverse to **k**. This mechanism was first proposed by Smit [33] and later reintroduced by Berger [34] to describe the AHE phenomenon. A detailed examination on the side-jump mechanism indicates two kinds of side-jump contribution: (a) the extrinsic side jump where the impurity has a spin-orbit interaction with the conductive electrons and (b) the intrinsic side-jump mechanism where the contribution comes from only the spin-orbit-coupled part of the wave packet (see Ref. [8] for more details). An example of the first principle calculation

of the intrinsic side-jump contribution is shown in Fig. 1.9. Recently, the side-jump mechanism has been suggested to explained the large enhancement of the SHE observed in Au doped with Ta impurity [35].

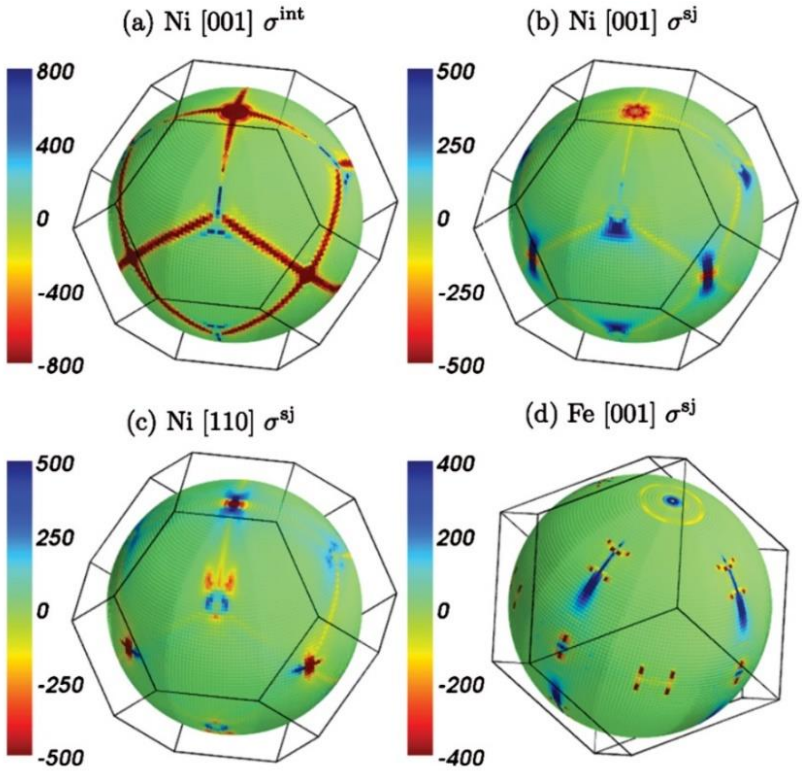

Figure 1.9: Results of first principle calculations of the angular distribution of the intrinsic (int) and side-jump (sj) contributions to the AHE in Ni and Fe oven the Fermi surface. Figure reproduced from Weischenberg et al. [35].

The side-jump contribution to the spin Hall conductivity is scattering-independent and therefore independent of the transport time lifetime τ, i.e. $\sim \tau^0$. Notice that the intrinsic contribution to the SHE is also independent of τ. As a result,

the spin Hall resistivity from the contribution of the side-jump (and intrinsic) mechanism can be expressed as:

$$\rho_{xy}^{SH-sj(\text{int})} \approx \sigma_{xy}^{SH-sj(\text{int})} \rho_{xx}^{2} \sim \rho_{xx}^{2} \tag{1.11}$$

By combining Eq.(1.10) and (1.11), we can have an expression of the spin Hall resistivity from both the intrinsic and extrinsic contributions:

$$\rho_{xy}^{SH} = a\rho_{xx} + b\rho_{xx}^{2} \tag{1.12}$$

where the first term on the right hand side of Eq.(1.12) represents the skew scattering contribution, while the second term denotes the intrinsic and/or side-jump contribution. Also, from the definition of the spin Hall angle θ_{SH} in Eq.(1.7), one has:

$$\theta_{SH} = \frac{\sigma_{xy}^{SH}}{\sigma_{xx}} \approx \frac{\rho_{xy}^{SH}}{\rho_{xx}} = a + b\rho_{xx} \tag{1.13}$$

1.3 Spin transfer torque

In 1996, the theory of "spin transfer torque" (STT) was proposed independently by Slonczewski [36] and Berger [37]. This mechanism of controlling the local magnetic moment using the transfer of the spin angular momentum instead of a magnetic field (generated by Ampere's law) opens up a totally new avenue for spintronics research and provides the foundation for fast and low energy consuming spintronics device applications down to the sub-micrometer or even nanoscale [5,38].

To understand the phenomenon of STT, one can recall that in the spin filter effect, the conductive electron spins become partially polarized when they flows through a ferromagnetic metal (FM1). Now if we have a second ferromagnet (FM2) sufficiently close to FM1, the polarized spin current will inject into FM2 before it becomes spin unpolarized because of the spin relaxation. If the spin polarization $\boldsymbol{\sigma}$ is not entirely parallel to the magnetization **m** in FM2, the transverse component of the spin polarization will be absorbed by FM2 (which can be regarded as another spin filter effect in FM2). After the transmission or reflection of the electron flow from FM2, the loss in the transverse component of the angular momentum of the spin is equal to the torque exerted on the magnetization via the conservation of the angular momentum. This is the simple picture for the mechanism of STT and it is illustrated in Fig. 1.10. Notice that in this STT geometry, the charge current is flowing perpendicular to the planes of the FM1/spacer/FM2 structure.

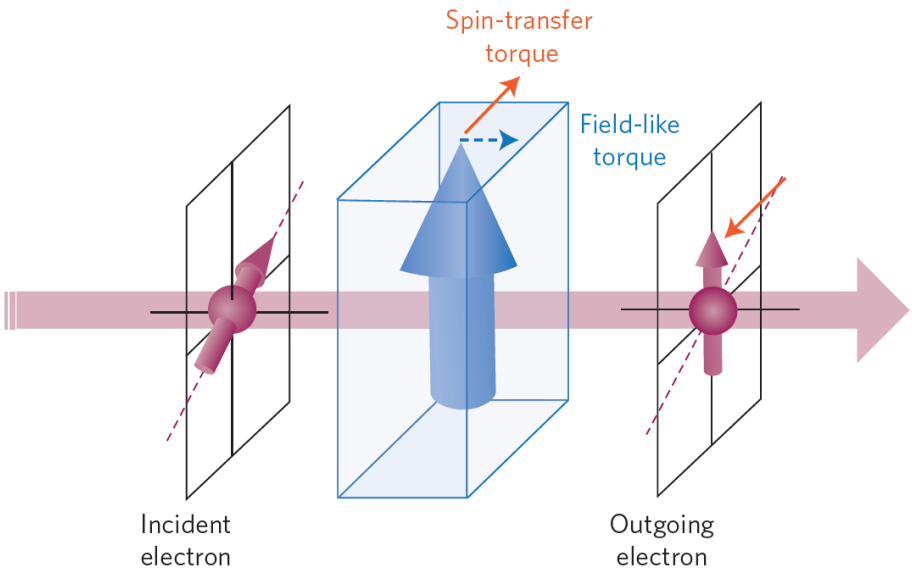

Figure 1.10: Illustration of the generation of the spin transfer torque. Figure reproduced from Brataas et al. [39]

The dynamic behavior of the magnetic moment under the influence of a STT (and other magnetic fields) can be quantitatively described by the Landau-Lifshitz-Gilbert (LLG) equation modified by adding the extra terms due to the STT:

$$\frac{d\mathbf{m}}{dt} = -\gamma \mathbf{m} \times \mathbf{H}_{\text{eff}} + \alpha \mathbf{m} \times \frac{d\mathbf{m}}{dt} + \tau_{DL} \mathbf{m} \times (\boldsymbol{\sigma} \times \mathbf{m}) + \tau_{FL} \boldsymbol{\sigma} \times \mathbf{m} \qquad (1.14)$$

where $\mathbf{H}_{\text{eff}}$ is the effective magnetic field, γ is the gyromagnetic ratio, α is the Gilbert damping constant and τ_{DL} (τ_{FL}) represents the (anti)damping-like (field-like) component of the STT. The term τ_{DL} is called (anti)damping-like is because, given the directions of the incident spin current and spin polarization, this term will subtract from or add to the Gilbert damping term in Eq.(1.14). An illustration of the magnetic moment precessing around the effective magnetic field with the STT is shown in Fig. 1.11.

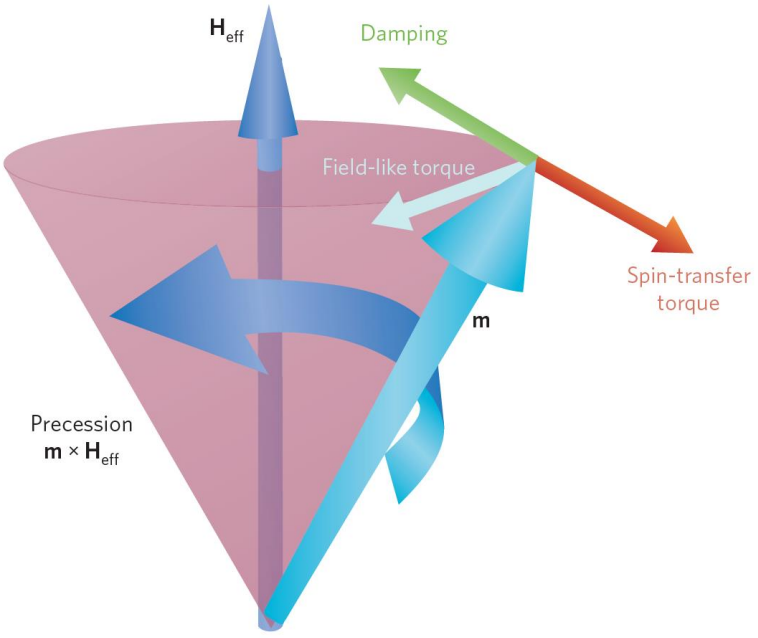

Figure 1.11 Illustration of the spin transfer torque. Notice that the "Spin-transfer torque" component in this illustration is usually referred as the "(anti)damping-like torque" among literature. Figure reproduced from Brataas et al. [39].

From the viewpoint of applied physics, the concept of using STT instead of a magnetic field to manipulate magnetic moment is of critical importance in modern spintronics applications. The possibility of controlling the magnetic state of the magnetization with STT makes it feasible to realize various magnetic devices as the elements of memory technologies compatible with circuit downscaling, such as binary memory devices [39–41], STT nano-oscillators [42,43] and spin-wave emitters [44,45].

As discussed above, in addition to the spin filter effect, spin-orbit coupling can also generate a spin current. When a ferromagnet is placed next to the material as the spin source that results from spin-orbit coupling, the injected spin current from that spin source will exert spin torque on the adjacent ferromagnet. The spin torque in this case is often referred as the "spin-orbit torque" (SOT) to be distinguished from the term "spin transfer torque" because of the different mechanisms for the generation of the spin torques. The charge current that generates SOT typically flows in-plane within the heterostructures compared to the traditional STT. The first experimental observations of the SOTs were in the early 2010s in the NM/FM bilayer structures [16,17,46,47]. Generally, the SOT also has the (anti)damping-like and field-like components as in the STT and the SOT-induced dynamics of the magnetic moment can be essentially described by the modified LLG torque equation (Eq. 1.14) as well. In addition to the torque equation, alternatively the SOT can be characterized by the *current-induced effective fields* instead of torques, typically in low frequency ($\sim$ kHz) SOT measurements [48,49]:

$$\Delta H_{DL} \equiv -\frac{\tau_{DL}}{\gamma}\boldsymbol{\sigma}\times\mathbf{m}, \quad \Delta H_{FL} \equiv -\frac{\tau_{FL}}{\gamma}\boldsymbol{\sigma} \tag{1.15}$$

where ΔH_{DL} (ΔH_{FL}) corresponds to the damping-like (field-like) SOT, and both τ_{DL} and τ_{FL} are defined in Eq. (1.14). This can be easily checked by substituting the definition of the effective fields in Eq.(1.15) back to Eq. (1.14) and notice that they indeed have the unit of a magnetic field (though they are not real magnetic fields).

1.4 Magnetoresistance

So far, I have introduced the microscopic mechanisms of the generation of spin current in spin filter effect and spin-orbit coupling. I have also briefly discussed how the spin current can interact with the magnetic moment via the spin transfer torques. However, one critical question has yet to be answered: how can one detect the signals of these spin-related effects? Actually depending on the specific system, the magnetic signals can be read out by different types of so-called magnetoresistance phenomena, in which the longitudinal (R_{xx}) or transverse resistance (R_{xy}) of the magnetic structure, which can have one or more FM layers, depends on the configuration of the magnetization.

1.4.1 Anisotropic magnetoresistance and Hall resistance

Let's consider the bulk of a conducting ferromagnetic thin film with an internal magnetization and ignore all other interfacial effects. The anisotropic magnetoresistance

(AMR) in a FM describes the resistance of the FM depending on the relative angle φ between its magnetization **m** and the charge current **J**. Let the measured longitudinal resistivity be $\rho_{\parallel}$ when **m** is parallel (or antiparallel) to **J**, and be $\rho_{\perp}$ when m is perpendicular to **J**, then AMR can be expressed as:

$$\rho_{xx} = \rho_{\perp} + \left(\rho_{\parallel} - \rho_{\perp}\right)\cos^2\varphi \tag{1.16}$$

The microscopic origin of AMR is due to the anisotropic scattering of the electron in the ferromagnet with respect to the magnetization direction [50]. Notice that AMR can not only generate a resistance change in the longitudinal direction but also in the transverse direction due to the same origin [51]:

$$\rho_{xy}^{P} = \left(\rho_{\parallel} - \rho_{\perp}\right)\sin\varphi\cos\varphi \tag{1.17}$$

This transverse anisotropic resistance effect is often referred as the “planar Hall effect”.

As for a ferromagnet, in the transverse Hall voltage there is also the well-known anomalous Hall effect which also depends on the relative angle between **m** and **J**. In the thin-film ferromagnetic structure with charge current running in plane, the anomalous Hall resistance is a function of the out-of-plane component of the magnetization:

$$R_{xy}^{A} = R_A \mathrm{m}_z \tag{1.18}$$

Therefore in such a system, the total transverse voltage signal, by combining the transverse AMR in Eq.(1.17) and the anomalous Hall signal in Eq.(1.18) can be expressed as:

$$R_{xy} = R_A \mathrm{m}_z + R_P \mathrm{m}_x \mathrm{m}_y \tag{1.19}$$

where R_A (R_P) denotes the strength of the AHE(AMR).

After the discovery of strong SHE in NM/FM systems, a new type of the magnetoresistance called "spin Hall magnetoresistance" (SMR) was also proposed [52] to explain the peculiar behaviors of the longitudinal and transverse magnetoresistance in certain SHE-based NM/FM systems [53,54]. The SMR typically has the same magnetization dependence as those in Eq. (1.16) and (1.17) but instead of being the result of spin-dependent scattering, it originates from the inverse SHE that depends on the spin accumulation at the NM/FM interface.

1.4.2 Giant magnetoresistance

The discovery of the large magnetoresistance effect in conducting ferromagnetic and non-magnetic multilayers, which was named "giant magnetoresistance" (GMR), marked the start of modern spintronics research and applications [55,56]. Considering a sandwich structure consisting of two FM layers separated by a thin conducting pacer: FM1/NM/FM2, the magnetization **m**1 and **m**2 in FM1 and FM2 can be either parallel or antiparallel to each other, as shown in Fig. 1.12.

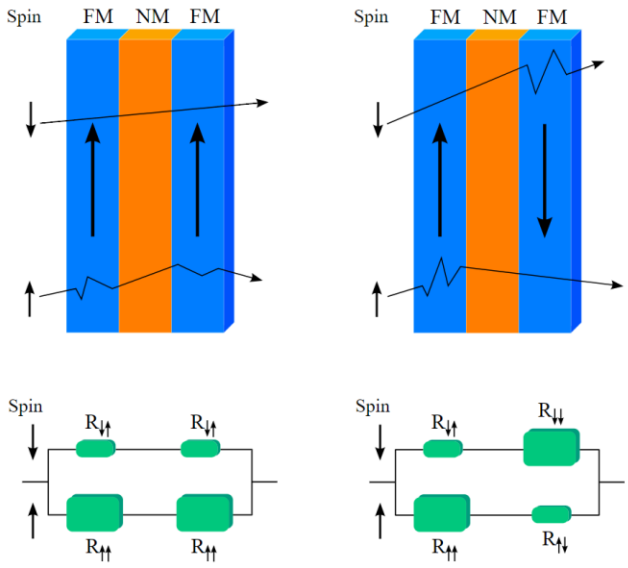

Figure 1.12: Illustration of the giant magnetoresistance. Figure reproduced from Wiki.

When a charge current is flowing perpendicular to the multilayers (current-perpendicular-to-plane, CPP), the total resistance of the structure will depend on the relative configuration of **m**1 and **m**2, and typically the resistance when **m**1 and **m**2 are parallel (R_P) is smaller than that when **m**1 and **m**2 are antiparallel (R_{AP}), i.e. $R_P < R_{AP}$. This is the GMR effect, and it also exists when the charge current is running in plane with regard to the layers (current-in-plane, CIP, though the effect is smaller than the CPP case [57]). The CPP scheme is also known as the "spin valve" structure.

Spin-dependent scattering is the origin of the GMR effect. The GMR can be described by the two-current model [58]. The majority spin, when the spin polarization

is parallel to the magnetization, usually has weaker scattering (and thus lower resistance $R_{\uparrow\uparrow} = R_{\downarrow\downarrow}$ in Fig. 1.12). However, the minority spin that has spin polarization antiparallel to the magnetization tends to have stronger scattering (and thus higher resistance $R_{\uparrow\downarrow} = R_{\downarrow\uparrow}$ in Fig. 1.12). One may define the GMR ratio as $\left(R_{AP} - R_P\right)/R_P$, and from Figure 1.12 one can have:

$$GMR = \frac{R_{AP} - R_P}{R_P} = \frac{1}{4}\frac{\left(R_{\uparrow\uparrow} - R_{\uparrow\downarrow}\right)^2}{R_{\uparrow\uparrow}R_{\uparrow\downarrow}} \tag{1.20}$$

Figure 1.13 shows the first experimental observations of the GMR effect.

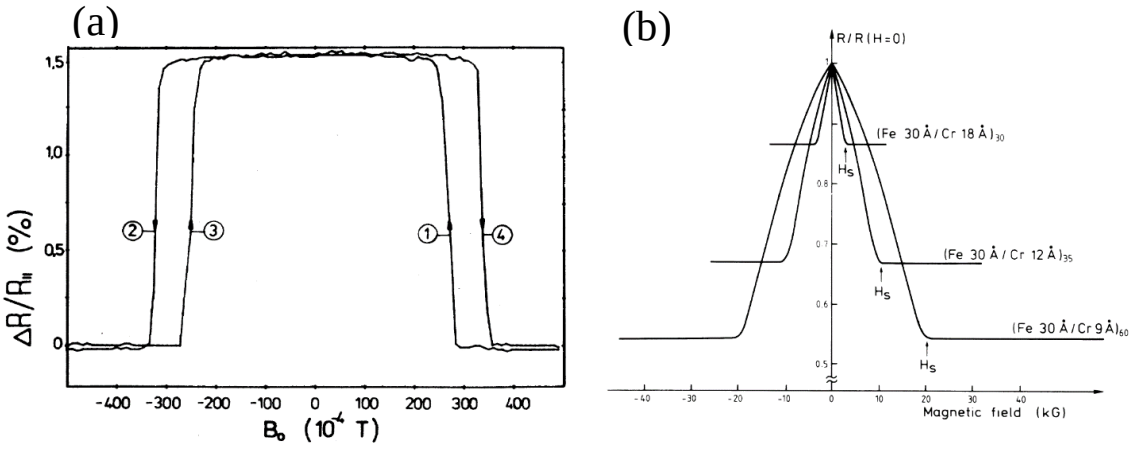

Figure 1.13: First experimental observations of the giant magnetoresistance effect in Fe/Cr multilayers at (a) room temperature and (b) cryostat temperature. Figure reproduce from Binasch et al. [56] and Baibich et al. [57].

1.4.3 Tunnel magnetoresistance

In addition to GMR, the observation of tunnel magnetoresistance (TMR) also has played an important role since the early research in spintronics. Unlike GMR, TMR exists in FM1/insulator/FM2 junction structure and it was firstly observed in Fe/Ge/Co junction under cryogenic temperature in 1975 by Julliere [59]. In a FM1/insulator/FM2 structure, when the insulator is sufficiently thin, the electron from one side in the ferromagnet can be tunneled through the insulator to the other side. As explained previously, the majority and minority spin in a ferromagnet have different density of states (DOS). As a result, when a bias is applied across the junction, the tunnel resistance can change depending on whether the majority(minority) spin on one side tunnels to the majority or minority band on the other side of the insulator, as illustrated in Fig. 1.14.

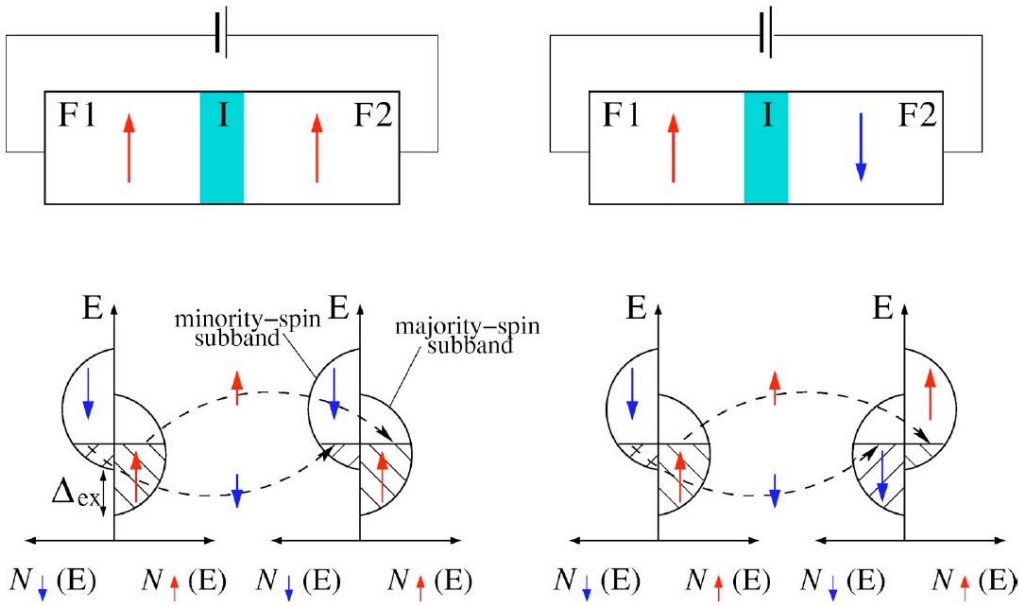

Figure 1.14: Illustration of the tunnel magnetoresistance. Figure reproduced from Zutic et al. [2].

For a given material system, the TMR depends on the spin polarizations, P_1 and P_2, of the ferromagnets on both side of the insulating barrier. The spin polarization can be calculated from the majority and minority spin DOS at the Fermi level [2]:

$$P = \frac{N_{\uparrow}(E_F) - N_{\downarrow}(E_F)}{N_{\uparrow}(E_F) + N_{\downarrow}(E_F)} \tag{1.21}$$

where $N_{\uparrow}(E_F)$ and $N_{\downarrow}(E_F)$ are the DOS for the majority and minority spin at the Fermi level respectively. Notice that Eq. (1.21) is often an over-simplified model to a realistic material system, for example MgO tunnel barriers. The TMR ratio can be given by:

$$TMR = \frac{R_{AP} - R_P}{R_P} = \frac{2P_1P_2}{1 - P_1P_2} \tag{1.22}$$

where R_P (R_{AP}) denotes the tunnel resistance when the two magnetizations are parallel (antiparallel) in the FM1/insulator/FM2 junction.

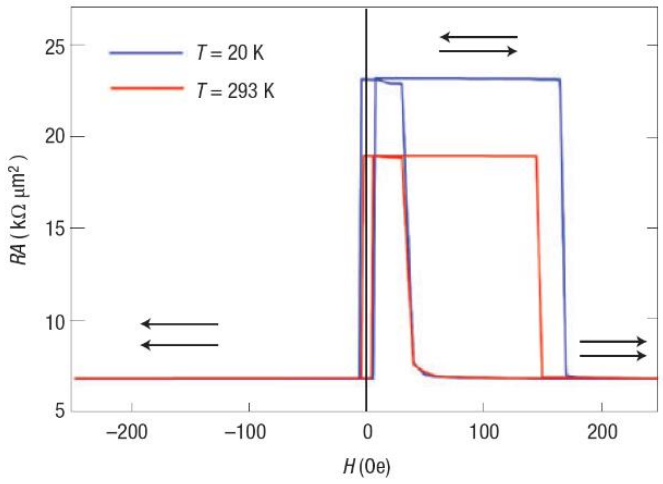

Figure 1.15: Experimental observation of large tunnel magnetoresistance in the epitaxial growth Fe/MgO/Fe junction. Figure reproduced from Yuasa et al. [63].

After the discovery of TMR, large TMR was later observed in Al oxide junctions [60,61]. In 2004, over 200% TMR at room temperature was observed in Fe/MgO/Fe and CoFe/MgO/CoFe junctions [62,63] (an example shown in Fig. 1.15), demonstrating the feasibility of using a magnetic tunnel junction (MTJ) as the basic memory element in non-volatile magnetic random-access memory (MRAM) with potentially high storage density. The highest record so far of TMR at room temperature is above 600% in CoFeB/MgO/CoFeB junction [64].

CHAPTER 2

SPIN-ORBIT TORQUE IN NORMAL METAL/FERROMAGNET HETEROSTRUCTURES

In the following sections, I will firstly introduce the concept of the interfacial spin mixing conductance. Then I will derive the analytical expressions for the SHE-induced spin torques in the NM/FM/oxide heterostructure using the spin diffusion model and compare them with the experimental results to illustrate the important role of the interfaces in the spin transport. Lastly, I will show the spin torque measurements under different interfacial and ambient temperature conditions to demonstrate that the SHE can not only generate large damping-like torque but also a sizable field-like torque when the FM is thin.

2.1 Introduction

In a non-magnetic normal metal/ferromagnet/oxide heterostructure (NM/FM/oxide, such as illustrated in Fig. 1.1) in which the NM exhibits a strong SHE, as mentioned in chapter 1, the SHE generates a transverse spin current that can be injected into the FM resulting in SOT being exerted on the magnetization **m**. This process can be described more precisely with the concepts of *spin accumulation* and the so-called *spin mixing conductance*. The SHE-induced spin current is a result from the longitudinal charge current. This transverse spin current will diffuse through the NM and generate a spin accumulation $\boldsymbol{\mu}_s$, i.e. the non-equilibrium spin population with the form of a potential analogous to a charge potential, at the NM/FM interface. This spin

transport usually can be described by the spin diffusion model in the bulk of the NM [65]. The amount of the spin accumulation at the interface is also governed by the interfacial spin mixing conductance which determines the fraction of the spin current that enters the FM and the fraction being reflected.

2.2 Interfacial spin mixing conductance

2.2.1 Magnetoelectronic circuit model

The non-local spin transport process in a NM/FM heterostructure can be effectively described by the magnetoelectronic circuit model [66–68]. In the schematic illustrated in Fig. 2.1, the NM (also referred as the "node") is connected to several FM parts (also referred as the "reservoirs") and when the chemical potentials are not identical in the FM reservoirs, the NM node can have a non-equilibrium spin population.

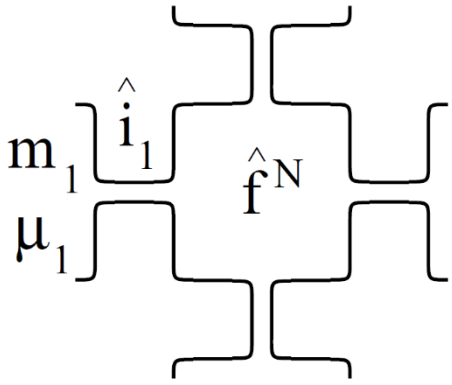

Figure 2.1: Illustration of the node-reservoir scheme in the magnetoresistance circuit model. Figure reproduced from Brataas et al. [66].

In the spin space, the current $\hat{i}$, including the part from a spin current, per energy interval at energy ε in the NM node near the contact can be expressed in a 2×2 matrix [66]:

$$\hat{i} = \frac{e^2}{h}\sum_{nm}\left[\hat{r}^{nm}\hat{f}^{N}\left(\hat{r}^{nm}\right)^{*} + \hat{t}^{nm}\hat{f}^{F}\left(\hat{t}^{nm}\right)^{*}\right] - M\hat{f}^{N} \tag{2.1}$$

where $\hat{r}^{nm}$ is the reflection matrix for an electron from mode m (in the Landauer formulism) reflected in mode n, $\hat{t}^{nm}$ is the transmission matrix for an electron from mode m transmitted in mode n, $\hat{f}^{N(F)}$ is the Fermi distribution in NM(FM), and *M* is the number of the propagating channels. With the definition of $\hat{u}^{\uparrow} = \left(\hat{1} + \hat{\boldsymbol{\sigma}}\bullet\mathbf{m}\right)/2$ and $\hat{u}^{\downarrow} = \left(\hat{1} - \hat{\boldsymbol{\sigma}}\bullet\mathbf{m}\right)/2$, in which $\hat{1}$ is the unit matrix and $\hat{\boldsymbol{\sigma}}$ is a vector of the Pauli spin matrix, Eq. (2.1) can be further written as:

$$\begin{aligned}\hat{i} = {} & G^{\uparrow}\hat{u}^{\uparrow}\left(\hat{f}^{F} - \hat{f}^{N}\right)\hat{u}^{\uparrow} + G^{\downarrow}\hat{u}^{\downarrow}\left(\hat{f}^{F} - \hat{f}^{N}\right)\hat{u}^{\downarrow} \\ & - G^{\uparrow\downarrow}\hat{u}^{\uparrow}\hat{f}^{N}\hat{u}^{\downarrow} - \left(G^{\uparrow\downarrow}\right)^{*}\hat{u}^{\downarrow}\hat{f}^{N}\hat{u}^{\uparrow}\end{aligned} \tag{2.2}$$

where G^{s} ($s = \uparrow, \downarrow$) is the spin dependent conductance and $G^{\uparrow\downarrow}$ is the spin mixing conductance defined as:

$$G^{s} = \frac{e^2}{h}\left[M - \sum_{nm}\left|r_{s}^{nm}\right|^{2}\right] \tag{2.3}$$

$$G^{\uparrow\downarrow} = \frac{e^2}{h}\left[M - \sum_{nm} r_{\uparrow}^{nm}\left(r_{\downarrow}^{nm}\right)^{*}\right] \tag{2.4}$$

$G^{\uparrow\downarrow}$ is a complex quantity and it is usually expressed with the real("r") and imaginary("i") parts respectively: $G^{\uparrow\downarrow} = G_r + iG_i$. The theoretical calculations based on Green function point out that $G_r \gg G_i$ in some typical NM/FM structures [69]. Sometimes the spin mixing conductance is also written as the normalized conductance: $g^{\uparrow\downarrow} \equiv G^{\uparrow\downarrow}(h/e^2)$. The spin mixing conductance essentially describes the spin transport process when the spin polarization **s** is noncollinear with the magnetization **m**, and it can be used to evaluate the spin current when the spin accumulation is not equal across the NM/FM interface. Notice that the spin accumulation can be generally calculated as [68]:

$$\boldsymbol{\mu}_s = \int d\varepsilon \mathrm{Tr}\left[\hat{\boldsymbol{\sigma}}\hat{f}\left(\varepsilon\right)\right] \tag{2.5}$$

The analytical form of Eq. (2.5) depends on the boundary conditions of the structure.

2.2.2 An example: spin pumping

The magnetoresistance circuit model and the concept of spin mixing conductance can be applied to describe the dynamic spin process. A good example is the spin pumping phenomenon, for which the magnetoresistance circuit theory provides a clear explanation [70] of the enhanced Gilbert damping in comparison to the bulk values observed in some early experiments on NM/FM heterostructures [39,71,72].

In a typical spin pumping experiment (as schematically illustrated in Fig. 2.2), the magnetization **m** is excited by the external magnetic field (usually in the RF

microwave frequency range). Under resonance condition, **m** precesses around the effective magnetic field. As a result, a spin current $\mathbf{I}_s^{pump}$ is pumped out of the FM [70]:

$$\mathbf{I}_s^{pump} = \frac{\hbar}{4\pi}\left(A_r \mathbf{m} \times \frac{d\mathbf{m}}{dt} - A_i \frac{d\mathbf{m}}{dt} \right) \tag{2.6}$$

In the above equation, **m** is the dynamic vector of the magnetization that obeys the LLG equation, and the so called "spin pumping conductance" $A = A_r + iA_i$ is essentially equal to $g^{\uparrow\downarrow}$, i.e. the spin mixing conductance, when the FM is thick enough.

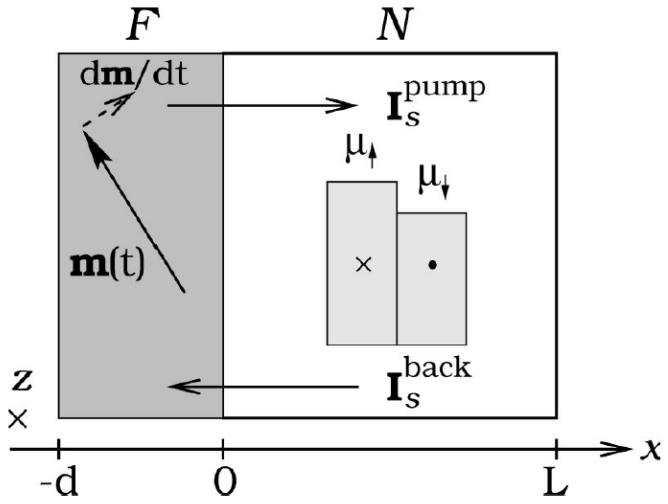

Figure 2.2: Schematic of the spin pumping process. Figure reproduced from Tserkovnyak et al. [67].

Taking into account the backflow of spin into the FM induced by the spin accumulation at the NM/FM interface [67], the total spin current can be evaluated to be proportional to the spin pumping current (Eq.2.6), $\mathbf{I}_s \propto \mathbf{I}_s^{pump} \sim \mathbf{m} \times \frac{d\mathbf{m}}{dt}$, in which the

imaginary part of the spin mixing conductance is usually ignored. The net total spin current, when pumped out of the FM and injected into the NM, carries a spin torque, $\boldsymbol{\tau} \sim -\mathbf{I}_s$, that is exerted on the FM. After substituting this torque into the LLG equation, it is not difficult to see that this torque from spin pumping effectively adds to the Gilbert damping constant. This is the spin pumping model for the enhanced Gilbert damping constant ($\Delta\alpha$)in NM/FM thin film heterostructure and it is an interfacial effect. Notice that the enhanced damping constant is expected to be proportional to the inverse of the FM thickness, $\Delta\alpha \propto t_{FM}^{-1}$ since it is an interfacial effect [67].

2.3 Dependence of the interfacial transparency of spin-orbit torque in the thin film heterostructures

2.3.1 Derivation of the spin torque expression in a NM/FM bilayer system

In this section, I will derive the analytical expression of the SHE-induced spin torque in a NM/FM bilayer structure illustrated in Fig. 2.3 using the spin diffusion model [65].

Here I will assume the charge current j_c is running in the x direction. In a SHE scenario, this charge current generates a transverse spin current. In a thin film structure (the x-y plane in this case), I will focus on the diffusive spin current on the z direction (i.e. one-dimensional approximation) that has spin polarization along the y axis.

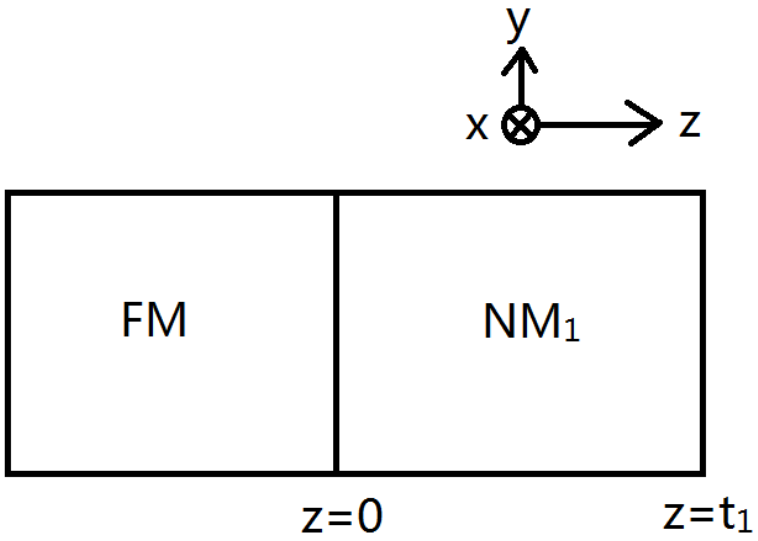

Figure 2.3: Schematic of the normal metal/ferromagnet bilayer.

Therefore, in the NM1 the SHE generates a spin current, $\mathbf{j}_1^{SHE}$ as:

$$\mathbf{j}_1^{SHE} = \theta_{SH} j_{c,x} \mathbf{y} = j_1^{SHE} \mathbf{y} \tag{2.7}$$

Notice that the vector in Eqn. (2.7) denotes the spin polarization direction. The spin current results in a spin accumulation distribution, $\boldsymbol{\mu}_1^s$, inside NM1 that satisfies the diffusion equation:

$$D \frac{\partial^2 \boldsymbol{\mu}_1^s}{\partial z^2} = \frac{\boldsymbol{\mu}_1^s}{\tau_{sf}} \tag{2.8}$$

where D is the conduction electron diffusion coefficient and τ_{sf} is the spin-flip time in NM_1. Here I have assumed that the precession frequency ω of $\boldsymbol{\mu}_1^s$ satisfies $\omega\tau_{sf} \ll 1$. Eq. (2.8) has a general solution as:

$$\boldsymbol{\mu}_1^s = \mathbf{A}e^{-\frac{z}{\lambda_1}} + \mathbf{B}e^{\frac{z}{\lambda_1}} \tag{2.9}$$

where $\lambda_1 = \sqrt{D\tau_{sf}}$ is the spin diffusion length in NM_1 with thickness t_1 and conductivity σ_1. The total spin current $\mathbf{j}_{s,1}$ in NM_1 will include the component from the SHE-induced spin current and that from the diffusive spin current resulting from the spin accumulation:

$$\mathbf{j}_{s,1} = -\frac{\sigma_1}{2e}\frac{\partial \boldsymbol{\mu}_1^s}{\partial z} - j_1^{SHE}\mathbf{y} \tag{2.10}$$

Consider the two boundary conditions at z=0 (the NM/FM interface) [65] and $z=t_1$ (the NM/substrate interface) in Fig. 1.3:

$$\mathbf{j}_{s,1}(0) = -\frac{G_r}{e}(\mathbf{m}\times(\boldsymbol{\mu}_1^s(0)\times\mathbf{m})) - \frac{G_i}{e}(\boldsymbol{\mu}_1^s(0)\times\mathbf{m}) \tag{2.11}$$

$$\mathbf{j}_{s,1}(t_1) = 0 \tag{2.12}$$

Notice that in the boundary condition Eq.(2.11), we ignore the component of the spin current that has the spin polarization along the magnetization $\mathbf{m}$, since the component will not contribute to the torque. By further assuming that the imaginary part of the spin mixing conductance G_i is negligible compared to G_r, solving Eq. (2.9)-(2.12) gives the spin current at the NM/FM interface (i.e. z=0):

$$\mathbf{j}_{s,1}(0) = -j_1^{SHE}(1-\operatorname{sech}(\frac{t_1}{\lambda_1}))\frac{2G_r}{2G_r + G_1\tanh(\frac{t_1}{\lambda_1})}\mathbf{m}\times(\mathbf{y}\times\mathbf{m}) \tag{2.13}$$

In Eq.(2.13), I have defined the "spin conductance" G_1 of NM1 as $G_1 = \sigma_1 / \lambda_1$. The spin current in Eq.(2.13), after injecting into the FM (with thickness t_{FM}), exerts a torque on the magnetization (with magnitude M_s):

$$\boldsymbol{\tau} = -\frac{\gamma\hbar}{2eM_s t_{FM}} \mathbf{m} \times (\mathbf{m} \times \mathbf{j}_{s,1}(0)) \tag{2.14}$$

After substituting Eq. (2.13) into (2.14), the spin torque reads:

$$\boldsymbol{\tau} = (\frac{\gamma\hbar}{2eM_s t_{\mathrm{FM}}}) j_1^{SHE} (1 - \mathrm{sech}(\frac{t_1}{\lambda_1})) \left[\frac{2G_r}{2G_r + G_1 \tanh(t_1 / \lambda_1)} (\mathbf{m} \times (\mathbf{y} \times \mathbf{m})) \right] \tag{2.15}$$

Notice that the torque in Eq. (2.15) corresponds to the damping-like torque. The field like torque, which depends on magnitude of G_{i}, can be derived similarly [65]. On the other hand, in a spin pumping experiment, the enhanced damping can be calculated in a very similar way [73]:

$$\Delta\alpha = \frac{\gamma\hbar}{4\pi M_s t_{\mathrm{FM}}} \bullet \frac{2G_{\mathrm{r}} G_1 \tanh(t_1 / \lambda_1)}{G_0 (2G_{\mathrm{r}} + G_1 \tanh(t_1 / \lambda_1))} = \frac{\gamma\hbar}{4\pi M_s t_{\mathrm{FM}}} g_{\mathrm{eff}}^{\uparrow\downarrow} \tag{2.16}$$

where $G_0 = 2e^2 / h$ is the conductance quantum, and I have defined the effective spin mixing conductance $g_{\mathrm{eff}}^{\uparrow\downarrow} = \frac{2G_{\mathrm{r}} G_1 \tanh(t_1 / \lambda_1)}{G_0 (2G_{\mathrm{r}} + G_1 \tanh(t_1 / \lambda_1))}$.

2.3.2 Interfacial spin transparency and spin memory loss

From Eq. (2.15), the (damping-like) spin-torque efficiency, ξ_{DL}, can be defined as:

$$\xi_{DL} = \theta_{SH} \frac{2G_r}{2G_r + G_1 \tanh(t_1 / \lambda_1)} \tag{2.17}$$

The spin-torque efficiency is what we measured from the direct SHE experiments in which the strength of the SHE is estimated from the magnitude of spin torque. Eq. (2.17) indicates that generally the spin-torque efficiency is less than the internal spin Hall angle and their ratio can be defined as the interfacial spin transparency:

$$T_{\text{int}} \equiv \frac{\xi_{DL}}{\theta_{SH}} = \frac{2G_r}{2G_r + G_1 \tanh(t_1 / \lambda_1)} \tag{2.18}$$

The concept of the interfacial spin transparency emphasizes the importance of the interface for a given NM/FM structure, since the net spin torque exerted on the FM, which is proportional to ξ_{DL}, is constrained by T_{int}. On the other hand, ξ_{DL} is always a lower bound of the internal spin Hall angle, since $T_{\text{int}} < 1$.

The derivation above assumes that there is no extra spin relaxation at the NM/FM interface. However there could be some kind of spin relaxation process in a realistic interface and it can be generally referred as the spin memory loss (SML) effect [74]. The SML may be modeled as a very thin layer (with thickness t_I and spin diffusion length $\lambda_{s,I}$) between the NM and FM serving as the spin relaxation region. After some math by solving this trilayer model and assuming that the NM is thick

enough compared its spin diffusion length, the spin torque efficiency can be expressed as [73]:

$$\xi_{DL} = \theta_{SH} \frac{G_{\text{eff}}^{\uparrow\downarrow}}{G_{\text{I}} \sin\delta + G_{\text{NM}} \cos\delta} \tag{2.19}$$

where the spin flip parameter is defined as $\delta = t_{\text{I}} / \lambda_{\text{s,I}}$, $G_{\text{I}} = \sigma_{\text{I}} / \lambda_{\text{s,I}}$, and $G_{\text{eff}}^{\uparrow\downarrow}$ is the effective spin mixing conductance, which in this case is a parameter depending on the spin mixing conductance and the spin conductance of the NM and SML layers [73]. Eq. (2.19) suggests that the stronger the spin flip in the SML (i.e. larger δ), the smaller the spin torque efficiency is, which is exactly the essence of the SML effect. The SML has been applied to explain the different length scales in thickness-dependent spin Hall signal and magnetic damping in the inverse spin Hall experiments [74].

2.3.3 Experimental results

In order to test the concept of the interfacial spin transparency and reveal the important role the interface plays in the spin torque process, we fabricated a series of Pt-based Pt/FM heterostructures and measured their SHE-induced spin torques. The thin film heterostructures here were grew by direct current (DC) sputtering (RF magnetron for the insulating oxide layers) from 2-inch planar magnetron sources onto thermally-oxidized Si substrates. The sputtering chamber had base pressure $< 4\times10^{-8}$ Torr, with the DC sputtering conditions of 2 mTorr Ar and 30 watts power, which resulted in a low deposition rate of ≈ 0.01 nm/s for the different conducting layers.

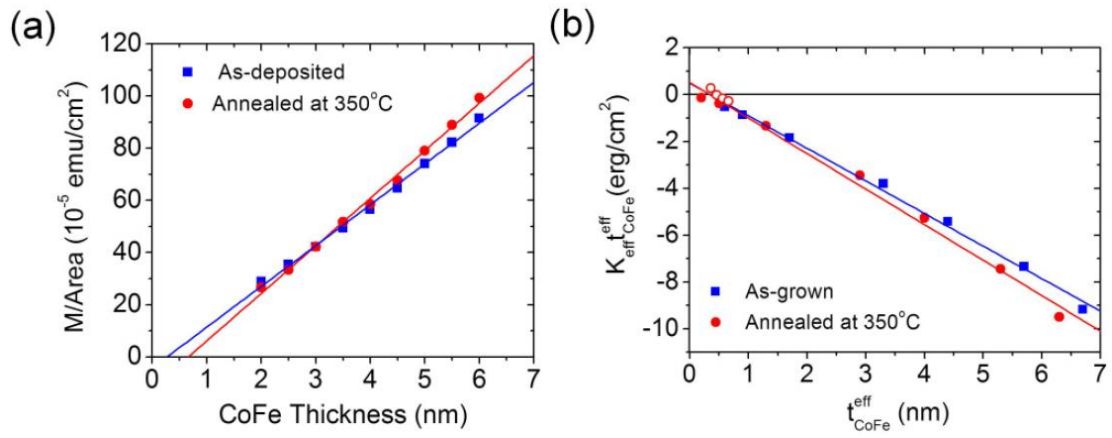

Figure 2.4: Characterization of the magnetic properties of the CoFe/Pt samples. (a) The VSM measurements on the as-grown and annealed samples. (b) The magnetic anisotropy energy density calculated from the magnetization and effective thickness of the CoFe/Pt samples. The red solid and open circles are data from two samples. Figures reproduced from Pai et al. [73].

Firstly, we characterized the samples' magnetic properties via the vibrating sample magnetometer (VSM). Fig. 2.4 shows the results for the as-grown and annealed (at 350C for 30 min) substrate/$Co_{50}Fe_{50}(t_{CoFe})$/Pt(4) with $1\text{nm} \le t_{CoFe} \le 9\text{nm}$. In Fig.2.4(a), the linear fits to the magnetic moment as a function of the CoFe thickness gives the magnetization $M_s = 1.56\times10^6$ A/m and the magnetic dead layer $t_{dead} = 0.30 \pm 0.10\,\text{nm}$ for the as grown sample, and $M_s = 1.82\times10^6$ A/m and $t_{dead} = 0.70 \pm 0.10\,\text{nm}$ for the annealed sample. The increased magnetization and dead layer after annealing indicate the possible change in the crystalline structure of the CoFe layer and a different interface between CoFe and Pt.

The changes in the magnetic properties of these CoFe/Pt samples before and after annealing are also indicated by the effective magnetic anisotropy energy density K_{eff} calculated from the effective magnetization $4\pi M_{\text{eff}}$ (determined from the spin-torque ferromagnetic resonance experiments, see below) and effective FM thickness t_{eff} (i.e. the thickness after subtracting the apparent dead layer thickness from the nominal thickness). The effective magnetic anisotropy energy density usually can be separated into the bulk and interfacial terms, which denotes the bulk (K_b) and interfacial (K_s) contribution to the magnetic anisotropy respectively:

$$K_{\text{eff}} t_{\text{eff}} = \left(K_b - 2\pi M_s^2\right) t_{\text{eff}} + K_s \tag{2.20}$$

Using Eq. (2.20), the linear fits in Fig.2.4(b) gives $K_s^{\text{as-grown}} = 0.48 \pm 0.17\,\text{erg/cm}^2$ and $K_s^{\text{annealed}} = 0.52 \pm 0.21\text{erg/cm}^2$ respectively. The slightly different slopes for the as-grown and annealed cases are consistent with the changes in M_s determined from the VSM measurements Fig.2.4(a).

Next, I measured the spin torques via the spin-torque ferromagnetic resonance (ST-FMR) method [46]. In a ST-FMR experiment, a RF current with frequency f ($\sim$ GHz) is running in the sample while under an external magnetic field H_{ext}. The resonant condition describing the relation between the frequency, magnetic field and the effective magnetization of the FM follows the Kittel formula:

$$f = \frac{\gamma}{2\pi}\sqrt{H_{\text{ext}}\left(H_{\text{ext}} + 4\pi M_{\text{eff}}\right)} \tag{2.21}$$

Eq. (2.21) can be used to evaluate the effective magnetization ($4\pi M_{\text{eff}}$, also referred as the effective demagnetization field).

In the ST-FMR measurements, the line shape of the resonance peak includes the symmetric (S) and antisymmetric (A) components where S is due to the damping-like torque while A is a result from the field-like torque. The FMR spin torque efficiency can be evaluated via the S/A ratio [73]:

$$\xi_{\text{FMR}} = \frac{S}{A}\left(\frac{e}{\hbar}\right) 4\pi M_s t_{\text{FM}}^{\text{eff}} t_{\text{NM}} \sqrt{1+\left(4\pi M_{\text{eff}} / H_0\right)} \tag{2.22}$$

where H_0 is the resonance field. In a system in which the field-like torque only results from the Oersted field, ξ_{FMR} is equal to the damping-like spin torque efficiency (i.e. $\xi_{\text{FMR}} = \xi_{DL}$) and it should be independent of the FM thickness. However, if the field-like torque has also an additional effective field-like component and if that is proportional to $1/t_{\text{FM}}^{\text{eff}}$, then there is [73]:

$$\frac{1}{\xi_{FMR}} = \frac{1}{\xi_{DL}}\left(1+\frac{\hbar}{e}\frac{\xi_{FL}}{4\pi M_s t_{\text{FM}}^{\text{eff}} t_{\text{NM}}}\right) \tag{2.23}$$

where ξ_{FL} is the field-like spin torque efficiency from the effective field-like torque excluding the Oersted field contribution.

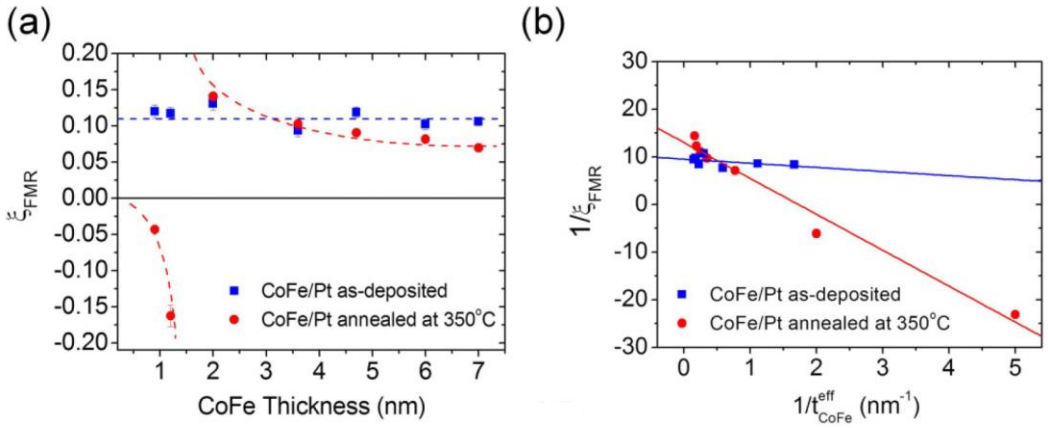

Figure 2.5: ST-FMR measurements of the CoFe/Pt samples. Figures reproduced from Pai et al. [73].

Figure 2.5 shows the ST-FMR measurements of the CoFe/Pt samples. As shown in Fig. 2.5(a) for the as-grown CoFe/Pt sample, the FMR spin torque efficiency $\xi_{\mathrm{FMR}} \approx 0.10$ with no significant t_{CoFe} dependence, which indicates that the effective field-like indicating that the effective field-like component is negligible in these as-grown samples (i.e. $\xi_{FL} \sim 0$). On the other hand, also shown in Fig. 2.5(a) for the annealed CoFe/Pt samples, ξ_{FMR} exhibits obvious t_{CoFe} dependence, suggesting the presence of the non-zero ξ_{FL}. The sign change in ξ_{FMR} around t_{CoFe}=2 nm is associated with a sign change in the antisymmetric component of the ST-FMR signal, which field-like spin-orbit torque and the Oersted torque has opposite signs. By fitting the inverse of the FMR spin torque efficiency as a function of the inverse of the effective thickness of the CoFe layer using Eq. (2.23), we find $\xi_{DL}^{\text{as-grown}} = 0.10 \pm 0.005$ and $\xi_{FL}^{\text{as-grown}} = -0.004 \pm 0.002$, while $\xi_{DL}^{\text{annealed}} = 0.077 \pm 0.005$ and $\xi_{FL}^{\text{annealed}} = -0.011 \pm 0.003$.

The decreasing of the damping-like spin torque efficiency after annealing demonstrates the sensitivity of the interfacial spin transport to the details of the composition and processing of the NM/FM interface, and it is probably due to the enhanced dead layer forming the SML layer at the interface upon annealing.

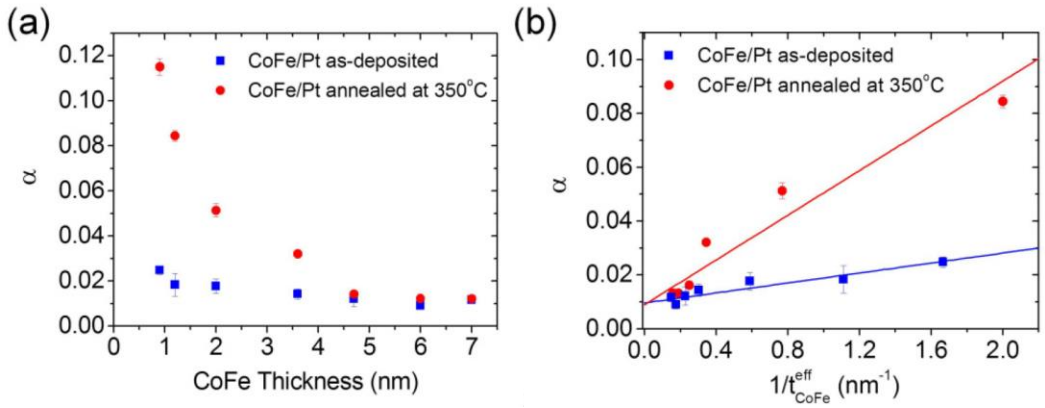

Figure 2.6: Magnetic damping measurements of the CoFe/Pt samples. Figure reproduced from Pai et al. [73].

In addition to the spin torque, as mentioned previously the magnetic damping measurements can also provide important information about the interfacial transparency. Fig. 2.6 shows the magnetic damping measurements on the CoFe/Pt before and after annealing. As shown in Fig. 2.6(a), the magnetic dampening α increases with decreasing t_{CoFe} in both cases, but the increase is more pronounced for the annealed samples. As mentioned in the previous part (Eq. (2.16)), the enhanced magnetic damping can be related to the effective spin mixing conductance $g_{\text{eff}}^{\uparrow\downarrow}$, in a NM/FM heterostructure which can be described by the spin pumping theory and without significant SML contribution. A linear fit to the as-grown CoFe/Pt sample is given in Fig. 2.6(b) using

Eq. 2.16, which gives $g_{\text{eff,as-grown}}^{\uparrow\downarrow} = (9.8 \pm 0.2) \times 10^{18}\ \text{m}^{-2}$ and an intrinsic Gilbert damping constant $\alpha_0 = 0.009 \pm 0.001$. With $g_{\text{eff,as-grown}}^{\uparrow\downarrow}$, the interfacial spin mixing conductance (ignoring the imaginary part) can be evaluated via:

$$G^{\uparrow\downarrow} = \frac{\left(\frac{e^2}{h}\right) g_{\text{eff}}^{\uparrow\downarrow}}{1 - 2\left(\frac{e^2}{h}\right) g_{\text{eff}}^{\uparrow\downarrow} / G_{\text{NM}}} \tag{2.24}$$

For Pt, resistivity-dependent spin torque measurements [75] give the estimation of its spin conductance as $G_{\text{Pt}} = 1.3 \times 10^{15}\ \Omega^{-1}\text{m}^{-2}$. Using this Pt spin conductance and $g_{\text{eff,as-grown}}^{\uparrow\downarrow}$ measured from the FMR, Eq.(2.24) results in $G^{\uparrow\downarrow} = 0.57 \times 10^{15}\ \Omega^{-1}\text{m}^{-2}$ in the as-grown CoFe/Pt, which is not far from a model calculation for the Co/Pt interface ($G^{\uparrow\downarrow} = 0.59 \times 10^{15}\ \Omega^{-1}\text{m}^{-2}$) [65] and a first principle calculation of the Sharvin conductance of Pt [68]. This suggests that the SML, which can bring in extra damping contribution [74] other than the spin pumping model, may not be significant in this case. We can then estimate the internal spin Hall angle of Pt θ_{SH}^{Pt} via the measured spin torque efficiency $\xi_{DL}^{\text{as-grown}} = 0.10$ with Eq. (2.17) and get $\theta_{SH}^{\text{Pt}} = 0.17$. This indicates that the spin transparency in this system is around 60%. On the other hand, similar calculation based on the enhanced magnetic damping, as shown in Fig. 2.6(b) yields an unphysical result, $G^{\uparrow\downarrow} < 0$, for the annealed CoFe/Pt. This unexpected result indicates that there is an extra magnetic damping contribution in the system likely from the SML effect, consistent with the decreased spin torque efficiency ($\xi_{DL}^{\text{annealed}} = 0.077 \pm 0.005$), which

may be a result of the formation of the dead layer at the CoFe/Pt interface upon annealing. Spin torque and magnetic damping measurements on the Co/Pt samples also reveal possible SML effect in those heterostructures [73]. After all, the above experiments demonstrate the critical role of the NM/FM interface in the spin transport process.

2.4 Origin of the field-like spin-orbit torque in NM/FM heterostructures

In the previous section, the discussion was basically focused on the damping-like spin torque. The SOT generally has two components that can be imbedded into the LLG equation to describe the magnetization dynamics, as mentioned in Chapter 1. In addition to the damping-like (DL) torque, the so-called field-like (FL) torque can also exist in the same material system. These two torques have distinguishable symmetries with respect to the magnetization direction (Eq. 1.14). Although the mathematical form of these two torques is relatively simple, their physical origin is much more unclear even though many studies have attempted to determine the properties of these spin torques.

The Rashba spin-orbit coupling interaction was firstly suggested to explain the experimental observation of in-plane-current-induced spin torques in NM/FM heterostructures [16,17]. The Rashba model is typically expected to generate a larger FL than DL torque, at least within the context of a Boltzmann equation or drift-diffusion analysis [65]. Alternatively, the strong SHE in the bulk of certain heavy metal (HM) materials was proposed to explain the spin torques in the same NM/FM thin-film

structures [46,47,76], in which case the absorption of the transverse polarized component of the spin current generally exerts a larger DL torque and reflection with some spin rotation can result in a smaller FL torque as described, for example, using the spin mixing conductance model [65]. After the proposal of the SHE scenario, it was supported later by studies of SOT excitation of nanomagnets and domain wall motion in HM/FM heterostructures, in which case both a DL torque from the SHE-induced spin current and an interfacial Dzyaloshinskii-Moriya interaction both play important roles in the SOT dynamic process [77–79].

However, large FL torque has indeed been observed in HM/FM systems where the FM is thin and magnetized out of plane [80], which seems to be puzzling given the dominant role of the SHE in the generation of DL torque. Several studies have reported behaviors of the FL torque in terms of its magnitude and the sign with respect to the thickness of the FM [81,82], the type of FM [83], the type of HM [84,85], the direction of the magnetization in FM [86,87] and temperature [80,87]. In the following sections, I will introduce our experimental measurements of the thickness and temperature (T) dependencies of current-induced spin-orbit torques, especially the FL component, in various HM/NM spacer/FM/Oxide heterostructures. Our experimental results indicate that the FL torque in these samples originates from the SHE in the HM.

2.4.1 The non-local FL torque in HM/spacer/FM heterostructure

The Rashba spin-orbit coupling is a local effect at the NM(HM)/FM interface where the spin polarization at the interface is coupled to the magnetization via the

exchange interaction thereby resulting an effective field (i.e. the FL component) [9]. On the other hand, the SHE model describes the transport of the diffusive spin current that carries angular momentum, which can be injected into the FM. As a result, the SHE-induced spin torques are non-local.

In order to confirm the non-local nature of the FL torque in HM/spacer/FM heterostructures, we sputtered a series of in-plane magnetized W(4)/Hf(t_{Hf})/$Fe_{60}Co_{20}B_{20}$(t_{FeCoB})/MgO(2)/Ta(1) samples, where $t_{Hf} = 0.25 - 2\mathrm{nm}$ and $t_{FeCoB} = 2 - 7$ nm, with the numbers in parentheses represent the nominal thickness in nm. The DC sputtering conditions were 2mTorr Ar pressure, 30 watts power. Here the Hf layer between the W and FeCoB layers serves as a spacer which allows the spin current generated in the W to diffuse into the FeCoB layer. Notice that the Hf layer itself has negligible SHE (see the sections below). By varying the Hf thickness, the amount of spin current can be controlled.

We measured the DL and FL torques with the ST-FMR techniques. For a fixed Hf spacer thickness, the ST-FMR signals were acquired from different FeCoB thicknesses. As shown in Fig. 2.7(a), the FMR spin torque efficiency ξ_{FMR} shows a strong FM thickness dependence, indicating a non-negligible FL torque (see Eq. 2.23). From fits to Eq. (2.23) (dashed lines in Fig. 2.7(a)) for a given Hf spacer thickness, the DL and FL spin torque efficiencies (ξ_{DL} and ξ_{FL}) as a function of t_{Hf} can be determined, with the results shown in Fig. 2.7(b). In our convention here the negative

signs of both ξ_{DL} and ξ_{FL} indicate a negative spin Hall ratio for W and a FL effective field that is antiparallel to the current-generated Oersted field. Both ξ_{DL} and ξ_{FL}

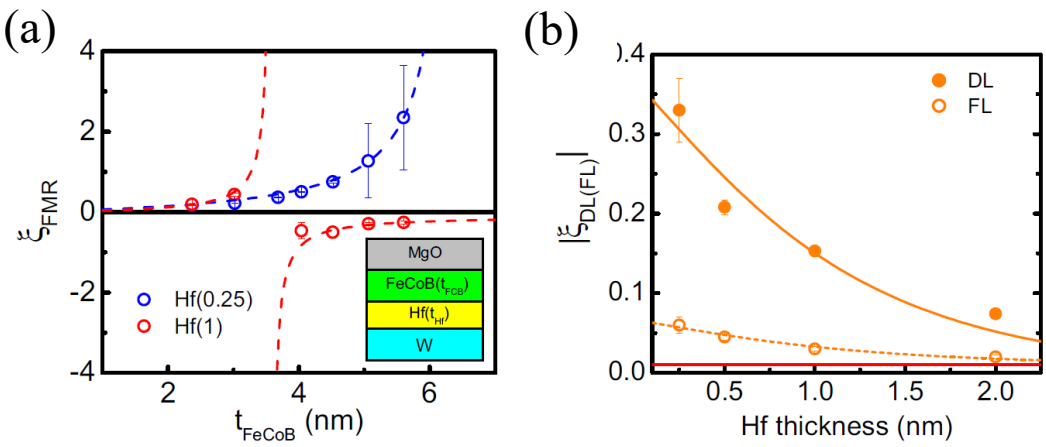

Figure 2.7: ST-FMR measurements on the W/Hf/FeCoB/MgO samples. (a) FMR spin torque efficiency as a function of t_{FeCoB}. (b) The DL and FL spin torques as a function of the Hf spacer thickness. The red solid line indicates a small residual FL spin torque efficiency (-0.010 ± 0.004). Figures reproduced from Ou et al. [88].

decrease as t_{Hf} increases and extrapolate to negligible values at large Hf thicknesses, in accord with the decreasing magnitude of spin current from W. After considering the relevant material parameters, we found that the spin current (and thus the DL torque) follows a t_{Hf} dependence, $1/(e^{t_{\mathrm{Hf}}/\lambda_{\mathrm{Hf}}} + P_{(\mathrm{Hf,W})} e^{-t_{\mathrm{Hf}}/\lambda_{\mathrm{Hf}}})$, where $P_{(\mathrm{Hf,W})} \approx 0.25$ [88]. Accordingly, the relatively well fit (solid line in Fig. 2.7(b)) to ξ_{DL} gives a self-consistent value of the spin diffusion length in Hf, $\lambda_{\mathrm{Hf}} = 0.9 \pm 0.2\mathrm{nm}$. We also found that $\xi_{FL}(t_{Hf})$ can be fitted with the same form with a small extra constant term $|\xi_{FL,0}|$, as shown in the dash line in Fig. 2.7(b):

$$|\xi_{FL}(t_{Hf})| = \frac{|\xi_{FL}(0)|}{e^{t_{Hf}/\lambda_{Hf}} + P_{(Hf,W)}e^{-t_{Hf}/\lambda_{Hf}}} + |\xi_{FL,0}| \quad (2.25)$$

The good fits in Fig. 2.7(b) indicate that both ξ_{DL} and ξ_{FL} are the result of a diffusive spin current from the underlying W that passes through the Hf layer. The non-local property of the FL torque observed here is consistent with previous studies reported for Py/Cu/Pt and CoFeB/Cu/Pt systems [81,85]. Also notice the fit for ξ_{FL} suggests a small residual FL component ($\xi_{FL,0} = -0.010 \pm 0.004$) when the Hf is in the thick limit and the spin current from W is negligible, which may be owed to a weak Rashba-type spin-orbit coupling at the Hf/FeCoB interface [89] or potentially the FeCoB/MgO interface.

2.4.2 Contribution to the FL torque at the FM/oxide interface

After we established that the majority of both the DL and FL torques result from the spin current generated by the SHE, we turned to the other aspects of the FL torque. As mentioned previously, the FL torque can be considerably stronger in perpendicularly magnetized (PM) samples, which typically have much thinner FM layers than in-plane magnetized samples. As shown in the following parts, we designed a series of experiments to show that the large FL torque in PM samples is strongly dependent on both t_{FM} and the details of the FM/Oxide interface.

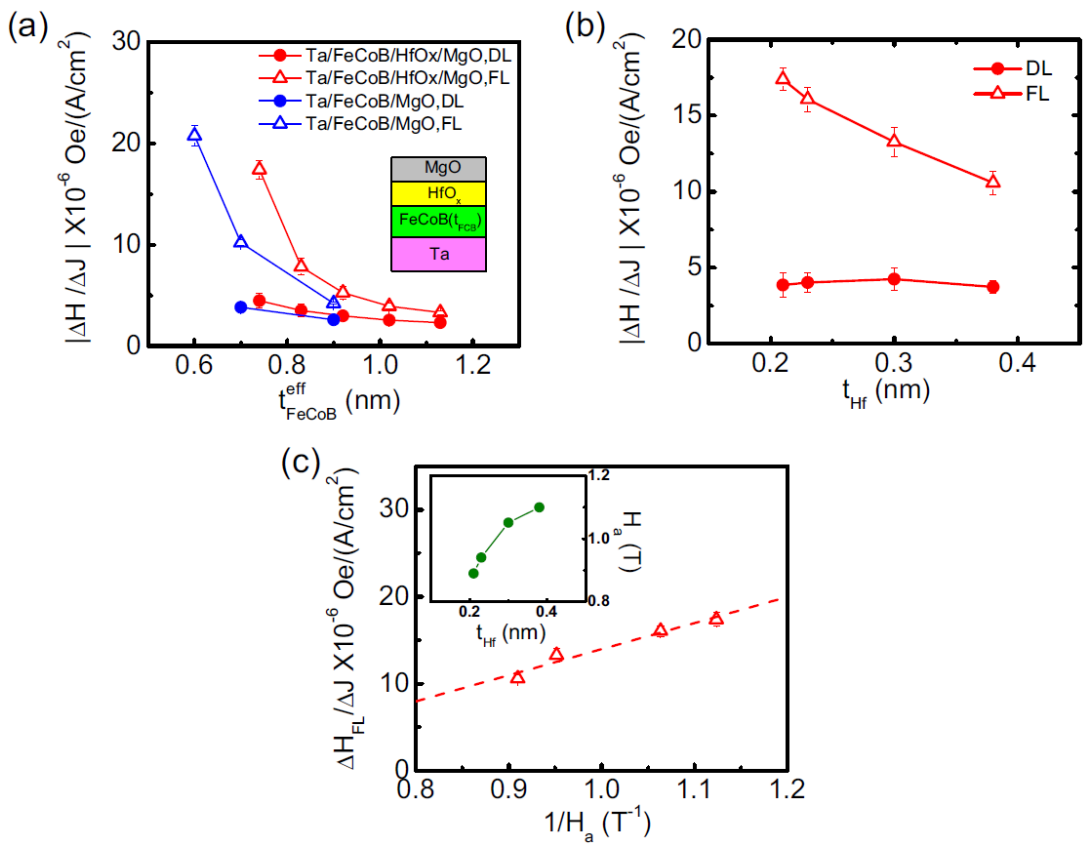

Figure 2.8: FM/oxide contributions to the FL torque. (a) The current-induced effective fields $\Delta H_{DL} / \Delta J_e$ and $\Delta H_{FL} / \Delta J_e$ as a function of t_{FeCoB} for a Ta/FeCoB/MgO and a Ta/FeCoB/HfOx(0.2)/MgO sample. (b) $\Delta H_{DL} / \Delta J_e$ and $\Delta H_{FL} / \Delta J_e$ as a function of the Hf passivation layer thickness. (c) $\Delta H_{FL} / \Delta J_e$ as a function of the inverse of the anisotropy field H_a. Inset: H_a for different Hf passivation layer thicknesses. Figures reproduced from Ou et al. [88].

To show that the strength of the FL torque indeed strongly depends on t_{FM}, we fabricated two series of PM samples: Ta(4)/FeCoB(t_{FeCoB})/MgO and Ta(6)/FeCoB(t_{FeCoB})/Hf(t_{Hf}) (oxidized)/MgO. In the latter case, $0 < t_{\mathrm{Hf}} \leq 0.4$ nm, and the Hf dusting layer was oxidized to form a thin HfO_x layer during the subsequent sputter

deposition of the MgO without any post-fabrication annealing (see Chapter 4 for more information about the Hf dusting in the formation of perpendicular magnetic anisotropy).

For these PM samples, we characterized the DL and FL spin torques via the harmonic response (HR) technique [48,90], in which the spin-torque-induced effective DL and FL fields, which are proportional to the DL and FL spin torques respectively, can be measured from the first and second harmonics Hall voltages for a given longitudinal current density, ΔJ_e ,under the external field sweeps:

$$\Delta H_{DL(FL)} = \frac{\Delta H_{L(T)} + 2\delta \cdot \Delta H_{T(L)}}{1 - 4\delta^2} \tag{2.26}$$

where $\Delta H_{L(T)} = -2 \frac{\partial V_H^{2\omega}}{\partial H_{L(T)}} \Big/ \frac{\partial^2 V_H^{\omega}}{\partial H_{L(T)}^2}$ is the harmonic response calculated from the ratio of the Hall voltages under the longitudinal(transverse) field sweep, and δ is the planar Hall correction ratio [90], the ratio of the effective planar Hall resistance to the effective anomalous Hall resistance

Figure 2.8(a) shows the effective fields per current density as measured by HR as a function of t_{FeCoB} , for t_{Hf} = 0 and 0.2 nm. Notice that the small Oersted field contribution has been subtracted from the $\Delta H_{FL} / \Delta J_e$ results. In both the FM/MgO and FM/HfO_x/MgO cases, $\Delta H_{FL} / \Delta J_e$ decreases rapidly as t_{FM} increases from 0.7 nm to 1.0 nm. For a given value of t_{FM} , the strength of the FL torque is stronger for the FM/HfO_x/MgO samples by approximately a factor of 2 compared to FM/MgO.

The above results indicates that $\Delta H_{FL} / \Delta J_e$ depends strongly on both t_{FM} and the composition of the FM/Oxide interface for the PM samples, while in the previous section our studies as a function of the thickness of a Hf spacer between the HM and the FM in PM samples show that the origin of this enhanced FL torque is a result from the spin current emitted from the HM, and the spin-orbit torques decay as a function of increasing Hf spacer thickness. Therefore, we can conclude that the enhanced FL torque in the PM samples must be mainly due to the portion of J_s from the HM, before dephasing and/or relaxing, that can pass through the FM layer and reach the FM/Oxide interface. As a result, for a very thin FM layer the spin scattering at that interface is able to affect the amount of spin accumulation there.

To support the conclusion that the FM/oxide interface plays an important role in the generation of large FL torque in thin FM samples, we also measured the $\Delta H_{DL} / \Delta J_e$ and $\Delta H_{FL} / \Delta J_e$ as a function of the thickness of an oxidized Hf dusting layer for a series of Ta(6)/FeCoB(0.8)/Hf(t_{Hf})/MgO samples, as shown in Fig. 2.8(b). As t_{Hf} increases from approximately one atomic layer (0.2 nm) to two (0.4 nm) there is only a small change in ΔH_{DL}, while ΔH_{FL} decreases markedly, by nearly a factor of two. The strong variation of the FL term with t_{Hf} is probably related to the more complete passivation of the FM surface by a slightly thicker Hf layer. As shown in the inset to Fig. 2.8(c), the perpendicular anisotropy field H_a increases as t_{Hf} becomes thicker, which supports the above attribution. In Fig. 2.8(c) we plot $\Delta H_{FL} / \Delta J_e$ as a function of $1/H_a$, which indicates that as the strength of the interfacial anisotropy increases, τ_{FL} decreases

linearly. This phenomenological behavior is also observed in Ta/FeCoB/MgO PM samples where we found that $\Delta H_{FL} / \Delta J_e$ for that system also varies as $1/H_a$ when different annealing temperatures were employed to modify the perpendicular magnetic anisotropy [88]. This suggests a tradeoff between the spin-orbit interaction that creates the PMA at FCB/Oxide interfaces [91] and the spin relaxation mechanism responsible for FL spin torque.

2.4.3 Temperature dependence of the spin torques in HM/NM/FM/oxide heterostructures

In order to get more insight into the properties of the spin torques, especially the FL component, we performed systematic temperature (*T*) dependence measurements on the spin torques in the HM/NM/FM/oxide heterostructures with different heavy metal materials. We found that neither ξ_{DL} nor ξ_{FL} has a significant *T* dependence for the in-planed magnetized W/Hf/FeCoB/MgO samples [88] studied in the previous section; on the other hand however, the FL torque contribution from the FM/Oxide interface is strongly temperature dependent, which we tentatively ascribe to the *T*-dependent spin-flip scattering at the FM/Oxide interface. The *T*-dependent spin torque measurements on the PM samples are shown in Fig. 2.9.

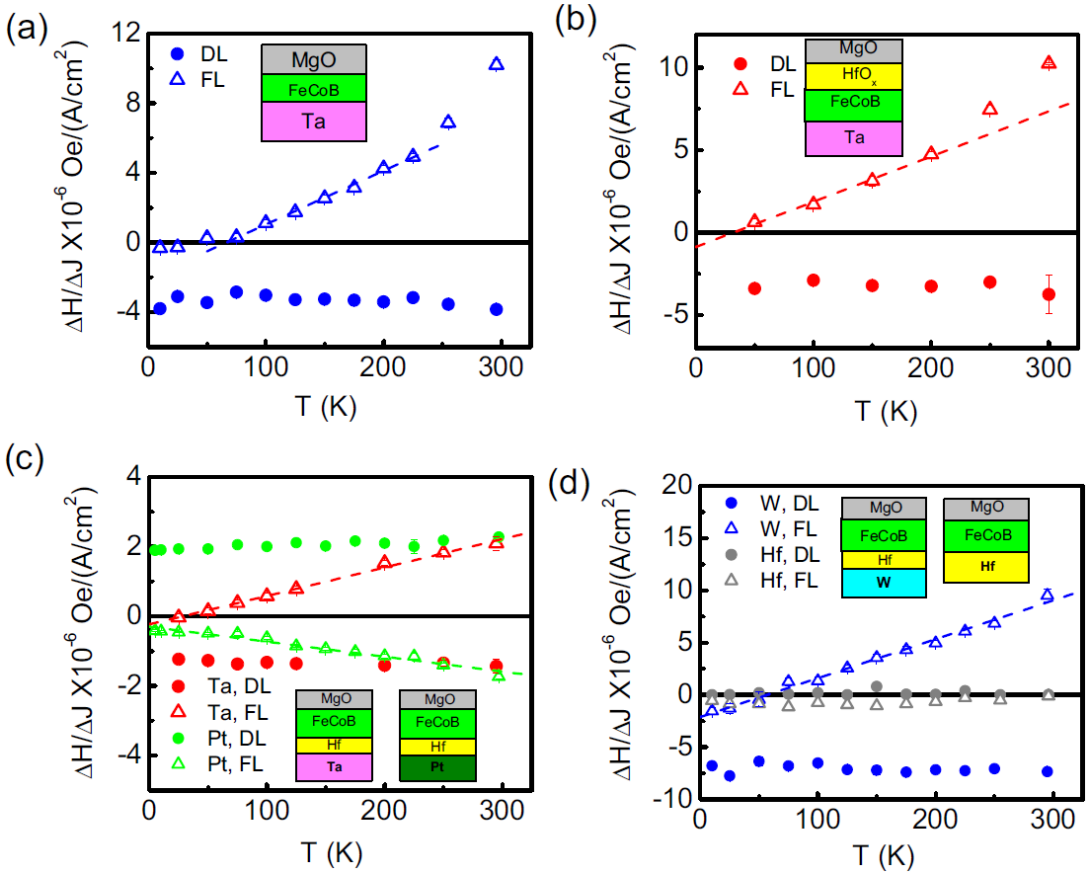

Figure 2.9: Temperature dependent measurements of the spin torques in various HM/NM/FM/oxide heterostructures: (a) Ta(4)/FeCoB(0.8)/MgO; (b) Ta(6)/FeCoB(0.8)/HfOx(0.2)/MgO; (c) Ta(4)/Hf(1)/FeCoB(1)/MgO and Pt(4)/Hf(0.5)/FeCoB(1)/MgO; and (d) W(4)/Hf(1)/FeCoB(1)/MgO and Hf(4)/FeCoB(1)/MgO. The dashed lines are fits to the linear portion of the $\Delta H_{FL}(T) / \Delta J_e$ variation. Figures reproduced from Ou et al. [88].

Figure 2.9(a) and (b) show results obtained respectively from an annealed Ta(4)/FeCoB(0.8)/MgO sample and an as-grown Ta(6)/FeCoB(0.8)/Hf(0.2)/MgO sample, that is without and with the Hf dusting layer. While $\Delta H_{DL} / \Delta J_e$ shows little variation with *T*, there is a strong *T*-dependence in $\Delta H_{FL} / \Delta J_e$ in both cases as *T* goes towards zero. The behavior of $\Delta H_{FL} / \Delta J_e$ for the sample without the Hf dusting is quite similar to that reported previously [15,23]. Below 250 K, ΔH_{FL} decreases in a quasi-linear way with decreasing *T*, approaching zero around 70 K. It then departs from linearity to vary more slowly, becoming slightly negative as *T* goes to zero. Notice the convention here is that a negative ΔH_{DL} corresponds to a negative spin Hall angle. As for the FL torque in the Hf dusting sample (Fig. 2.9(b)), it also shows a strong *T* dependence that is even more linear for *T* below 200 K to at least 50 K. From these results we can conclude that the FM/HfO_x interface is responsible for the linear *T* dependence of the FL torque in all these samples at low *T*.

For additional insight we also studied PM samples with different HM base layers and with a thin Hf spacer layer between the HM and the FM: Ta,Pt,W(4)/Hf(t_{Hf})/$Fe_{60}Co_{20}B_{20}$(t_{FeCoB})/MgO(2)/Ta(1), where $t_{Hf} = 0.5$ or 1 nm and $t_{FeCoB} = 0.7 - 1$ nm . The thin Hf spacer layers in these samples can enhance the PMA in the HM/Hf/FeCoB/MgO heterostructures without sacrificing all the spin current from the HM in determining the strength of the SOT [92].

Figure 2.9(c) shows $\Delta H_{DL}(T)$ and $\Delta H_{FL}(T)$ as generated in a Ta and a Pt based sample with the Hf spacer and Fig. 2.9(d) shows results from a W sample ($t_{Hf} = 1$ nm

for the Ta and W samples and $t_{Hf} = 0.5$ nm for the Pt sample). In all three cases, ΔH_{DL} is again nearly *T*-independent, increasing just slightly with decreasing *T*. The different signs for ΔH_{DL} are consistent with the different signs of the spin Hall ratio θ_{SH} (negative for Ta and W, positive for Pt). The sign of $\Delta H_{FL}(T)$ at *T* = 300 K is in all cases opposite to that of θ_{SH}, being + for Ta and W, and – for Pt. In all cases $\Delta H_{FL}(T)$ decreases quite linearly with decreasing *T* down to ~ 5 K and exhibits a sign change at low *T* for Ta and W, which can be most strongly seen in the W sample. Since W has the highest spin Hall ratio, the W base layer provides the strongest incident spin current at the Hf/FM interface and results in the largest field-like torque being exerted there, in comparison to the Ta/Hf/FM and Pt/Hf/FM samples. $\Delta H_{FL}(T)$ at the lowest temperature for the W sample corresponds to a FL spin torque efficiency $\xi_{FL} \approx -0.03$, which is consistent with the IPM ST-FMR measurement for the same structure with the same Hf thickness (Fig.2.7 (b)).

In order to eliminate the possible contribution from the Hf spacer or Hf/FeCoB interface in these spin-torque measurements, we measured $\Delta H_{DL}(T)$ and $\Delta H_{FL}(T)$ in a control sample having only a 4 nm Hf base layer, that is Hf(4)/FeCoB(1)/MgO, as also shown in Fig. 2.9(d). $\Delta H_{DL}(T)/\Delta J_e$ is negligible over the full *T* range, while $\left|\Delta H_{FL}(T)/\Delta J_e\right|$ is quite small, $\leq 1\times10^{-6}$ Oe/(A/cm^2) with little *T* variation, indicating both the SHE or Rashba spin-orbit coupling from the Hf spacer layer is negligible.

From the non-local spin torque and temperature dependence measurements, we conclude that the dominant mechanism in generating ΔH_{FL} is the scattering of the

incident SHE-generated J_s at each of the two interfaces of the FM. For the spin torque that is exerted only at the NM/FM interface (e.g. in the in-plane magnetized samples) the result is a comparatively small field-like torque, $\Delta H_{FL} < \Delta H_{DL}$, and has weak T dependent. When in thin PM samples where a significant J_s reaches the FeCoB/Oxide interface, it results in a stronger contribution to the FL torque at $T \sim 300$ K with a sign opposite to θ_{SH} (under our sign convention) and with $\Delta H_{FL} \geq \Delta H_{DL}$, but this contribution decreases rapidly close to zero at low T, leaving only the weaker spin current dependent contribution to ΔH_{FL} from the HM/FM interface, where the spin scattering can perhaps be treated via the scattering-matrix spin mixing conductance scenario where spin rotation during the reflection of part of J_s will result in a field-like torque [65]. Our results here also show that at the FM/Oxide interface, the strength of H_a is inversely correlated with the strength of the field-like torque (see for example Fig. 2.8(c)), which indicates that the electronic states at the FM/Oxide interface may be distributed between those that generate the interfacial anisotropy and those that provide the spin relaxation pathway with the distribution depending on annealing or the Hf dusting passivation.

CHAPTER 3

BEYOND 5d HEAVY METALS: SPIN-ORBIT TORQUE IN NOVEL MATERIAL SYSTEMS

3.1 Introduction

Since the discovery of the current-induced SOT in NM/FM heterostructures, most of the studies have been focused on the 5d transition heavy metals as the spin sources, for example Pt [16,46], beta-Ta [47] and beta-W [76]. It has been demonstrated that such 5d heavy metals typically have strong SHE (e.g. with SHE angles larger than 5%) due to the large spin Hall conductivity these elements have, which is related to their large atomic numbers and thus strong spin-orbit interaction, as predicted from first principle calculations [30]. In addition to the 5d elements, some 4d transition metals, such as Pd and Au, have also been reported to have sizable SHE, such as discussed in Ref. [8,93] for example.

The demonstration of a large SHE in AuCu-I-type metallic antiferromagnets (AF) in inverse spin Hall measurements on Py/$X_{50}Mn_{50}$ (X=Pt, Ir, Pd, Fe) systems [94] in 2014 stimulated strong interest in the spin-orbit torque studies in antiferromagnetic materials [95,96]. In these AF with collinear antiferromagnetic order, theory has predicted that the strength of the SHE depends on not only the atomic number of X (i.e. relative strength in the spin-orbit interaction), but also the crystal orientation and the staggered AF magnetization [94]. In addition to the collinear AF materials, experimental observation of a strong SHE in triangular AF $IrMn_3$ has also been

reported [97,98], in which the SHE is attributed to the large intrinsic spin Hall conductivity resulting from its chiral AF order [98]. Instead of its traditional role serving as the pinning layer in magnetic tunneling junctions, the strong SHE in AF as a spin current source, combined with its special properties such as the AF order and exchange coupling, may provide new functionalities in the spintronics applications [99,100]. In the first part of this chapter, I will discuss our study on the strong SHE in the antiferromagnetic material PtMn and demonstrate the deterministic SOT-assisted magnetization switching in PtMn/FM heterostructures.

Compared to the non-magnetic transition metals and antiferromagnets that has no net internal magnetization, the detection of SOT from ferromagnetic materials is more challenging, which may be at least due to the fact that the internal magnetization of the FM tends to quickly dephase the transverse spin polarization of the spin current generated from, for example, the SHE in the FM. Therefore, it is quite unusual that sizable SHE has been observed in ferromagnetic Py via inverse spin Hall measurements [101,102]. Alternatively, in a temperature region near the ferromagnetic transition of a diluted ferromagnet, when the internal magnetization has not yet well established, the SHE may exhibit unexpected behavior corelated to the strong spin fluctuations in that temperature region. For instance, abnormality in the inverse spin Hall signal in the vicinity of the ferromagnetic transition of the diluted FM Ni_xPd_{1-x} has been reported [103]. In the second part of this chapter, I will introduce our experimental studies on the strong enhancements of the SHE in ferromagnetic FePt alloys near the Curie temperature due to spin fluctuations.

3.2 The strong spin Hall effect in the antiferromagnetic PtMn

3.2.1 Sample growth and fabrication

All samples in this study [104] were grown by DC sputtering (with RF magnetron sputtering for the MgO layer). The sputtering chamber has a base pressure $< 8\times10^{-8}$ Torr, with the DC sputtering condition using 2mTorr Ar pressure, 30 watts power, which results in low deposition rates (≤ 0.02 nm/s). The PtMn alloy is sputtered from a 2-inch planar $Pt_{50}Mn_{50}$ target directly. All of the PtMn samples have a Ta seeding layer as a smooth template base layer and the thin MgO/Ta top layers as the capping layers to protect the stack from oxidation.

We deposited six series of samples:

(A)||Ta(1.5)/PtMn(8)/Co(t_{Co})/MgO(1.6)/Ta(1.5);

(B) ||MgO(1.6)/Co(t_{Co})/PtMn(8)/MgO(1.6)/Ta(1.5)

(C) ||Ta(1.5)/PtMn(8)/FeCoB(t_{FeCoB})/MgO(1.6)/Ta(1.5)

(D) ||MgO/FeCoB(t_{FeCoB})/PtMn(8)/MgO(1.6)/Ta(1.5)

(E) ||Ta(1.5)/PtMn(8)/FeCoB(t_{FeCoB})/MgO(1.6)/Ta(1.5)

and (F) ||Ta(1.5)/PtMn(8)/Hf(0.25)/FeCoB(0.8)/MgO(1.6)/Ta(1.5)

in which "||" denotes the Si/SiO_2 substrate and the numbers in the parenthesis are in unit of nm. Series (A) to (D) are for in-plane-magnetized (IPM) ST-FMR measurements, while (E) and (F) are perpendicularly magnetized (PM) samples for harmonic response

(HR) measurements. We characterized the magnetic properties of the unpattern samples via the VSM technique and therefore determined the effective magnetization and dead layer thickness. In the discussion below, the effective FM thickness t_{FM}^{eff} has been subtracted with the dead layer thickness. We then patterned the thin films into the rectangular bar and Hall cross structures, via the standard photolithography and ion etching process, for ST-FMR and HR detection.

3.2.2 SOT measurements via ST-FMR for the IPM samples

Figure 3.1(a) shows the typical ST-FMR measurement schematic is illustrated in Fig. 1a. The ferromagnetic resonance signal resulting from the RF input current is measured by lock-in detection. And during the ferromagnetic resonance, the voltage consists of the symmetric and antisymmetric components of anisotropic magnetoresistance response, and the FMR spin torque efficiency ξ_{FMR} can be evaluated from the ratio of the symmetric to the antisymmetric component. Figure 3.1(b) shows the results ξ_{FMR} as a function of Co thickness t_{Co} for both the series (A) (main) and (B) (inset) order samples. Notice that (A) and (B), and (C) and (D) have opposite PtMn/FM deposition orders, in which I will call the former as the “standard” order (SO) while the latter as the “reverse” order (RO) for convenience. The reason we utilized these two stack orders was because previous experiments indicate that stack order may affect the strength of the measured spin torques [73].

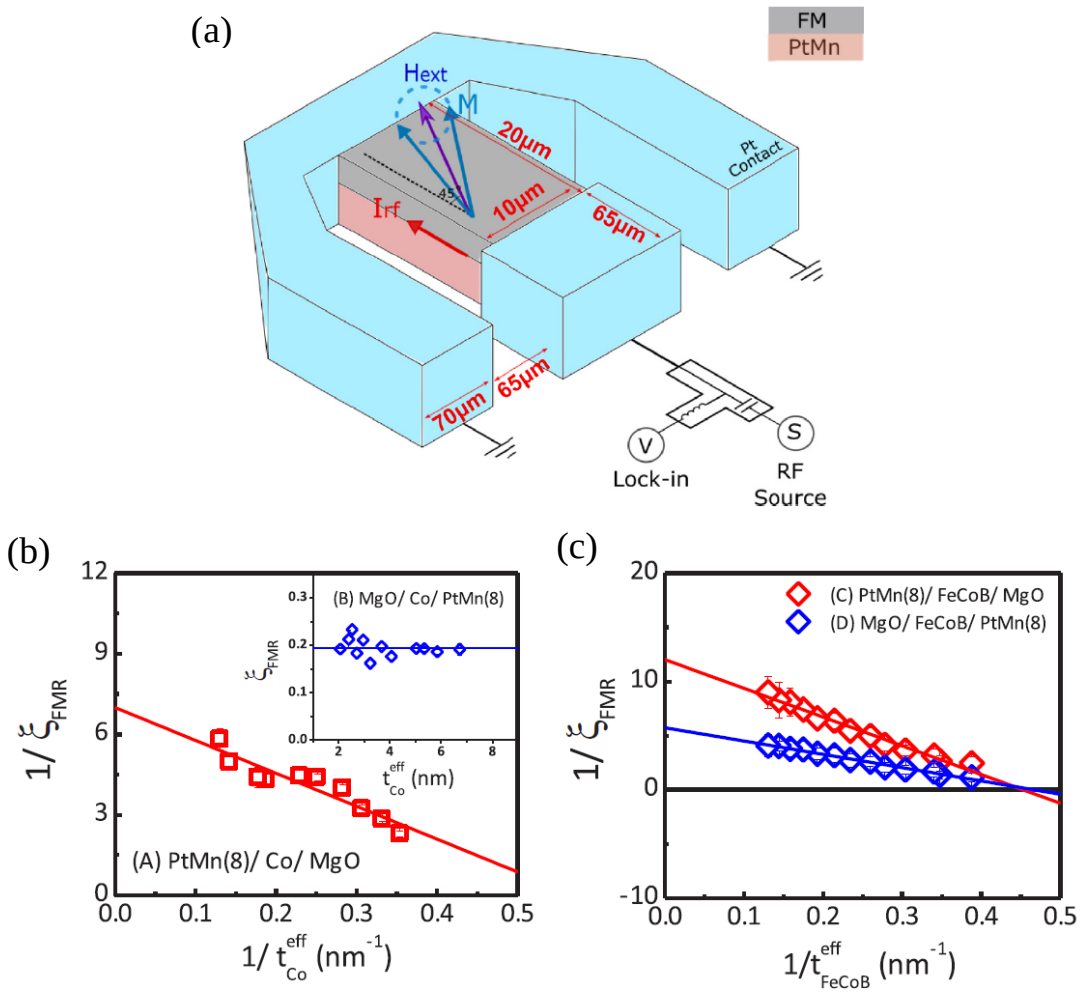

Figure 3.1: ST-FMR measurements on the IPM PtMn/FM samples. (a) Schematic of ST-FMR measurement. (b) The inverse of the ST-FMR measured spin torque efficiency, $1/\xi_{FMR}$, as a function of the inverse of the effective thickness for the Co series (A) samples (red squares). Inset: ξ_{FMR} as a function of $t_{\mathrm{Co}}^{\mathrm{eff}}$ for series (B) samples (blue squares). (c) $1/\xi_{FMR}$ as a function of $1/t_{\mathrm{FeCoB}}^{\mathrm{eff}}$ for the series (C) (red squares) and series (D) (blue squares) samples. Figure reproduced from Ou et al. [104].

As can be seen in Fig. 3.1(b), the obvious t_{Co} dependence in ξ_{FMR} indicates a nonnegligible FL torque in the SO PtMn/Co samples (see Eq. (2.23), Chapter 2). By fitting $1/\xi_{FMR}$ versus $1/t_{\mathrm{Co}}$ using Eq. (2.23), the DL spin torque efficiency ξ_{DL} can be determined from the $1/t_{\mathrm{Co}} = 0$ intercept and the FL spin torque efficiency ξ_{FL} can be determined from the slope of the plot, when ξ_{FL} is effectively independent of t_{Co}. For the RO Co/PtMn samples, ξ_{FMR} shows little t_{Co} dependence, indicating ξ_{FL} is negligible and $\xi_{FMR} \approx \xi_{DL}$ (Fig. 1b inset). From this we obtain $\xi_{DL} = 0.16 \pm 0.01$ and $\xi_{FL} = -0.040 \pm 0.008$ for the SO samples and $\xi_{DL}(\text{average}) = 0.19 \pm 0.02$ and $\xi_{FL} \simeq 0$ for the RO samples (according to the sign convention we have, the positive sign for ξ_{DL} corresponds to the same sign of the anti-damping torque as for Pt, while the minus sign for ξ_{FL} indicates that the FL effective field is opposite to the Oersted field).

In order to test whether the spin torque in the PtMn/FM bilayer depends on the type of FM, we performed the same ST-FMR measurements on series (C) and (D) by replacing the Co with $Fe_{60}Co_{20}B_{20}$ (FeCoB) for the FM layer in the PtMn/FM structures. Figure 3.1(c) shows $1/\xi_{FMR}$ vs. $1/t_{\mathrm{FeCoB}}^{\mathrm{eff}}$ as obtained for these two series of samples (C) and (D). From the linear fits to the plots we obtained $\xi_{DL} = 0.096 \pm 0.003$, $\xi_{FL} = -0.043 \pm 0.003$ for the SO series (C) samples and $\xi_{DL} = 0.174 \pm 0.004$, $\xi_{FL} = -0.036 \pm 0.002$ for the RO series (D) samples.

The different DL torque efficiencies for SO and RO samples, and that between Co and FeCoB as the FM material, may be related to difference in the strength of SML

at the PtMn/FM interface. In order to attain more insight into the interface/SML in these PtMn/FM samples, we measured their enhanced damping constant $\Delta\alpha(t_{FM}^{-1})$ via the ST-FMR measurements and evaluated the spin mixing conductance with Eq. 2.16. The $\Delta\alpha(t_{FM}^{-1})$ in all four series yielded the effective spin mixing conductance $G_{\text{eff}}^{\uparrow\downarrow} > 0.7\times10^{15}\Omega^{-1}\text{m}^{-2}$ [104]. With the spin conductance of PtMn, $G_{\text{PtMn}} = 0.37\times10^{15}\Omega^{-1}\text{m}^{-2}$, as determined from the resistivity and spin diffusion length measurements, this $G_{\text{eff}}^{\uparrow\downarrow}$ results in an unphysical (negative) value for $G^{\uparrow\downarrow}$, suggesting that there should be a significant SML at the PtMn/FM interface and/or a non-ideal damping enhancement at the other FM interface.

3.2.3 SOT measurements via HR technique for the PM samples

As an independent measurement, we also fabricated the series (E) samples with SO and measured the SOT via the HR technique on a specific thickness of the FeCoB ($t_{\text{FeCoB}} \approx 0.8\text{nm}$) that has the highest out-of-plane anisotropy field ($H_{an} \approx 1.8\,\text{kOe}$) in this sample series without any post-fabrication annealing treatment. Using the measurement protocol of Ref. [48,49] on Hall-bar samples, we determined for this sample a DL spin torque efficiency $\xi_{DL} = 0.11 \pm 0.02$ and a FL spin torque efficiency $\xi_{FL} = -0.04 \pm 0.02$, which is in accord with the ST-FMR values obtained via ST-FMR from the IPM series (C) samples with the same layer structure but thicker FeCoB.

In order to reduce the potential SML at the PtMn/FM that is detrimental to the spin transport without sacrificing too much spin current, we fabricated the sample (F)

that has a very thin Hf spacer (0.25nm) between the PtMn(8nm) and FeCoB(0.8nm). The ultrathin Hf may help to enhance the spin transmission and thus ξ_{DL}. This sample also exhibits perpendicular magnetic anisotropy (i.e. magnetized out-of-plane) without any post-fabrication annealing. The HR measurement results in a high DL spin torque efficiency $\xi_{DL} = 0.24 \pm 0.03$ in this sample, indicating that the spin transparency can indeed be improved by engineering the interface. Since the spin transparency is always less than unity, the result here indicates that the internal spin Hall ratio of the PtMn is $\theta_{SH}^{\mathrm{PtMn}} > 0.24$.

3.2.4 Spin diffusion length measurements

In addition to the SOT, spin diffusion length is also an important material parameter that governs the spin transport process. In order to determine the spin length ($\lambda_{\mathrm{s}}^{\mathrm{PtMn}}$) in our PtMn alloy, we fabricated a set of samples, series (G), with the multilayer stack being ||Ta(1)/PtMn(t_{PtMn})/Hf(0.8)/FeCoB(0.7)/MgO, where t_{PtMn} ranged from 2 to 8 nm, to measurement the DL effective field as a function of t_{PtMn} via the HR technique. The result is shown in Fig. 3.2 (a).

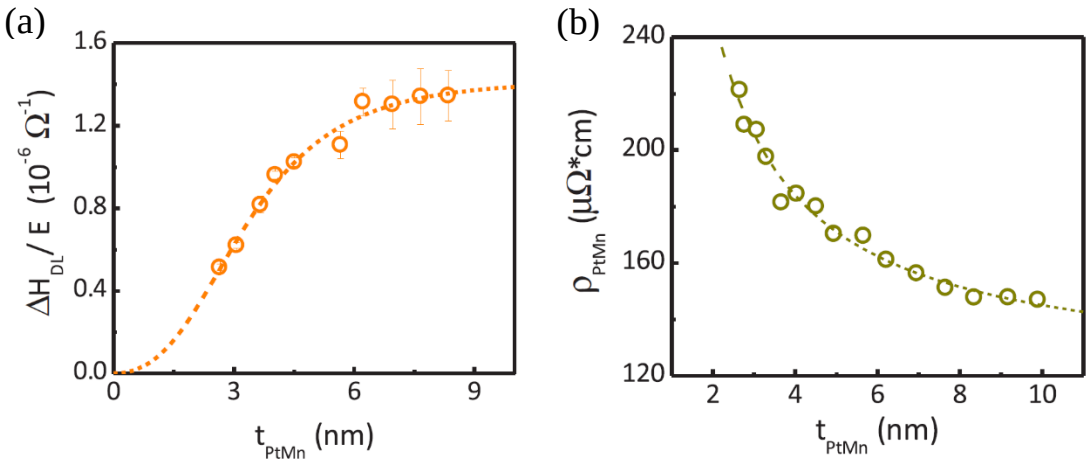

Figure 3.2: Spin diffusion length and resistivity measurements of PtMn. (a) Damping-like effective field per unit applied electric field for the series (G) samples as a function of PtMn thickness t_{PtMn}. (b) Average resistivity of different thicknesses of PtMn. The dash line is a fit of the empirical function $\rho_0 + \rho_s / t_{\mathrm{PtMn}}$ to the data, where ρ_0 and ρ_s are represent the bulk and interfacial scattering contributions to the resistivity. Figure reproduced from Ou et al. [104].

As there is little spin current from the Hf spacer that was determined from our previous research (see Chapter 2), we can use a trilayer spin diffusion model evaluate the DL effective field per electrical field [104]:

$$\frac{\Delta H_{DL}}{E} = \frac{\sigma_{SH}}{4\pi M_s t_{FM}^{\mathrm{eff}}} \frac{G_A}{G_{\mathrm{PtMn}} \tanh(t_{\mathrm{PtMn}} / \lambda_s^{\mathrm{PtMn}}) + G_B} (1 - \mathrm{sech}(t_{\mathrm{PtMn}} / \lambda_s^{\mathrm{PtMn}})) \qquad (3.1)$$

where $4\pi M_s$ is the magnetization, t_{FM}^{eff} is the effective thickness of the FM layer excluding the dead layer and d_{PtMn} is the thickness of the PtMn, σ_{SH} is the spin Hall conductivity of PtMn ($\sigma_{SH} = \sigma_{\mathrm{PtMn}} \theta_{SH}^{\mathrm{PtMn}} \hbar / (2e)$), $G_{\mathrm{PtMn}} \equiv \sigma_{\mathrm{PtMn}} / \lambda_s^{\mathrm{PtMn}}$ is the spin

conductance of PtMn and G_A and G_B are parameters depending on the Hf spacer and spin mixing conductance at the Hf/FeCoB interface.

Figure 3.2(a) shows a fit to the series (G) results with Eq. (3.1), which gives a spin diffusion length of PtMn $\lambda_{\mathrm{PtMn}} = 2.1\mathrm{nm}$. This result is considerably larger than the value 0.5 nm previously reported [94] from inverse spin Hall effect measurements on NiFe/PtMn. This may be due to the significant SML at the NiFe/PtMn interface that affect the estimation of λ_s in an ISHE measurements as in the the Co/Pt case [18]. The lower DL spin torque efficiency that we find without the Hf layer, which is similar to that found in the previous ISHE study [8], suggests that there also could be a significant SML in those PtMn/FM cases, perhaps due to reaction of a component of the FM with Mn at the PtMn/FM interface.

Notice that by using Eq. (3.1), we assume that the spin diffusion length is independent of t_{PtMn}. If however the spin relaxation process in PtMn satisfies the Elliot-Yafet scattering mechanism, one would expect $\lambda_s^{\mathrm{PtMn}} \propto 1/\rho_{\mathrm{PtMn}}$ when the PtMn resistivity ρ_{PtMn} aslo varies with film thickness. In order to test this, we measured ρ_{PtMn} as a function of t_{PtMn}, as shown in Figure 3.2(b). It clearly shows that ρ_{PtMn} is not a constant and it is dependent of t_{PtMn}. In this case, we can use a "rescaling" method introduced in Ref.[27] to fit our data in Fig. 3.2(a), which yields $\lambda_s^{\mathrm{PtMn}} = 2.3\mathrm{nm}$ for the bulk spin diffusion length [104], and also a spin conductance for PtMn $G_{\mathrm{PtMn}} = 1/(\lambda_s^{\mathrm{PtMn}} \rho_{\mathrm{PtMn}}) = 0.37 \times 10^{15} \Omega^{-1}\mathrm{m}^{-2}$.

3.2.5 Current-induced magnetization switching

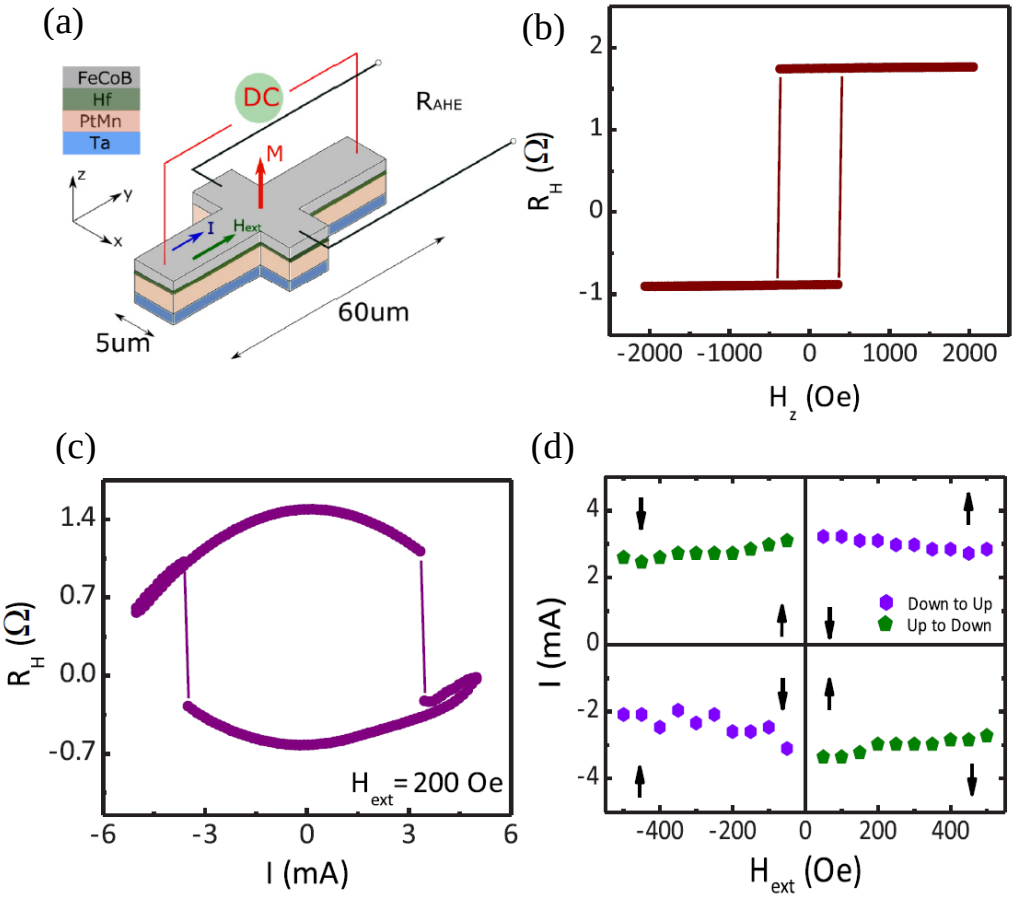

Figure 3.3: Current-induced magnetization switching using the SOT from PtMn. (a) Schematic of the Hall-bar samples used to study field- and current-induced switching. (b) Magnetic field switching of a series (H) sample with the field perpendicular to the sample plane. (c) Current-induced switching of the same sample with an external magnetic field (200 Oe) applied in-plane along the current direction. (d) Phase diagram of the current-induced switching behavior. Figure reproduced from Ou et al. [104].

One of the key goals in the research of SOT is to realize efficient current-induced switching using the SOT. After we determined the large spin torque efficiency from the PtMn, we demonstrated the potential of using it as the source of spin-transfer torque for high-efficiency magnetic switching by performing current-induced switching with a Hall bar structure (schematic in Fig. 3.3(a)) using an as-deposited ||Ta(1)/PtMn(4)/Hf(0.5)/FeCoB(0.8)/MgO/Ta(1.5) sample (H) that possessed strong PMA, and that exhibited sharp and abrupt magnetic switching in its anomalous Hall signal under an out of plane field as shown in Fig. 3.3(b). (Notice that this sample had $\xi_{DL} \approx 0.10$ based on HR measurements, consistent with the spin attenuation effect of the thicker Hf layer and the reduced spin current from the thinner (4nm) than optimal PtMn.)

A typical deterministic current switching loop, read out from the anomalous Hall resistance, is shown in Fig. 3.3(c) with an external field $H_y = 200$ Oe collinear to the current flow. This external field was required to overcome the Dzyaloshinskii-Moriya interaction (DMI) at the Hf/FeCoB interface and a magnetization reversal process that proceeds by domain nucleation followed by spin-torque-driven domain expansion [79]. By repeating the current-induced switching experiments under different external fields, we were able to determine the spin-torque current switching phase diagram of the same sample (here 2 mA corresponds to a current density 9×10^6 A/cm^2 in PtMn) as illustrated in Fig. 3.3 (d). Our studies here thereby not only highlight the large SHE in PtMn but also successfully demonstrate its potential as an efficient spin source for spin-torque-assisted magnetization manipulation in spintronics applications.

3.3 Strong enhancement of the spin Hall effect by spin fluctuations near the Curie point of Fe_xPt_{1-x} alloys

As mentioned in the beginning of this chapter, most of the research about SOT so far have focused on the non-magnetic transition metals. Some reports indicate that even in a ferromagnet with its internal magnetization, a sizable SHE can still be observed. However, until now little has been known about the behavior of the SHE in a ferromagnetic system near its transition temperature (i.e. the Curie temperature) where there are strong spin fluctuations, especially when there are introduced dopants serving as the scattering centers that can be described by the extrinsic SHE mechanism.

By alloying the element Pt which has a strong spin-orbit interaction with ferromagnetic Fe atoms, the resulted Fe_xPt_{1-x} alloys belong to a class of ferromagnetic alloys that have long been known to exhibit giant magnetic moments per ferromagnetic solute, and where the Curie temperature can be tuned by the concentration of Fe. The Fe_xPt_{1-x} alloys are also well known for their robust magnetic anisotropy properties arising from the strong conduction electron spin-orbit interaction with the Fe orbital moment [106,107], and for the dependence of the magnetic state on the chemical order [108,109], in addition to their other interesting magnetic properties such as the large anomalous Hall effects (AHE) in Fe_xPt_{1-x} thin films [110–112]. These features of Fe_xPt_{1-x} suggest that it could be a promising material for the generation of spin currents by the extrinsic SHE. In the following sections I will introduce our study on the enhancement of the SHE and interfacial spin mixing conductance near the Curie temperature of Fe_xPt_{1-x} alloys [113].

3.3.1 Sample fabrication and characterization

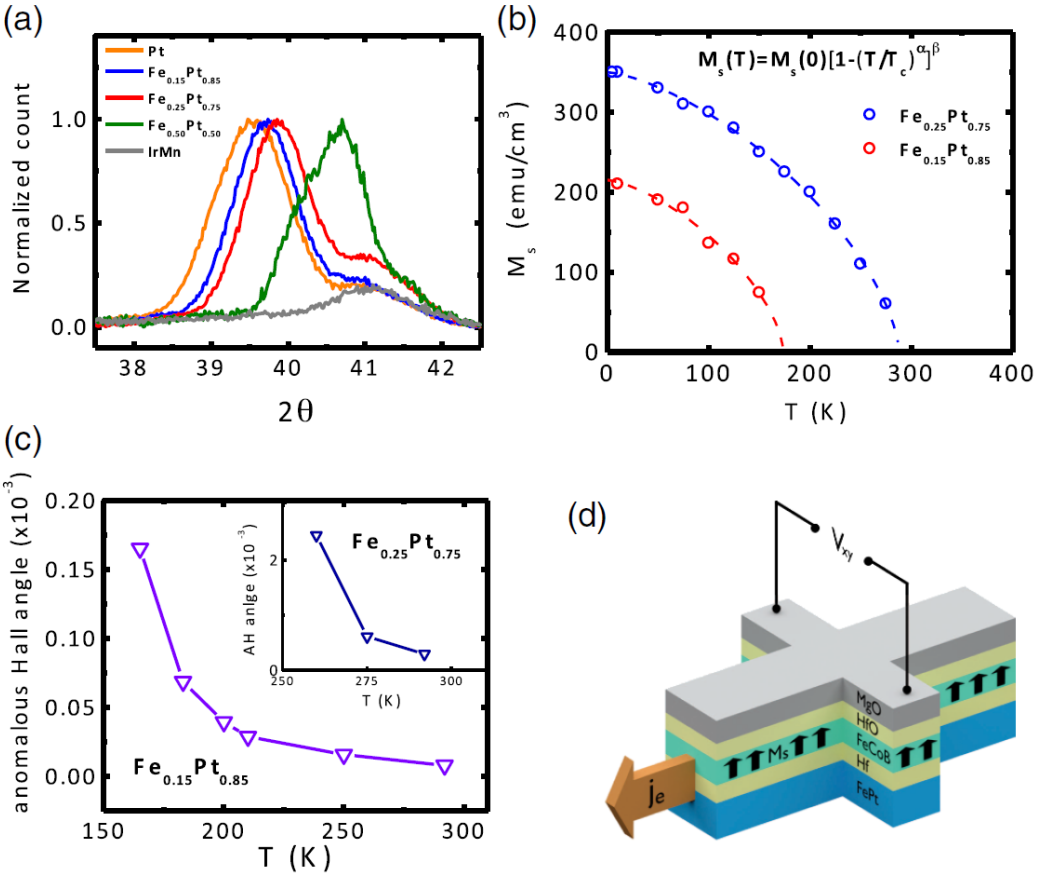

Figure 3.4: Sample characterizations and anomalous Hall measurements of the FePt alloys. (a) XRD measurements on the samples: $IrMn_3(10)/F_{0.50}Pt_{0.50}(10)/MgO$, $IrMn_3(10)/Fe_{0.25}Pt_{0.75}(10)/MgO$ and $IrMn_3(10)/Fe_{0.15}Pt_{0.85}(10)/MgO$, and two control samples: $IrMn_3(10)/Pt(1)/MgO$ and $IrMn_3(10)/Pt(8)/MgO$. (b) Temperature dependent VSM measurements on the samples $IrMn_3(10)/Fe_{0.25}Pt_{0.75}(10)/MgO$ and $IrMn_3(10)/Fe_{0.15}Pt_{0.85}(10)/MgO$. The dashed lines are fits to the empirical equation $M_s(T) = M_s(0) \cdot (1-(T/T_c)^{\alpha})^{\beta}$. (c) Temperature dependence of the anomalous Hall angle of the samples $IrMn_3(10)/Fe_{0.15}Pt_{0.85}(10)/MgO$ (main) and $IrMn_3(10)/Fe_{0.25}Pt_{0.75}(10)/MgO$ (inset). (d) Schematic of the Hall bar device. Figure reproduced from Ou et al. [113].

Two different sets of Fe_xPt_{1-x} thin films consisting of different Fe concentrations were fabricated at room temperature via DC magnetron sputtering: in one case the nominal composition was $Fe_{0.15}Pt_{0.85}$ and in the other $Fe_{0.25}Pt_{0.75}$. All samples were prepared in a deposition chamber with a base pressure $< 5\times10^{-8}$ Torr. The dc sputtering condition was 2mTorr Ar pressure. The Fe_xPt_{1-x} alloy was grown by co-sputtering from two pure sputtering targets (i.e. Fe and Pt targets). Heterostructures of substrate/Ta/IrMn/Fe_xPt_{1-x}/MgO/Ta were used for thin film characterization and substrate/Ta/IrMn/Fe_xPt_{1-x}/Hf/FeCoB/Hf/MgO/Ta stacks were used for the SOT measurements. After fabrication, these samples were then annealed in an in-plane magnetic field (2000 Oe) in a vacuum furnace at 300C for 1 h to enhance the PMA. For measurements of the AHE and SOT, Hall bar devices with lateral dimensions of $5\times60\,\mu m^2$ were patterned via photolithography and ion milling (see the sample schematic in Fig. 3.4(d)).

I first performed sample characterization via x-ray diffraction (XRD) measurements on two multilayer samples with the layer structures: $IrMn_3$(10)/$Fe_{0.15}Pt_{0.85}$(10)/MgO and $IrMn_3$(10)/$Fe_{0.25}Pt_{0.75}$(10)/MgO (the number in parentheses is the thickness in nanometers), where the $IrMn_3$ layer was included to provide antiferromagnetic pinning of the Fe_xPt_{1-x} layers when cooled to well below their Curie points. The 10nm Fe_xPt_{1-x} layers are thick enough that in the experiments to be considered below the $IrMn_3$ does not contribute any significant SOT on the free magnetic layer [113]. The (111) XRD peaks for the $Fe_{0.15}Pt_{0.85}$ and the $Fe_{0.25}$ $Pt_{0.75}$ samples are shown in Fig. 3.4(b), together with the separate 10 nm Pt, $Fe_{0.50}Pt_{0.50}$ and

IrMn films for comparison. As the Fe concentration increases, the reasonably narrow (111) peak shifts to higher 2θ angle, indicating a decrease in the unit cell size with increased Fe content. The lack of evidence of a (110) peak in the XRD of these samples whose presence would indicate significant chemical order [114] (The small peak at $2\theta \approx 41^o$ in Fig.1a is due to the $IrMn_3$ base layer) is as expected from the use of room temperature deposition. Resistivity measurements of the films showed only a weak temperature dependence, decreasing by less than 10% from room temperature to 160 K, indicating the dominance of impurity scattering. On the other hand, the room temperature resistivity of the films did vary with Fe content, from $\rho_{Pt}(10) \approx 15\mu\Omega\bullet\text{cm}$ to $\rho_{Fe_{0.15}Pt_{0.85}}(10) \approx 55\mu\Omega\bullet\text{cm}$ to $\rho_{Fe_{0.25}Pt_{0.75}}(10) \approx 75\mu\Omega\bullet\text{cm}$, indicating an increased electron scattering rate with increased Fe content.

To further characterize the ferromagnetic character of these alloys, I performed temperature-dependent VSM measurements of the samples (Fig. 3.4(b)). At sufficiently low temperature, both $Fe_{0.15}Pt_{0.85}$ and $Fe_{0.25}Pt_{0.75}$ were found to be ferromagnetic, and the spontaneous magnetization $M_s(T)$ can be fitted to the empirical function $M_s(T) = M_s(0) \cdot (1-(T/T_c)^{\alpha})^{\beta}$ [115], yielding a Curie temperature of $T_c \approx 174\,K$ for the $Fe_{0.15}Pt_{0.85}$ sample and $T_c \approx 288\,K$ for the $Fe_{0.25}Pt_{0.75}$ sample.

I also determined the AHE in these alloys. In Fig. 3.4(c) I show the temperature dependence of the "anomalous Hall angle" $= \rho_{xy} / \rho_{xx}$ of the $Fe_{0.15}Pt_{0.85}(10)$ and $Fe_{0.25}Pt_{0.75}(10)$ samples as measured in a magnetic field H_z = 2 kOe applied perpendicular to the plane of the film. (Here ρ_{xx} is the resistivity in the direction of

current flow and r_{xy} is the transverse Hall resistivity). As can be seen in the $Fe_{0.15}Pt_{0.85}(10)$ sample, there is a significant AHE at high temperature that increases gradually as the temperature is decreased toward $200\,\mathrm{K}$ and even more as *T* decreases below T_c, qualitatively as would be expected for the case of strong skew scattering from the Fe ions. In the inset of Fig. 3.4(c), a similar temperature dependence trend for the $Fe_{0.25}Pt_{0.75}(10)$ sample below its Curie temperature is shown.

3.3.2 SOT measurements on FePt/Hf/FeCoB heterostructures

In order to quantify the SOT from the SHE in FePt, I fabricated two sets of FePt-based multilayer samples with perpendicular magnetized FeCoB layers:

$IrMn_3(10)/Fe_{0.15}Pt_{0.85}(10)/Hf(1)/FeCoB(1)/Hf(0.35)/MgO$ (A),

and $IrMn_3(10)/Fe_{0.25}Pt_{0.75}(10)/Hf(0.8)/FeCoB(1)/Hf(0.35)/MgO$ (B),

and measured the SOT via the HR technique introduced earlier. The very thin (0.35nm) Hf insertion layer between the FeCoB and the MgO enhanced the interfacial magnetic anisotropy energy density (and thus the PMA strength, see Chapter 4 for more information).

I first measured the response of the anomalous Hall resistance of one of the $Fe_{0.15}Pt_{0.85}$ heterostructure Hall bars (sample A) to an applied out-of-plane field H_z at different temperatures between 300 K and 140 K, as shown in Fig. 3.5. The sharp field-induced switching events, with an increasing coercivity upon decreasing temperature, are from the PMA FeCoB layer. When the temperature is lower than the Curie

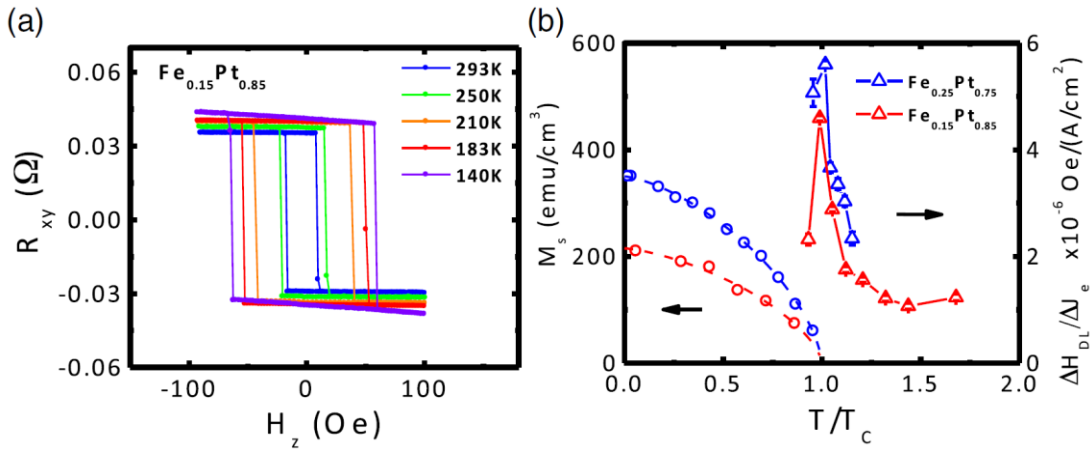

Figure 3.5: Hall and harmonic response measurements of the FePt/Hf/FeCoB heterostructures. (a) Temperature-dependent AHE resistance of sample (A) $Fe_{0.15}Pt_{0.85}$. (b) Dampinglike effective fields of sample (A) $Fe_{0.15}Pt_{0.85}$ and (B) $Fe_{0.25}Pt_{0.75}$ as a function of normalized temperature T / T_c . Their temperature dependent magnetizations are also plotted here for comparison. Figure reproduced from Ou et al. [113].

temperature of $Fe_{0.15}Pt_{0.85}$ there is also a quasi-linear background, which is much larger than the ordinary Hall effect and instead is due to the AHE of the in-plane magnetized FePt layer. The AHE resistance for sample (B) is similar [116].

In Fig. 3.5(b) I show the temperature dependences of the DL effective fields for both sample (A) and sample (B) as measured from the HR technique, plotted as a function of T/T_c, where T_c are determined from the fits to the magnetization of the samples (Fig. 3.4(b)). The measurement for sample (A) ($Fe_{0.15}Pt_{0.85}$) is from room temperature 293 K to T = 160 K, and for sample (B) ($Fe_{0.25}Pt_{0.75}$) from 330 to 275 K. For sample (A) for which we have measurements starting around 100 degrees above T_c,

we see that the DL effective field per current density $\Delta H_{DL} / \Delta J_e$ is more or less constant until $T/T_c \approx 1.44$ (250 K). Below that it begins to increase, at first gradually, then very rapidly reaching a peak near T_c (172K) more than 3 times its 293 K value. This significant temperature-dependent behavior is dramatically different from that of the DL torque found with conventional heavy metal systems [80,88]. Below T_c, the DL effective field drops rapidly. As can be seen in Fig. 3.5(b), the behavior of sample (B) over the same scaled temperature range above and below T_c, is quite similar. This similarity, despite the 35% difference in resistivity, and 67% difference in Fe concentration between sample (A) and (B), is consistent with skew scattering being the dominant spin Hall effect in these materials.

3.3.3 Spin mixing conductance and spin diffusion length measurements

In addition to the SOT, the spin mixing conductance and spin diffusion length are two other important physical parameters that are relevant to the spin transport process. In order to measure the spin mixing conductance, I fabricated a $Fe_{0.25}Pt_{0.75}$(10)/Hf(0.25)/FeCoB(7.3)/MgO sample and measured its enhanced magnetic damping $\Delta\alpha \equiv \alpha(t_{FM}) - \alpha_0$, where α_0 is the intrinsic Gilbert damping constant, via the resonant linewidth measurements made by flip-chip field-modulated FMR. The enhanced magnetic damping can be related to the effective spin mixing conductance via $g_{\text{eff}}^{\uparrow\downarrow} = 4\pi M_s t_{FeCoB} \Delta\alpha / (\gamma\hbar)$ (Eq. 2.16). I observed a somewhat similar peak in magnetic damping of the FeCoB layer in our samples as they were cooled through the T_c of the

FePt. As shown in Fig. 3.6(a), $g_{\text{eff}}^{\uparrow\downarrow}$ increases rapidly as T moves below T_c, and then drops abruptly by more than a factor of three to a value ($\approx 30\,\text{nm}^{-2}$) much closer to that expected for a typical FM/Pt interface [73]. The temperature-dependent behavior observed here is distinctly different from the temperature-insensitive $g_{\text{eff}}^{\uparrow\downarrow}$ in Pt/ferromagnet bilayer systems [117].

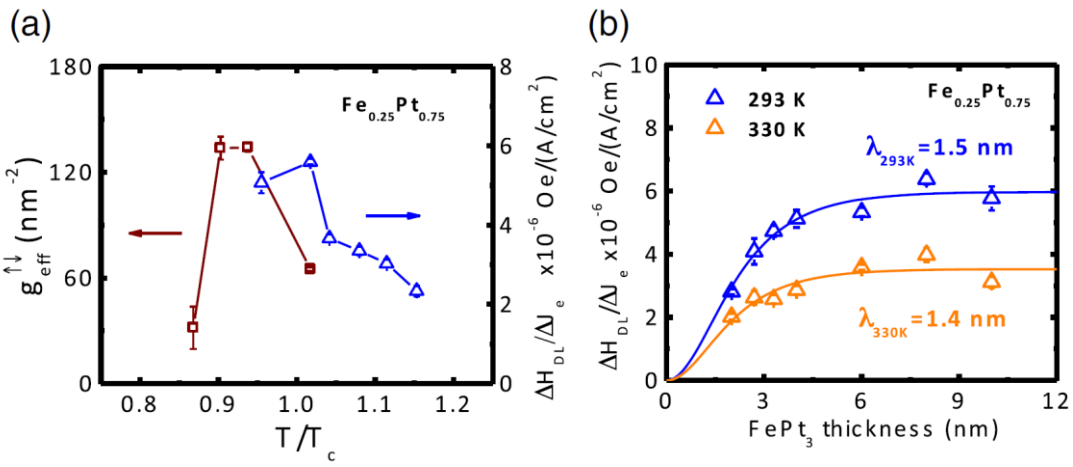

Figure 3.6: Spin mixing conductance and spin diffusion length measurements. (a) The effective spin mixing conductance of an in-plane magnetized $Fe_{0.25}Pt_{0.75}$(10)/Hf(0.25)/FeCoB(7.3) sample as determined by a flip-chip FMR measurement of the damping parameter for the FeCoB resonance. The temperature dependence of the DL effective field of sample (B) is also plotted here for comparison. (b) Spin diffusion length measurement of the samples $Fe_{0.25}Pt_{0.75}$(t)/Hf(0.8)/FeCoB(1). Figure reproduced from Ou et al. [113].

As for the spin diffusion length in FePt, we measured λ_s by fabricating a series of PMA samples without the IrMn layer $Fe_{0.25}Pt_{0.75}$(t_{FePt})/Hf(0.8)/FeCoB(1)/Hf(0.35)/MgO/Ta(1) where the thickness t_{FePt} of the FePt alloy was varied from 2 to 10 nm. The measured damping-like effective fields as

a function of t_{FePt} for these samples are plotted in Fig. 3.6(b) for two different temperatures 293 and 330 K, *i.e.* in the near vicinity of T_c and somewhat above it. The solid lines are a fit of the function $\Delta H_{DL}(t_{FePt})/\Delta J_e = (\Delta H_{DL}(\infty)/\Delta J)(1 - \mathrm{sech}(t_{FePt}/l_s)$ [65] to the data. The results at the two temperatures are quite similar, with $\lambda_s \approx 1.5$ nm.

3.3.4 Current-induced magnetization switching

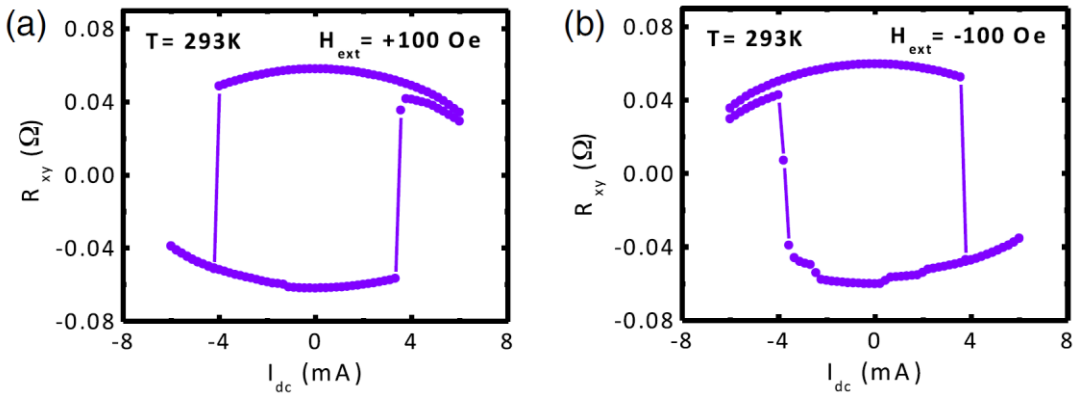

Figure 3.7: Current-induced magnetization switching of sample (B) $IrMn_3(10)/Fe_{0.25}Pt_{0.75}(10)/Hf(0.8)/FeCoB(1)/Hf(0.35)/MgO$ at room temperature under an external magnetic field along the current direction. Figure reproduced from Ou et al. [113].

I further confirm the strength of the SHE in the FePt alloys with current-induced switching measurements. In Fig. 3.7 I show the switching behavior of sample (B) as measured at $293\,K$, in close vicinity to T_c. The direction of current-induced switching is reversed upon changing the sign of a small in-plane applied magnetic field, in a way

that is characteristic of DL torque SHE switching [118]. The switching current density for this case was $\approx 6\times10^{6}$ A/cm^{2}.

3.3.5 Enhancement of the SHE and spin mixing conductance due to spin fluctuations

Our experimental results above indicate that the enhancement of the SHE and spin mixing conductance, both of which reach their peak values in the vicinity of the Curie temperature of the FePt alloys, are closely related to the strong spin fluctuations that occur in this system near T_c. These interesting phenomena may be understood via the comparison to the AHE. More than half a century ago Kondo [119] developed a theorical model for the scattering of conduction electrons by localized orbital moments to explain an anomaly in the magnetoresistance and AHE of ferromagnetic Ni and Fe near their Curie points [120]. In the AHE case, Kondo attributed the anomaly to increasingly stronger spin fluctuations as $T \to T_c$ from below. This sheds light on our SHE results here since AHE and SHE are generally considered to have very similar mechanisms (see Chapter 1). Recently Gu et al. [121] extended Kondo's theory to explain results by Wei et al. [103] on inverse spin Hall effect (ISHE) measurements of NiPd alloys near their T_c, including the effect of correlations between neighboring localized moments. We surmise that spin fluctuations are also the origin of the strong peak in the SOT torque (spin current) that we observe with the FePt alloys.

If spin fluctuations are indeed the origin of the enhanced SHE in the FePt alloys near T_c, then it is predicted [122] that there should also be an enhancement of the

effective interfacial spin-mixing conductance $g_{\text{eff}}^{\uparrow\downarrow}$ between the FeCoB and FePt alloy in the vicinity of the latter's Curie point. This is indeed what we observed in the enhanced magnetic damping experiments as discussed in the previous section. Interesting, similar enhancement of the magnetic damping near the Neel temperature of antiferromagnet spin sinks by inverse spin Hall measurements [123] and spin pumping [124] have been reported recently, which are also attributed to the spin fluctuation near the transition temperatures in those systems.

CHAPTER 4

MANIPULATION OF THE INTERFACIAL PERPENDICULAR MAGNETIC ANISOTROPY ENERGY AT THE FERROMAGNET/OXIDE INTERFACE

4.1 Introduction

The results and discussions from the previous chapters have indicated the importance of the (NM/FM/oxide insulator) thin film heterostructure (illustrated in Fig. 1.1) as a material platform for the study of SOT related phenomena. So far, all those discussions have been focused on how critical the interfaces are during the spin transport process (chapter 2) and how to generate strong spin current from new SHE material systems (chapter 3). With regard to the magnetization dynamics in a given system under the SOT, the properties of the FM also play an important role. I have mentioned the enhanced magnetic damping of the FM as a directly relevant material parameters in the process of the spin transport and spin dynamics. Another property is the effective magnetization (or demagnetization field) of the FM, which is related to the perpendicular magnetic anisotropy (PMA) of the FM layer [125].

Among all kinds of the magnetic anisotropy, the shape anisotropy of the FM is one of the simplest, which depends on the shape of the FM material and it is a natural result of the magnetic dipolar energy [125]. Specifically speaking for a thin FM layer with in-plane magnetization, the magnetic dipolar energy density can be calculated as [125,126]:

$$E_{\text{demag}} = -\frac{\mu_0}{2} M_z^2 \tag{4.1}$$

which is also referred to as the demagnetization energy. The minus sign on the right-hand side of Eq. (4.1) follows the convention that a negative magnetic energy means the magnetization is in-plane (while a positive one indicates the magnetization is perpendicular to the plane). The direct conclusion from the Eq. (4.1) is that for a thin film system, the magnetization will always tend to stay in-plane if there is no another magnetic anisotropy contribution.

However, there can be other magnetic anisotropy contributions from both the bulk and the interface(surface) of the FM layer. If K_v is the bulk anisotropy energy density and K_s is the interfacial anisotropy energy density, then for the thin film FM, the total effective magnetic anisotropy energy density K_{eff} can be written as [126]:

$$K_{\text{eff}} = \left(K_v - \frac{\mu_0}{2} M_s^2 \right) + \frac{K_s}{t_{FM}} \tag{4.2}$$

From Eq. (4.2) it is easy to see that if K_v and/or K_s is positive and large enough to compensate the demagnetization energy, the total energy density K_{eff} can be a positive value and thereby the magnetization can have out-of-plane configuration. While the bulk anisotropy contribution can be from the crystalline or magneto-elastic effects [125], the interfacial anisotropy energy is usually related to the spin-orbit interaction between the FM and the adjacent layers [126].

The observation of strong interfacial PMA at the FeCoB/MgO interface in Ta/FeCoB/MgO heterostructure [127] has opened up a new avenue for perpendicular magnetic tunneling junction (p-MTJ) applications [128] (see Fig. 4.1), as high TMR and robust PMA can be achieved in the same material system with proper post-fabrication annealing treatments. In this FeCoB/MgO system, the interfacial PMA originates from the spin-orbit interaction in the hybridized 3d Fe-2p O bonding, as pointed out by first principle calculations [91,129], although experiments indicates that the buffer layer under FeCoB is important for the formation of PMA as well [128,130].

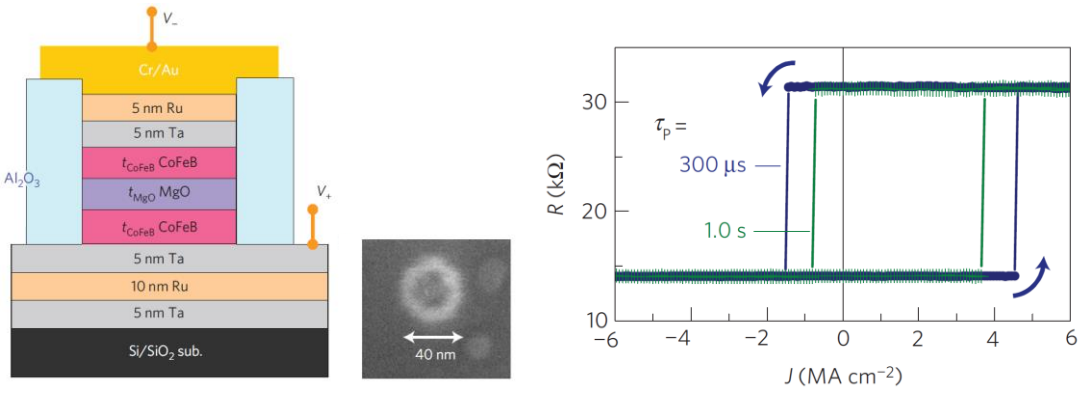

Figure 4.1: Schematic and current-induced magnetization switching of a FeCoB/MgO/FeCoB perpendicular MTJ. Figures reproduced from Ikeda et al. [127].

The realization of the robust PMA in FeCoB/MgO systems also provide a platform to manipulate domain walls in perpendicularly magnetized nanowire structures and drive novel magnetic chiral structures such as skyrmions via SOT [77,78,131,132].

Moreover, even for in-plane magnetized MTJs, by lowering the effective magnetization of the FM layer via the interfacial PMA effect may be beneficial for a more efficient SOT-assisted magnetization switching of the nanopillar structures (see chapter 5 for more discussion). In the following sections, I will introduce our experimental studies on the manipulation of the interfacial PMA energy at the FeCoB/MgO interface by inserting an ultrathin layer with other materials between the FeCoB and MgO. This material "dusting" technique can yield strong PMA without any post-fabrication annealing treatment that compromise the layers in the magnetic heterostructure due to materials intermixing or diffusion at the interface, while at the same time maintaining excellent thermal stability (PMA can be further enhanced by annealing to at least $400\ ^{o}C$). I will also show that this dusting technique can result in PMA in system with FM materials in addition to FeCoB, indicating its great potential for engineering magnetic thin film heterostructures for spintronics research and applications.

4.2 Strong perpendicular magnetic anisotropy energy density at Fe alloy/HfO_2 interfaces

In this section, I will discuss our results on controlling the PMA at the Fe alloy/MgO interfaces by depositing one to two atomic layers of Hf onto the Fe alloy before the subsequent rf sputter deposition of the MgO layer, which oxidized the ultrathin Hf into HfO_2. This HfO_2 insertion generates a strong interfacial PMA energy density both with and without any post-fabrication annealing treatment [133].

4.2.1 Sample growth and x-ray photoelectron spectroscopy characterizations

In this research all the samples were prepared via DC sputtering (with RF magnetron sputtering for the MgO layer), with a base pressure $< 4\times10^{-8}$Torr . Similar to our other research, the sputtering condition was 2mTorr Ar pressure, 30 watts power. In order to form the interfacial HfO_2, I firstly deposited an ultrathin Hf dusting layer (<0.5nm) on the FM layer (e.g. FeCoB) with a low deposition rate of $0.01\,\text{nm/s}$. Next a MgO layer was subsequently sputtered on the Hf layer with a growth rate of $0.005\,\text{nm/s}$ (at 100 watts power, 2 mTorr Ar), a process that oxidized the Hf. I also used a thin top Ta film as a capping layer to protect the underlayers from degradation due to atmospheric exposure. Unpatterned films were used for x-ray photoelectron spectroscopy (XPS) and VSM characterizations. Then the thin film heterostructures were fabricated into $5\times60\,\mu\text{m}^2$ Hall bars for anomalous Hall measurements. All the samples were baked at 115 $^{\circ}C$ for 1 min twice during the standard photolithography fabrication for photoresist treatment. Both as-deposited and annealing samples were prepared, in which we annealed the samples to various temperatures in a vacuum furnace.

I firstly characterized our samples by performing the XPS experiments to determine the oxidation level in the FeCoB/HfO_2/MgO dusting structure, since the complete oxidation of the insulator at the Fe alloy/oxide interface is believed to be critical for the formation of PMA in HM/Fe alloy/oxide heterostructures [91]. The XPS experiments are performed on three sets of as-deposited samples: (A) Si/SiO_2/Ta(6)/FeCoB(t_{FeCoB})/HfO_2(t_{Hf})/MgO(2)/Ta(1) with a range of HfO_2

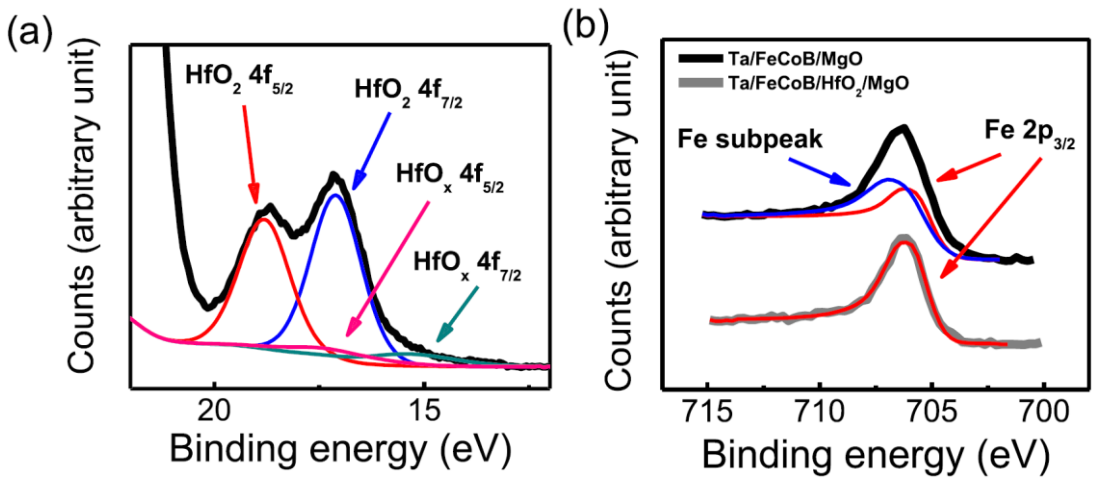

Figure 4.2: XPS spectra from (a) HfO2 4f and (b) Fe 2p spectral regions for the as-grown samples Ta(6)/FeCoB(1.2)/HfO2(0.2)/MgO/Ta(1) and Ta(6)/FeCoB(1.3)/MgO/Ta(1). Figures reproduced from Ou et al. [133].

thicknesses, and two control series with different dusting layers, (B) $Si/SiO_2/Ta(6)/FeCoB(t_{FeCoB})/TaO_x(t_{Ta})/MgO(2)/Ta(1)$ with a Ta dusting layer, and (C) $Si/SiO_2/Ta(6)/FeCoB(t_{FeCoB})/MgO(2)/Ta(1)$ without any dusting layer (the numbers in parentheses are the thicknesses in nm). Ion etching was used to remove most of the Ta capping layer before performing XPS. As shown in Fig. 4.2(a), the HfO_2 $4f_{7/2}$ and $4f_{5/2}$ peaks can be clearly observed at 17.1 eV and 18.8 eV in the XPS spectra. There is also a very small sub-oxide peak at ~ 16.0 eV and but there is no evidence for the Hf metallic $4f_{7/2}$ peak at 14.3 eV, which indicates that the Hf became fully oxidized during the deposition of MgO.

To achieve strong PMA, the HfO_2 layer should be able to provide optimized interfacial Fe-O bonds at the FeCoB/HfO_2 interface, which suggests that the Fe alloy should not be overly oxidized beyond the Fe-O bonds [91]. Fig. 4.2(b) shows for the sample (A) the XPS $2p_{3/2}$ peak of Fe at 706.0 eV, which can be well fit with the narrow asymmetric spin-split peak function characteristic of metallic Fe [134]. Compared to sample (A), the Fe $2p_{3/2}$ peak in sample (C) without the Hf dusting layer is much broader with a high energy tail indicative of substantial oxidation of the surface Fe during the direct deposition of MgO by rf sputtering [135] (Fig. 4.2(b)). I also examined the Fe XPS signal for a series (B) sample with Ta as the dusting layer (0.3 nm). It yielded a metallic signal indistinguishable from the Hf case, again indicating protection of the ferromagnetic surface from significant oxidation from the Ta dusting layer. However as can be seen in the following section, the magnetic characteristics of the Hf and Ta dusting heterostructures are quite different.

4.2.2 PMA enhancement duet to Hf dusting in Ta based heterostructures

I characterized the magnetic properties of these sample via VSM measurements. The magnetic moment per area as a function of t_{FeCoB} for a set of series A samples (Hf dusting) and also for series B samples (Ta dusting), as measured by VSM, is shown in Fig. 4.3(a). The linear fit to the Hf dusting series (A) gives a saturation magnetization of $M_s = 1260\,\mathrm{emu/cm^3}$ and a very small apparent "dead layer" thickness $t_d \approx 0.1\,\mathrm{nm}$, both consistent with previously reported results from as-deposited

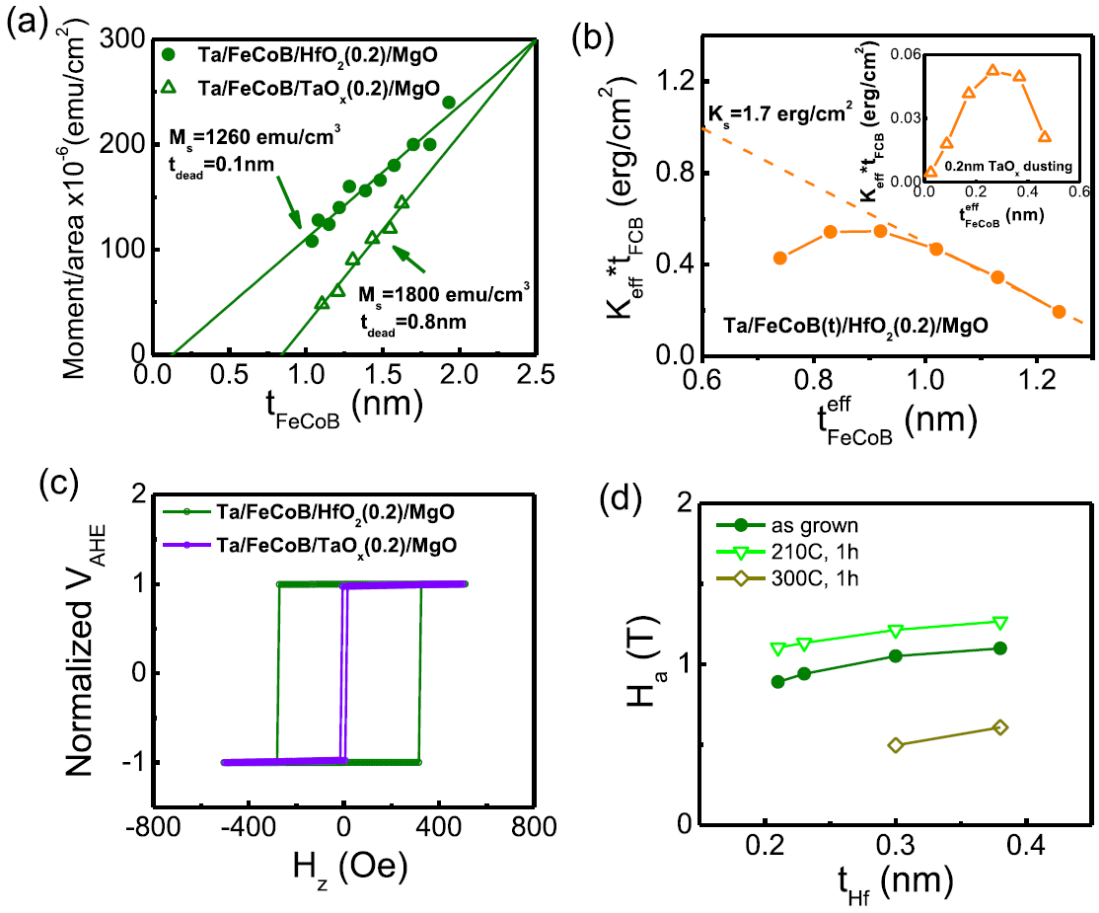

Figure 4.3: Enhanced PMA in Ta based heterostructure with Hf dusting. (a) VSM measurements of magnetization, (b) effective anisotropy energy density K_{eff} determined from anomalous Hall measurements as a function of in-plane magnetic field, and (c) anomalous Hall measurements as a function of out-of-plane magnetic field, for the as-grown samples Ta(6)/FeCoB(t_{FeCoB})/HfO_2(0.2)/MgO/Ta and Ta(6)/FeCoB(t_{FeCoB})/TaO_x(0.2)/MgO/Ta. The solid and dashed straight lines are linear fits to the data. (d) The perpendicular anisotropy fields of Ta(6)/FeCoB(0.8)/HfO_2(t_{Hf})/MgO/Ta samples as deposited and after different post-fabrication annealing treatments. Figures reproduced from Ou et al. [133].

Ta/FeCoB/MgO structures [88,127,136]. In contrast, the series (B) samples with the Ta dusting indicate $t_d \approx 0.8\text{nm}$ and a much larger $M_s = 1800\,\text{emu/cm}^3$. These results are comparable to some previous studies of annealed ($\sim 300\,^{\circ}C$) Ta/FeCoB/MgO samples where the dead layer [137] has been attributed to undesirable diffusion of Ta into the FeCoB, perhaps to the ferromagnet/oxide interface [138]. Therefore, we tentatively attribute the thick dead layer in series (B) samples to the intermixing of dusting layer and FeCoB during the deposition of the Ta that is absent in the Hf dusting case. To avoid this intermixing-induced dead layer may be one of the key factors to achieve robust PMA at the FeCoB/MgO interface.

Another property of using Hf dusting to enhance PMA is that it does not require high temperature post-fabrication annealing, while in Ta/FeCoB/MgO structures without the Hf dusting, the thin FM layer typically only exhibits a weak PMA in the as-deposited state [136,137,139]. We obtained robust PMA behavior in as-deposited structures with the HfO_2 dusting layer, as shown in Fig. 4.3(b) with the plot of the PMA energy density $K_{\text{eff}} \equiv \mu_0 H_a M_s / 2$ as a function of the effective thickness $t_{\text{FeCoB}}^{\text{eff}} = t_{\text{FeCoB}} - t_{\text{d}}$ of the FeCoB for the series (A) Ta/FeCoB(t_{FeCoB})/HfO_2(0.2)/MgO samples. The perpendicular magnetic anisotropy field H_a is determined from measurement of the anomalous Hall voltage response to an in-plane magnetic field [90,104] and I use the values of M_s determined from the VSM measurements discussed above. After rewriting Eq.(4.2) into $K_{\text{eff}} \bullet t_{\text{FeCoB}}^{\text{eff}} = (K_v - \frac{\mu_0}{2} M_s^2) \bullet t_{\text{FeCoB}}^{\text{eff}} + K_s$, I can use it to fit the linear part of the plot in Fig. 4.3(b), which gives the interfacial PMA

energy density $K_s = 1.74 \pm 0.09$ erg/cm^2. For Ta and Hf base layer systems without the Hf dusting, comparable anisotropies can be obtained only via high temperature ($\geq 200\ ^{\circ}C$) annealing [140,141]. In the inset of Fig. 2(b), I also show the effective PMA energy density K_{eff} for the series (B) samples with a 0.2 nm Ta dusting layer. Notice that here K_{eff} for Ta dusting is an order smaller than for the Hf dusting, which suggests that the PMA in the Ta dusting samples is much weaker than the Hf dusting samples. Note that the drop off in K_{eff} in the thin region of $t_{\text{FeCoB}}^{\text{eff}}$, as shown in Fig. 4.3(b), may be due to the magnetoelasticity effect in the thin film limit [136].

The different strength in the PMA for Hf dusting and Ta dusting samples can be also compared in the anomalous Hall measurement. For the HfO_2 passivated samples with strong H_a, their coercive field H_c is relatively high, typically $\geq$ 300 Oe, in comparison to quite low values (< 20 Oe) for the Ta dusting samples. Examples of the field switching that is obtained with an external field applied normal to the film surface are provided in Fig. 4.3(c) for a Ta(6)/FeCoB(1.1)/HfO_2(0.2)/MgO/Ta(1) and a Ta(6)/FeCoB(1.1)/TaO_x(0.2)/MgO/Ta(1) sample.

Our results above show that robust PMA can re archived in Hf dusting samples without high temperature annealing process, which may facilitate important applications as this could avoid complications such as material diffusion/intermixing during high temperature excursions. Previously, high temperature post-fabrication annealing treatment has been considered to be necessary to the realization of robust PMA in HM/FeCoB/MgO heterostructures. There are generally two important functions

of this annealing process: (i) removal of the over-oxidation of the FeCoB surface that occurs during MgO deposition [135,142] and (ii) promotion of the out-diffusion of the boron from the initially amorphous FeCoB [135,140] to obtain a more ordered, crystalline FeCo/MgO interface. The as-deposited Hf dusting results here indicate that the first function is the more important, or alternatively that the Fe-O-Hf hybridized bonds results in a stronger spin-splitting of the orbitals than do the Fe-O-Mg bonds.

On the other hand, since many applications of PMA heterostructures do require high temperature processing, both for integration with Si circuits and to attain a high TMR with MTJs, we also studied how different heat treatments affect the PMA of our Ta based HfO_2 structures. In Fig. 2(d) I show that after annealing at $210\ ^{\circ}C$ for 1 hour, H_a increases for every HfO_2 thickness studied, while the general dependence of H_a on t_{Hf} remains. However, after annealing at $300\ ^{\circ}C$ for 1 hour the PMA strength deteriorates, with a much weaker PMA retained only for $t_{\mathrm{Hf}} \geq 0.3\,\mathrm{nm}$. This deterioration may be again due to the diffusion of Ta from the base layer, since such diffusion has been known to damage the interfacial PMA in the Ta based PMA systems after high temperature annealing [138,139].

4.2.3 PMA enhancement due to Hf dusting in W based heterostructures

I also examined whether the Ta in-diffusion problem mentioned in the previous section can be avoided by the use of an alternative heavy metal base layer, such as W that can have a strong spin Hall effect.

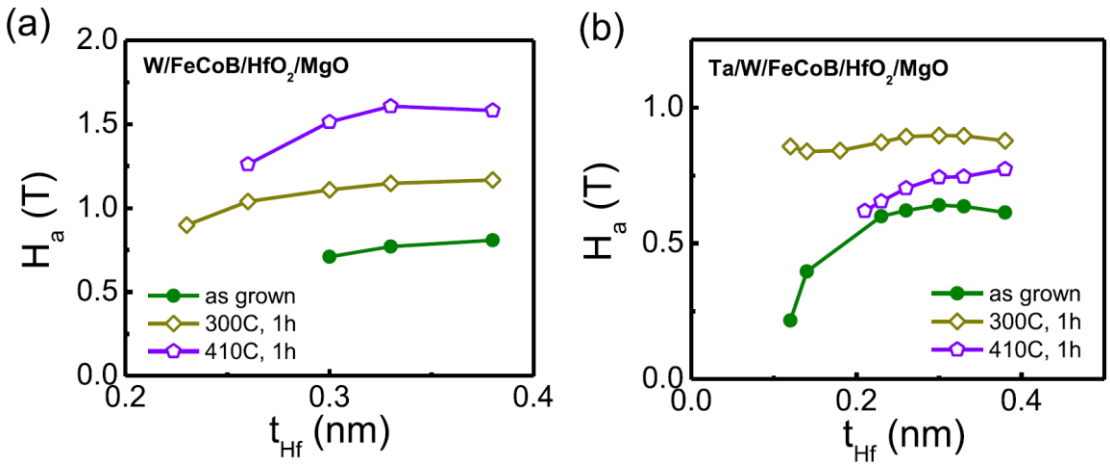

Figure 4.4: Enhanced PMA in W based heterostructure with Hf dusting. The perpendicular anisotropy fields of (a) beta-W(4)/FeCoB(0.8)/HfO_2(t_{Hf})/MgO/Ta and (b) Ta/alpha-W(4)/FeCoB(0.8)/HfO_2(t_{Hf})/MgO/Ta after different post-fabrication annealing treatments. Figures reproduced from Ou et al. [133].

Figure. 4.4(a) shows the values of H_a obtained from a set of W(4)/FeCoB(0.8)/HfO_2(t_{Hf})/MgO(1.6)/Ta samples as a function of t_{Hf} for the annealing treatment: as-deposited (no annealing), after 1 hour at 300 $^{\circ}C$, and after 1 hour at 410 $^{\circ}C$. I confirmed via resistivity measurements that the W here is in the high resistivity beta-W phase. As shown in Fig. 4.4(a), H_a increases with annealing temperature, and with 410 $^{\circ}C$ vacuum annealing we obtained H_a > 1.6 T for a sufficiently thick HfO_2 dusting layer. When we use a 1 nm Ta seeding layer before the deposition of the W layer, it results in the W being smoother and in it also being in the

lower resistivity alpha-phase. In Fig. 4.4(b), the relatively high H_a are obtained after $300\ ^{\circ}C$ annealing of such Ta(1)/W(4)/FeCoB(0.8)/HfO_2(t_{Hf})/MgO(1.6)/Ta samples for $t_{Hf} \geq 0.1$ nm, but annealing at $410\ ^{\circ}C$ degrades H_a, particularly for the heterostructures with thinner HfO_2, which is likely due to in-diffusion of Ta from the bottom seeding layer.

4.2.4 Hf dusting induced PMA in NiFe and MgO systems

So far most of the research on PMA in Fe alloy/MgO systems have been focused on the magnetic material of FeCoB, due to its important role in MTJs for the realization of a large TMR effect (see chapter 1). Alternatively, with our Hf dusting technique other magnetic Fe alloys with attractive properties, such as $Ni_{80}Fe_{20}$ (Py), could be of possible interest and value if samples of sufficiently strong anisotropy can be produced. A previous study with $Ni_{80}Fe_{20}$ has reported that when it is grown on an MgO underlayer, PMA can be achieved with proper capping materials,(i.e. with a MgO/$Ni_{80}Fe_{20}$/capping layer structure) [143], although the PMA strength was quite weak in that case. In order to demonstrate that the Hf dusting technique can indeed provide a range of opportunities in both PMA related material research and applications, I will show below that significant PMA can be achieved with a suitable combination of HfO_2 and $Ni_{80}Fe_{20}$, *e.g.* with Ta/ $Ni_{80}Fe_{20}$/HfO_2/MgO and with Ta/Hf(0.5)/$Ni_{80}Fe_{20}$/HfO_2/MgO multilayers.

In Fig. 4.5(a) we show anomalous Hall measurements as a function of an in-plane magnetic field for as-deposited Ta based NiFe(~1.5)/HfO_2(0.2)/MgO samples

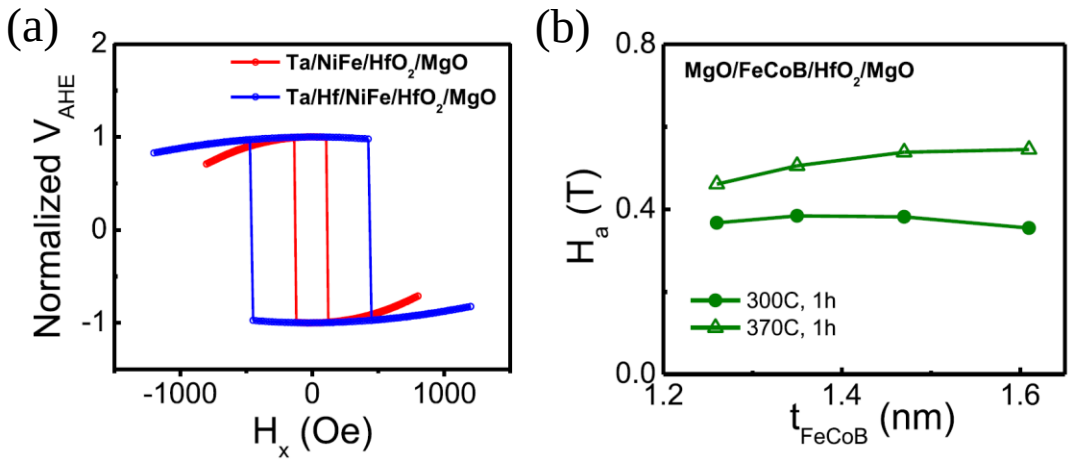

Figure 4.5: Hf dusting induced PMA in NiFe and MgO systems. (a) Anomalous Hall measurements of the as-grown samples Ta(6)/NiFe(1.4)/HfO_2(0.2)/MgO/Ta and Ta(6)/Hf(0.5)/NiFe(1.5)/HfO_2(0.2)/MgO/Ta as a function of in-plane magnetic field. (d) The Ha of MgO(1.6)/FeCoB(t_{FeCoB})/HfO_2(0.3)/MgO(0.8)/Ta samples after different post-fabrication annealing treatments. Figures reproduced from Ou et al. [133].

with and without the Hf spacer at the Ta/NiFe interface. The parabolic fit to the data indicates that H_a for the structure without Hf spacer was 1.1 kOe, while for the sample with the 0.5 nm Hf spacer, H_a is doubled to 2.1 kOe, larger than the previous results [143]. The stronger PMA in the NiFe sample with an amorphous 0.5 nm Hf spacer between the Ta base layer and the NiFe likely results from its role to accommodate the crystalline mismatch between the Ta and the NiFe. In particular, the coercive field of the Ta/Hf(0.5)/$Ni_{80}Fe_{20}$(1.5)/HfO_2/MgO is around 100 Oe (not shown here). We conclude that the combination of a HfO_2 passivation layer at the Fe alloy/oxide interface together with a thin Hf spacer layer between the HM and the Fe

alloy (when needed due to crystalline mismatch between the HM and the Fe alloy) can be a robust strategy for engineering the PMA of a range of thin-film magnetic heterostructures.

A recent development in MTJ technology for spin transfer torque applications is to include a second, thinner MgO layer on the other side of the FeCoB free layer to enhance its PMA strength [144,145]. In this kind of MgO/FeCoB/MgO sandwich structure, the enhanced K_{eff} of the free layer permits the use of a thicker layer with higher thermal stability, and also suppresses the magnetic damping enhancement that typically exists in a thin FM layer. To show that our Hf dusting technique can also be beneficial in this kind of structure, we examined the PMA modification of by depositing multilayer stacks of MgO(1.6)/FeCoB(t_{FeCoB})/HfO_2(0.2)/MgO(0.8)/Ta onto oxidized Si substrates. Unlike in the case of using heavy metals as the base layers, before annealing these samples do not exhibit PMA, which may be attributed to the deleterious effect of chemisorbed oxygen on the surface of the sputter deposited MgO after deposition [135] that overly oxidizes the lower surface of the subsequently deposited FeCoB. After annealing there is strong PMA. In Fig. 4.5 (b) I show a plot of H_a of such samples as a function of t_{FeCoB}. Quite strong anisotropy fields are obtained to high values of t_{FeCoB}, particularly for the samples annealed at $370\ ^{\circ}C$. Field modulated FMR studies of such a heterostructure with $t_{\text{FeCoB}} = 1.6$ nm yielded a magnetic damping parameter $\alpha = 0.009$, while a Ta/FeCoB(1.6)/MgO(1.6)/Ta sample showed $\alpha = 0.02$, consistent with earlier work [47,127]. Our results here thereby demonstrate that strong PMA and low magnetic damping can be realized simultaneously via the Hf dusting technique.

4.3 Interfacial engineering in NM/FM/MgO heterostructures using Zr ultrathin insertion layers

In the previous section, I introduced our results that an ultrathin Hf dusting layer between the Fe alloy and MgO layers can provide a robust PMA energy density with great high temperature thermal stability. Motivated by this, we are interested into the study about whether there are other materials that can have similar material properties, which can be used to enhance the PMA strength at the FM/MgO interface similar to the ultrathin Hf insertion. We are also interested in utilizing such material as a potential thin spacer between the NM and FM, which may remove the detrimental effects at that interface and hence improve the magnetic performance of a device consisting of the NM/FM/MgO heterostructure, as has been demonstrated in the PtMn research by inserting a thin Hf spacer there [104].

In order to provide a similar PMA enhancement as the Hf dusting, we anticipate that the new material should at least have similar heat of formation (also referred as the enthalpy of formation) during oxidation, which is the change of the enthalpy from the element (e.g Hf) into the corresponding substance (e.g. Hf dioxide). This is because in order to protect the FM from overoxidation from the subsequent deposition of MgO, the dusting material should have better heat of formation than the MgO so that it can form some kind of protecting oxide on top of the FM layer that may provide optimum oxidation level there to enhance the PMA energy density (see discussion in the previous sections). Zirconium (Zr) is an element in the same column as Hf in the periodic table but with lighter atomic mass. Previous reports indicate that Zr has a comparable heat of

formation in the form of oxide compared to Hf [146,147], indicating it may be a good candidate to enhance the PMA as well. Moreover, due to its lighter mass and potentially weaker spin-orbit interaction, Zr as a spacer may have even better performance than Hf. In the following sections, I will introduce our experimental study using Zr as both the dusting and spacer layer to improve the magnetic properties in the NM/FM/MgO heterostructures.

4.3.1 Sample growth and fabrications

Similar to our previous studies, the samples in this research were all prepared by DC sputtering (with RF magnetron sputtering for the MgO layer). The base pressure was below 6×10^{-8}Torr, with the sputtering condition of 2mTorr Ar pressure, 30 watts power. I sputtered a series NM(either Ta, W or Pt)/Zr/FeCoB(t_{FeCoB})/Zr/MgO heterostructures to test Zr both as a dusting layer between FeCoB and MgO and as a spacer between NM and FeCoB. I used a low deposition rate of Zr (<0.004 nm/s) to form the Zr dusting layer and spacer. On top of the FeCoB/Zr layers, the subsequent deposition of the MgO (with a growth rate of 0.005 nm/s at 100 watts power, 2 mTorr Ar) oxidized the Zr due to the higher heat of formation in Zr. A thin top Ta film was deposited on MgO for all samples as a protection layer. For the Pt base samples, 1nm Ta was also deposited beneath Pt to provide a smoother buffer layer for the growth of Pt. VSM measurements were performed to determine the effective FM thickness and magnetization. As for the device fabrications, the heterostructures were fabricated into $5\times60\,\mu m^2$ Hall bars for anomalous Hall measurements or $10\times20\,\mu m^2$ bars for ST-

FMR measurements. Standard photolithography steps including baking at 115 $^{\circ}C$ for 1 min twice were performed during the fabrication. After device fabrications, I annealed some of the samples to different temperatures in a vacuum furnace to compare with the as-deposited devices.

4.3.2 PMA enhancement due to Zr dusting in Ta based heterostructures

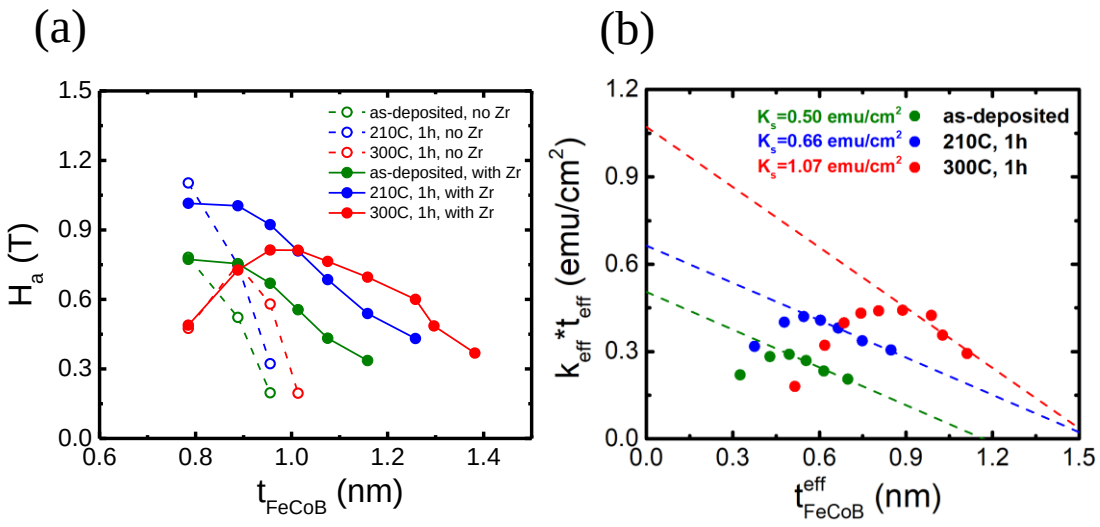

Figure 4.6: PMA measurements on the Ta based samples with and without Zr dusting. (a) The perpendicular anisotropy field Ha as a function of t_{FeCoB} for two sample Ta(6)/FeCoB(t_{FeCoB})/MgO (open dots) and Ta(6)/FeCoB(t_{FeCoB})/Zr(0.2)/MgO (solid dots) with different annealing treatments. (b) The effective anisotropy energy density K_{eff} determined from anomalous Hall measurements as a function of in-plane magnetic field for the as-deposited and annealed Ta(6)/FeCoB(t_{FeCoB})/Zr(0.2)/MgO.

I will first discuss the results from Ta based samples. Fig. 4.6(a) shows the magnetic perpendicular anisotropy field H_a, as determined from anomalous Hall measurements under in-plane field sweep, for two Ta based heterostructures Ta(6)/FeCoB(t_{FeCoB})/MgO (open dots) and Ta(6)/FeCoB(t_{FeCoB})/Zr(0.2)/MgO (solid dots) in the as-deposited state and after different annealing treatments. In all cases, H_a in the samples with 0.2nm Zr dusting layer is larger than those without any Zr dusting, indicating the interfacial PMA is enhanced with the ultrathin Zr dusting. More specifically, the Zr dusting appears to enlarge the FeCoB thickness range that shows PMA. In the Ta(6)/FeCoB(t_{FeCoB})/MgO sample, the PMA is measurable when $0.8\,\text{nm} < t_{\text{FeCoB}} < 1\,\text{nm}$, while in the Ta(6)/FeCoB(t_{FeCoB})/Zr(0.2)/MgO, that range is enhanced to $0.8\,\text{nm} < t_{\text{FeCoB}} < 1.4\text{nm}$. Within the same sample set, H_a is increased upon annealing, which may be due to a better passivation at the FeCoB/Zr oxide interface or improved FeCoB crystalline interface beneficial from the out-diffusion of boron after heat treatments [140].

To further characterize the PMA enhancement in the Zr dusting samples, I calculated the effective anisotropy energy density K_{eff} from the determined H_a and magnetization M_s in the Ta(6)/FeCoB(t_{FeCoB})/Zr(0.2)/MgO samples as a function of the effective FeCoB thickness, and the results plot in Fig. 4.6(b). With the same equation used previously, $K_{\text{eff}} \bullet t_{\text{FeCoB}}^{\text{eff}} = (K_v - \frac{\mu_0}{2} M_s^2) \bullet t_{\text{FeCoB}}^{\text{eff}} + K_s$, the linear fits in Fig. 4.6(b) give the interfacial PMA energy density $K_s = 0.50\ \text{erg/cm}^2$ (as-deposited),

$K_s = 0.66\ \text{erg/cm}^2$ (after annealing at $210\ ^\circ C$ for 1 h) and $K_s = 1.07\ \text{erg/cm}^2$ (after annealing at $300\ ^\circ C$ for 1 h) respectively.

4.3.3 PMA enhancement due to Zr dusting in W based heterostructures

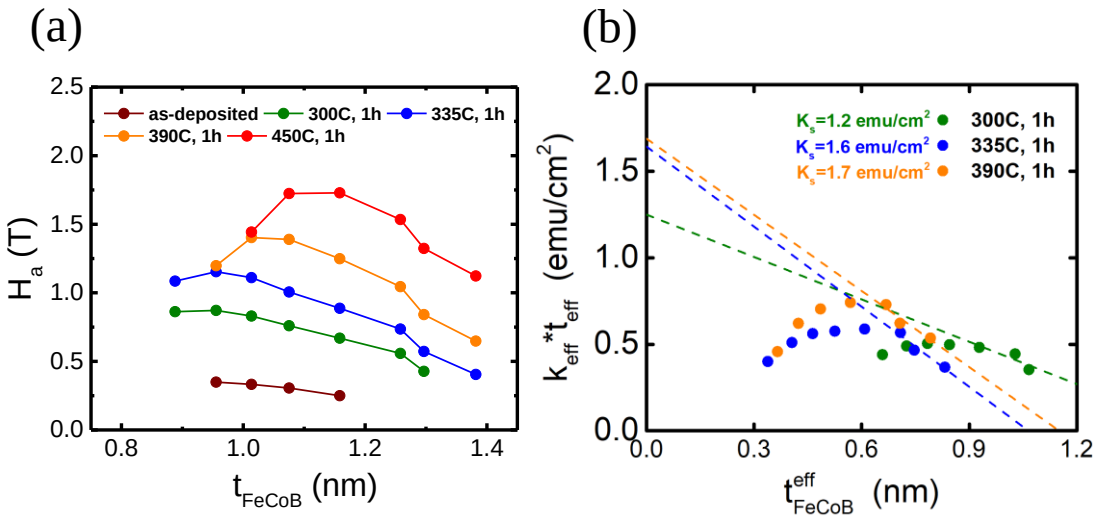

Figure 4.7: PMA measurements on the W based samples with and without Zr dusting. (a) The perpendicular anisotropy field Ha as a function of t_{FeCoB} for the sample W(4)/FeCoB(t_{FeCoB})/Zr(0.2)/MgO with different annealing treatments. (b) The effective anisotropy energy density K_{eff} determined from anomalous Hall measurements as a function of in-plane magnetic field for the as-deposited and annealed W(4)/FeCoB(t_{FeCoB})/Zr(0.2)/MgO.

In addition to the Ta based samples, we also tested the enhancement of PMA with the Zr dusting in beta-W based heterostructures. Figure 4.7(a) shows H_a as a function of t_{FeCoB} in the as grown sample W(4)/FeCoB(t_{FeCoB})/Zr(0.2)/MgO and in those after annealing at and above $300\ ^\circ C$. The perpendicular anisotropy field is enhanced for

all annealing temperatures and it is still robust after annealing at 450 $^{\circ}C$ for 1h. Remarkably, H_a is able to reach 1 Tesla upon annealing above 300 $^{\circ}C$ and is even larger with the 450 $^{\circ}C$ annealing reaching about 1.7 Testa. On the other hand, in the thin t_{FeCoB} region, the onset thickness for the downturn of H_a shifts to thicker range as the annealing temperature increases, which may be due to the changing in the crystalline structure of the FeCoB.

To better quantify the PMA strength in these Zr dusting samples, I again evaluated the effective anisotropy energy density K_{eff} after various annealing treatments in the same samples W(4)/FeCoB(t_{FeCoB})/Zr(0.2)/MgO as a function of the effective t_{FeCoB}, as plotted in Fig. 4.7(b). From the linear fits, I can estimate the interfacial PMA energy density $K_s = 1.2$ erg/cm^2 (after annealing at 300 $^{\circ}C$ for 1 h), $K_s = 1.6$ erg/cm^2 (after annealing at 335 $^{\circ}C$ for 1 h) and $K_s = 1.7$ erg/cm^2 (after annealing at 390 $^{\circ}C$ for 1 h) respectively. Even after high temperature 390 $^{\circ}C$ annealing, the Zr dusting W base sample still persists in having robust PMA. This result confirms the good thermal stability of the ultrathin Zr dusting layer and it suggests that the Zr dusting, in addition to Hf dusting, might provide opportunities to efficiently engineer the anisotropy in thin film magnetic devices for spintronics applications.

4.3.4 The spin diffusion length in Zr

The above results focus on how the an ultrathin Zr insertion layer between FeCoB and MgO can effectively enhance the PMA energy density at that interface. A thin Zr layer can also serve as a spacer between the NM (spin current source) and the FM to eliminate some interfacial effects that may be detrimental to the spin transfer process. The spin diffusion length of Zr also needs to be determined in such a NM/Zr/FM heterostructure to optimize the best Zr thickness without sacrificing too much spin current. For this reason, I fabricated a series of in-plane magnetized samples W(4)/Zr(t_{Zr})/FeCoB(t_{FeCoB})/MgO with a Zr spacer ($0.25\,\text{nm} \le t_{\text{Zr}} \le 2\,\text{nm}$) and $2\,\text{nm} \le t_{\text{FeCoB}} \le 7\,\text{nm}$. I measured the SOT of these samples via ST-FMR. For a given Zr spacer thickness, we determined the FMR spin torque efficiency ξ_{FM} (Eq. 2.22) as a function of t_{FeCoB} and extrapolated the DL torque efficiency ξ_{DL} from the relation $1/\xi_{FM}$ v.s. $1/t_{\text{FeCoB}}$ (Eq. 2.23), during which we also considered the current shunting effect from the Zr spacer to the estimation of ξ_{DL}. Fig. 4.8 plots ξ_{DL} as a function of t_{Zr}. After considering the spin diffusion model, $\xi_{DL}(t_{\text{Zr}})$ can be expressed as:

$$\xi_{DL}(t_{\text{Zr}}) = \xi_{DL}(0) \cdot \frac{K_{(\text{Zr,W})}}{e^{t_{\text{Zr}}/\lambda_{\text{Zr}}} + P_{(\text{Zr,W})} e^{-t_{\text{Zr}}/\lambda_{\text{Zr}}}} \tag{4.3}$$

where $K_{(\text{Zr,W})}$ and $P_{(\text{Zr,W})}$ are two material parameters related to the interfacial spin mixing conductance $G^{\uparrow\downarrow}$ and the spin conductance, G_W, of W (see the supplementary material of Ref. [88] for derivation). With Eq. (4.3), I fit the data in Fig. 4.8 and estimate the spin diffusion length of Zr to be $\lambda_{\text{Zr}} = 1.3\,\text{nm}$. This value is larger than that of Hf

($\lambda_{\mathrm{Hf}} = 0.9\,\mathrm{nm}$) determined from a very similar heterostructure measurement. The longer spin diffusion length may be due to its weaker spin-orbit interaction compared to the heavier element Hf. We also determined the resistivity of the thin Zr layers as $\rho_{\mathrm{Zr}} \simeq 217\,\mu\Omega\bullet\mathrm{cm}$. With λ_{Zr} and ρ_{Zr}, I can estimate the spin conductance of Zr to be $G_{\mathrm{Zr}} \equiv 1/\left(\lambda_{\mathrm{Zr}}\rho_{\mathrm{Zr}}\right) \simeq 3.54\times10^{14}\ \Omega^{-1}\mathrm{m}^{-2}$. The relatively long spin diffusion length of Zr may be beneficial for the spin transport across the Zr spacer.

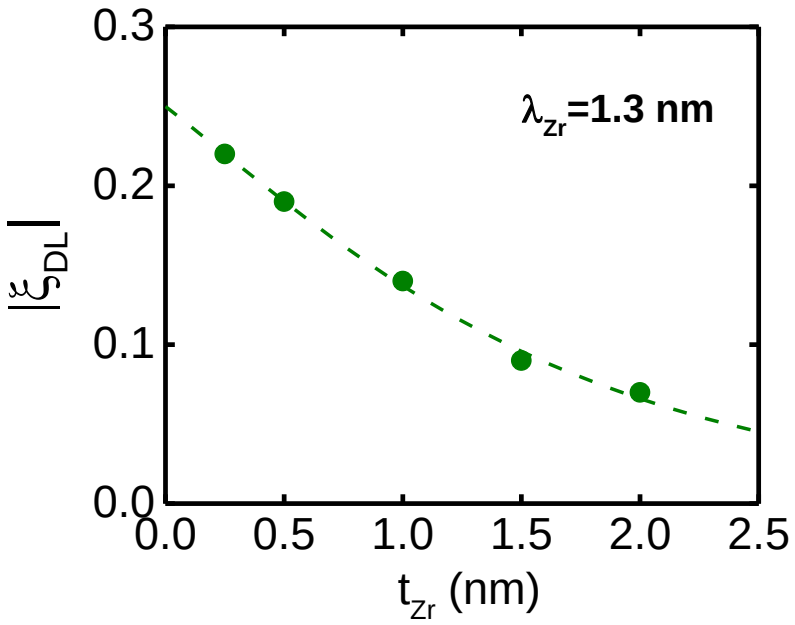

Figure 4.8: Determination of the Spin diffusion length Zr. The dashed line is the fit using Eq. (4.3).

4.3.5 Lowing the enhanced magnetic damping using Zr spacer in Pt base systems

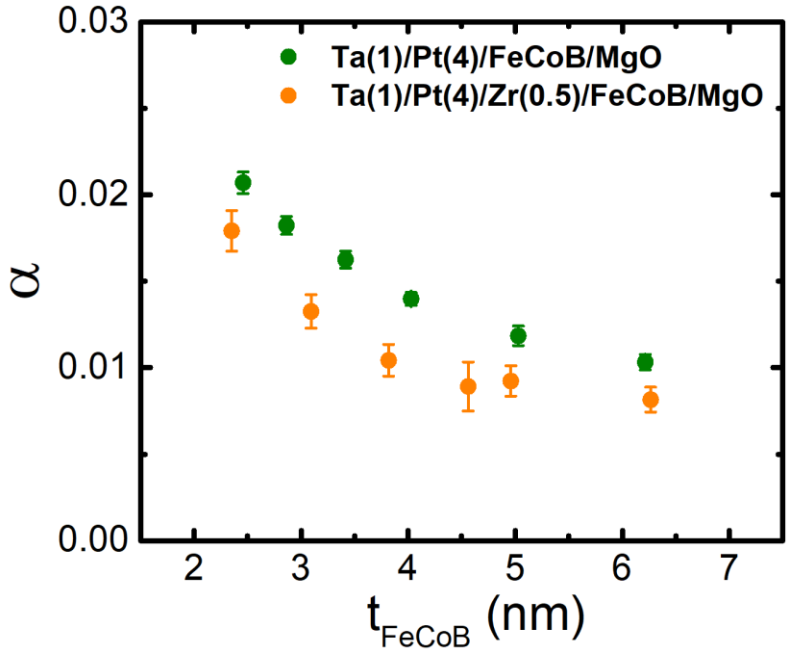

Figure 4.9: Magnetic damping measurements of Pt base heterostructure using Zr spacer.

Finally, in order to demonstrate that an ultrathin Zr between the NM and FM can reduce the interfacial effects that may be detrimental to the spin transfer process such as the SML that can increase the magnetic damping, I prepared two sets of samples Ta(1)/Pt(4)/FeCoB(t_{FeCoB})/MgO and Ta(1)/Pt(4)/Zr(0.5)/FeCoB(t_{FeCoB})/MgO and measured their damping via ST-FMR, with the results shown in Fig. 4.9. Compared to the Pt/FeCoB structure without Zr, the 0.5 nm Zr spacer can reduce the magnetic damping as can be clearly seen in Fig 4.9. This feature of using Zr as a spacer, together with the PMA enhancement with Zr dusting, may provide a pathway to design more efficient and low current consumption spintronics devices [148] (also see chapter 5).

CHAPTER 5

ENHANCED PERFORMANCE OF THREE-TERMINAL MAGNETIC TUNNEL JUNCTIONS VIA INTERFACIAL MODIFICATION

5.1 Introduction

As introduced in chapter 1, the magnetic tunnel junction (MTJ) is the basic building element for magnetic signal reading in a nonvolatile magnetoresistive memory device due to its large TMR effect. In an MTJ structure, it generally includes a direction fixed magnetic layer (referred as the fixed layer) and another layer (referred as the free layer) of which the magnetization direction can be switched bipolarly. Instead of using a magnetic field to switch the magnetization in the free layer, a much more efficient and realistic way is to exploit the spin torques to realize the magnetization switching. Based on the origins of the spin torques, the MTJ scheme can be generally categorized into two types. One type is the spin-transfer-torque MTJ (STT-MTJ) [1], which uses the STT via the spin filter effects to switch the free layer in a two-terminal structure (see Fig. 5.1(a) for the schematic). In STT-MTJ, the write and read current paths are collinear. Alternatively, the write current path can be separated from the read one in the so-called three-terminal MTJ structure [149], which is shown in Fig. 5.1(b). In this type of the MTJ, the manipulation of the free layer is implemented through the spin-orbit torque generated from the transversely diffusive spin current, which typically results from SHE. This type of MTJ is usally referred as the spin-orbit-torque MTJ (SOT-MTJ).

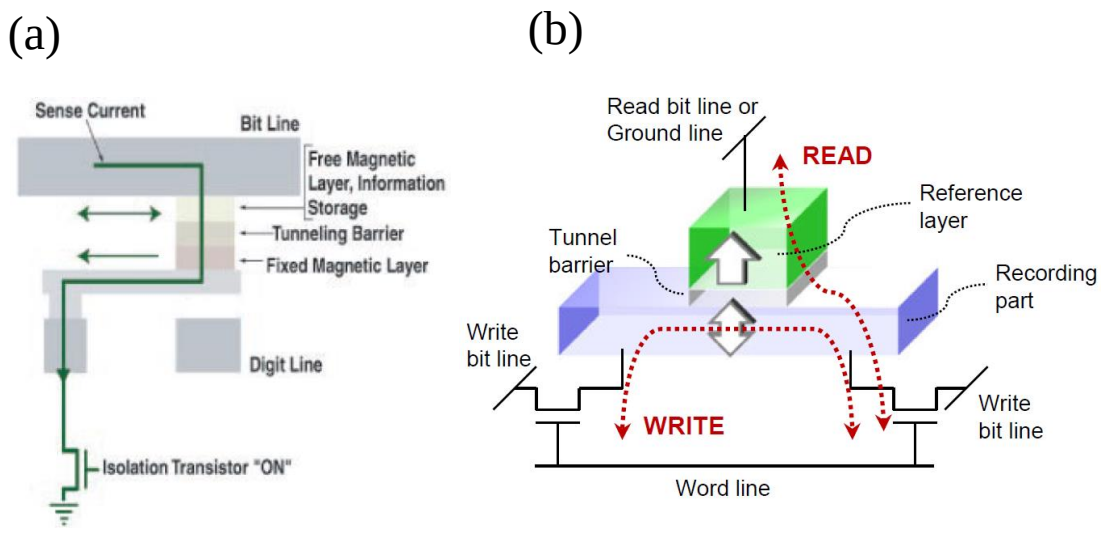

Figure 5.1: Schematics for (a) a two-terminal MTJ and (b) a three-terminal MTJ. Figures reproduced from Wolf et al. [1] and Fukami and Ohno [149].

Compared to the two-terminal MTJ, the separation of the write and read channel in the three-terminal MTJ geometry provide several advantages, such as the implementation of a high-speed reliable read-out without a read disturbance and lower write energy [149], making it a promising candidate for nonvolatile magnetoresistive random access memory (MRAM). However, in order to be competitive with the other working memories such as static random access memory (SRAM), in addition to its nonvolatile nature, it will also require new mechanisms to improve the efficiency for switching nanoscale three-terminal MTJs, while also controlling the magnetic dynamics to achieve faster, nanosecond scale performance with low write error rates. In the following sections, I will show our study to improve the performance of the in-plane magnetized three-terminal MTJs by the modification of the free layer interfaces to

engineer the magnetic properties such as the interfacial magnetic anisotropy energy and enhanced magnetic damping, using the techniques I introduced in the previous chapters. We demonstrated in these three-terminal MTJs a switching current density lower than any other reported SOT magnetic memory devices at room temperature, and the high reliability in the fast magnetization switching [148].

5.2 Fast and low current SOT switching in in-plane magnetized MTJs via interfacial modification using Hf ultrathin insertion layers

5.2.1 Sample fabrications

All the samples in this work were prepared via DC magnetron sputtering in our sputtering system with a low deposition rate (<0.1nm/s) and a low base pressure ($\sim 10^{-8}$ Torr). The heterostructures were deposited on the high-resistive Si/SiO_2 wafers, $W/Hf(t_{Hf})/Fe_{60}Co_{20}B_{20}(1.8)/Hf(t_{Hf})/MgO(1.6)/Fe_{60}Co_{20}B_{20}(4)/Ta(5)/Ru(5)$ (thickness in nanometers) with t_{Hf} <0.3nm. We used beta-W because of its large spin Hall ratio [76] that can be beneficial in the magnetization switching with low switching current density (see Eq. 5.1). The role of ultrathin Hf insertion layers at the W/FeCoB and FeCoB/MgO interface will be discussed below in the next section.

The samples were then fabricated into three-terminal MTJ devices in three steps. First the spin Hall channels (nominal sizes 500nm) were defined using deep UV lithography and ion beam etching, of which the actual width of the channel was

determined via the atomic force magnetometry (AFM). Second, the MTJ nano pillars were defined via e-beam lithography and ion beam etching. The pillar size was designed to have variation ranging from $190\,\text{nm}\times 30\,\text{nm}$ to $390\,\text{nm}\times 100\,\text{nm}$. Large, μm size pillars were also exposed simultaneously and serve as vertical contact between top leads and bottom channels. Lastly, a blanket nitride (~80nm Si_3N_4) was deposited on the wafer to protect the MTJ pillars, which was followed by the deposition of Ti/Pt contacts (10nm/50nm) to the two ends of the W channel and to the top electrode of the MTJ. The schematic and a SEM image of the MTJ channel and pillar are shown in Fig. 5.2. After fabrication, the devices were annealed in an air furnace at various temperatures.

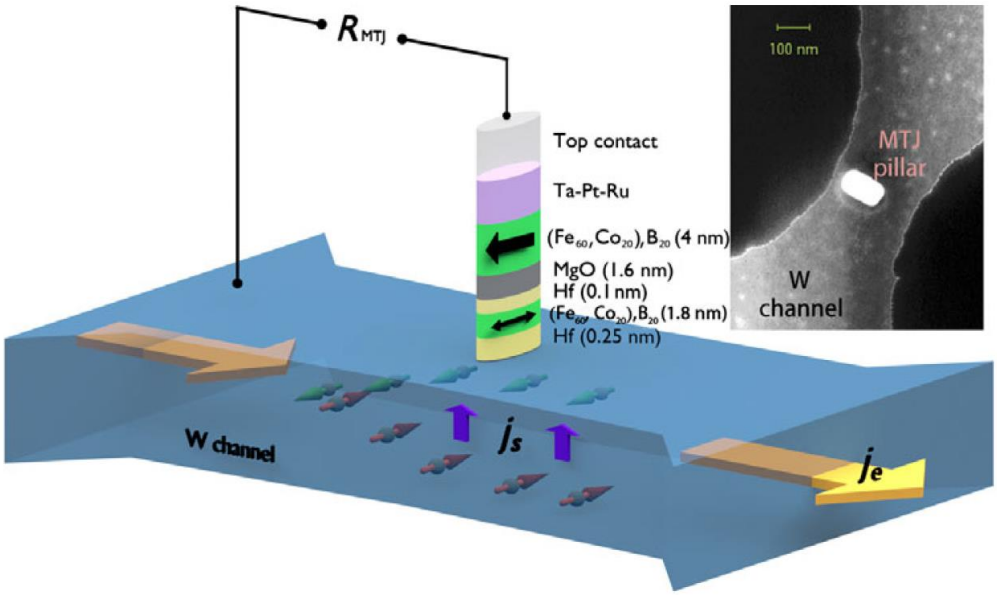

Figure 5.2: An MTJ schematic with ultrathin Hf insertion layers. Inset: SEM image shows a representative nanopillar situated on a W channel after e-beam exposure, development and ion beam etching. Figure reproduced from Shi et al. [148].

5.2.2 Enhanced magnetic properties with ultrathin Hf insertion layers at interfaces

As mentioned earlier, we used beta-W as the spin Hall channel that provides the spin current in our MTJ devices due to the large spin Hall ratio in beta-W. On the other hand, ultrathin Hf insertion layers were also inserted respectively between the free layer and the MgO and between the W and the free layer. As discussed in chapter 4, the thin Hf dusting layer at the FM/MgO interface enhances the PMA energy density there. As a result, for an in-plane magnetized FM layer, its demagnetization field (or effective magnetization) M_{eff} is reduced due to the enhanced interfacial perpendicular magnetic anisotropy energy density at that interface. The thin Hf spacer between W and FeCoB was designed to lower the magnetic damping as will be shown below.

To show that the Hf dusting layer can indeed lower the M_{eff} in our MTJ devices, we performed the flip-chip FMR measurements on two control samples, one with only the Hf dusting (0.1nm), W(4)/FeCoB(1.8)/Hf(0.1)/MgO(1.6)/FeCoB(4)/Ta(5)/Ru(5), and one without any Hf insertion W(4)/FeCoB(1.8)/MgO(1.6)/FeCoB(4)/Ta(5)Ru(5). For both the as grown and annealed cases, the M_{eff} in the samples with Hf dusting is obviously smaller than the samples without the Hf dusting, as shown in Fig. 5.3(a). Specifically, after annealing at 240°C for 1h, M_{eff} for the Hf dusting-only structure was reduced to 4300 Oe, compared to 9860 Oe for the W MTJ system without Hf. Interesting, by inserting another thin Hf spacer (0.25 nm) between W and FeCoB can further reduce M_{eff} to 2110 Oe after annealing at 240°C, which may be attributed to some of that Hf

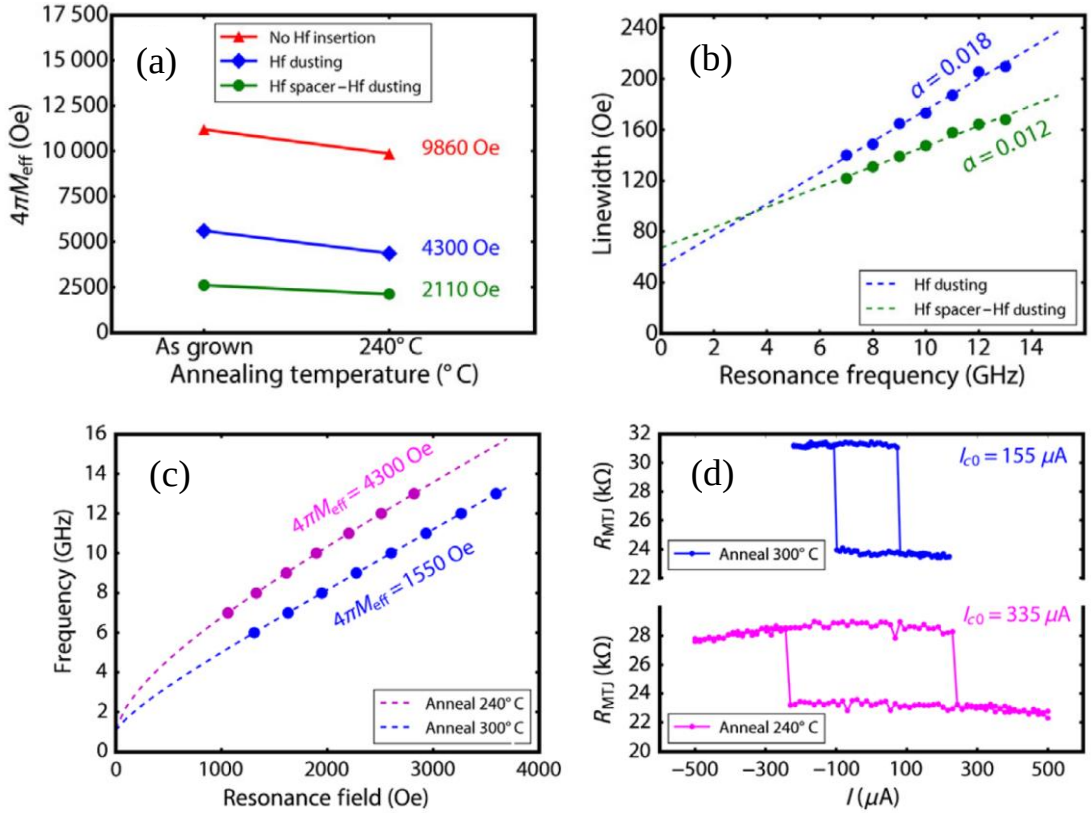

Figure 5.3: Enhanced magnetic performance via ultrathin Hf insertion. (a) M_{eff} measurements via flip-chip FMR for as grown and annealed samples with and without Hf insertion. (b) Linewidths at different resonance frequencies (applied fields) for the Hf dusting-only sample and the Hf spacer-Hf dusting sample measured by flip-chip FMR. Both samples are annealed at 240 °C. (c) Flip-chip FMR measurement on two Hf dusting-only samples, annealed at 240 °C (magenta) and 300 °C (blue) respectively. (d) Current-induced switching of Hf dusting-only samples annealed at two different temperatures, 240 °C (magenta) and 300 °C (blue). The spin torque switching loops indicate a substantial reduction in critical current with the higher temperature anneal as quantified by the results of ramp rate measurements of I_{c0}. Figure reproduced from Shi et al. [148].

diffusing through the FeCoB to the MgO interface during the anneal [92,150]. These results clearly show that the an ultrathin Hf dusting layer can efficiently reduce M_{eff} of the free layer in the MTJ heterostructure.

Meanwhile the insertion of the Hf spacer between the W and FeCoB not only helps to reduce M_{eff}, but also suppresses the enhanced magnetic damping as shown in Fig. 5.3(b) determined from the FMR measurements. As can be seen there, the magnetic damping α decreases substantially from 0.018 to 0.012, which may be attributed to a passivation of the W surface that suppresses reaction between the W and FeCoB that would otherwise result in interfacial spin memory loss [73].

This reduction in damping without sacrificing too much spin current by using an ultrathin Hf spacer, together with the lowing M_{eff} via Hf dusting, are beneficial for MTJ current-induced switching. For three terminal-MTJs, the SOT switching current density within the macrospin model, is predicted to vary as [40,151]:

$$J_{c0} = I_{c0} / w_{SH} t_{SH} = \frac{2e}{\hbar} \mu_0 M_s t_{FM} \alpha (H_c + M_{eff} / 2) / \xi_{DL} \tag{5.1}$$

where e is the electron charge, $\hbar$ is the reduced Plank constant, μ_0 is the permeability of free space, M_s is the saturation magnetization of the free layer and t_{FM} is the free layer's effective magnetic thickness, which were measured to be 1.2×10^6 A/m and 1.7 nm. As can be seen from Eq. (5.1), for a given FM thickness, the smaller the magnetic damping and M_{eff} are, the lower the switching current density J_{c0} is. Therefore, our

results above indicate that an ultrathin Hf dusting and spacer in the MTJ structure should improve its performance by reducing J_{c0} in current-induced magnetization switching.

To further demonstrate that annealing at higher temperatures for our MTJ devices can be beneficial, since it is usually required in the integration process of MRAM with CMOS, we annealed our samples at temperatures at 240°C and 300°C and determined their current switching performance. Figure 5.3(c) shows the M_{eff} of the free layer in a MTJ structure with 0.1 nm Hf dusting layer (no Hf spacer) after annealing at 240 °C and 300 °C for 1 hour respectively. There M_{eff} is reduced from 4300 Oe to 1550 Oe, a compelling demonstration of the effectiveness of Hf dusting in enhancing the interfacial PMA energy after high temperature annealing treatments [133]. To examine the SOT switching behavior of devices with such low M_{eff} we patterned MTJs with pillar size $390\,\text{nm}\times 100\,\text{nm}$ and annealed two of them at the two different temperatures, 240 °C and 300 °C. Consistent with the reduction in M_{eff}, we observed clean SOT switching with a much lower critical current (after performing the ramp rate experiments, see next section), I_{c0} = 155 μA, after 300 °C annealing temperature in comparison to the 240 °C critical current I_{c0} = 335 μA. These results can be easily understood with Eq. (5.1), since a smaller M_{eff} results in a lower I_{c0} if other material parameters are unchanged.

5.2.3 Low-current SOT switching of the MTJ with ultrathin Hf insertion

As discussed above, inserting an ultrathin Hf layer between FeCoB and MgO, and between W and FeCoB, can efficiently reduce the demagnetization field and magnetic damping in the heterostructures. With these techniques, in order to demonstrate that we can indeed realize low-current SOT switching in an MTJ device, we prepared a sample with the thin film multilayer stack with the Hf insertion, W(4.4)/Hf(0.25)/$Fe_{60}Co_{20}B_{20}$(1.8)/Hf(0.1)/MgO(1.6)/$Fe_{60}Co_{20}B_{20}$(4)/Ta(5)/Ru(5) (S), and fabricated it into a three-terminal MTJ with a nanopillar ($190\,\text{nm}\times 30\,\text{nm}$) on a 480 nm wide W channel. The device was annealed at 240 °C for 1 hour to improve the TMR of the MTJ and further promote the Hf-dusting-induced PMA strength as discussed in the previous section.

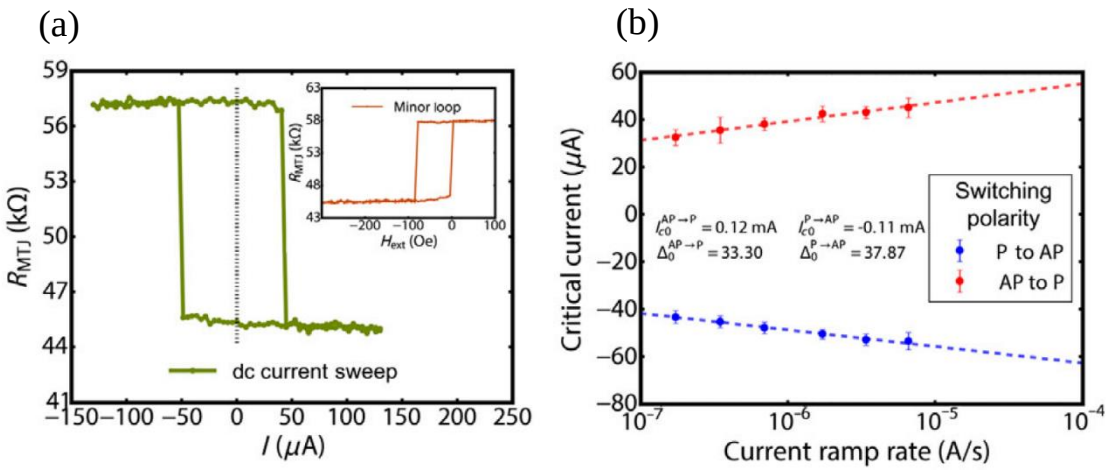

Figure 5.4: Current switching experiments on an MTJ with both Hf dusting and spacer layer. (a) Current induced switching loop of the free layer of the MTJ device (S) showing a thermally assisted switching current of 50 μA. (b) Current ramp rate measurement on the device (S). Dashed lines are linear fits to the macrospin model giving an average zero-thermal fluctuation critical current of 115 μA with a thermal stability factor of 35.6. Figure reproduced from Shi et al. [148].

The minor magnetic loop response of the MTJ resistance for the device (S) is shown in the inset of Fig. 5.4(a), where an in-plane magnetic field H_{ext} is scanned along the long axis of the MTJ device within range of ± 300 Oe. As can be seen there, the field range is large enough to reverse the orientation of the thin bottom free layer of the MTJ from being parallel (P) to anti-parallel (AP) to the thicker FeCoB reference layer as read out from the TMR effect, but small enough to maintain the orientation of the reference layer due to its relatively stronger shape anisotropy. Notice that the horizontal offset of the minor loop (~ −50 Oe) is due to the dipole field from the reference layer on the other side of the MgO barrier felt by the free layer. We canceled this offset field by applying an appropriate H_{ext} in all the SOT measurements discussed in the following.

In the main part of Fig. 5.4(a) I show the characteristic direct current (DC) SOT hysteretic switching behavior of the MTJ device (S) with the bias current in the W channel ramped quasi-statically. Notice that the switching polarity is consistent with the negative spin Hall sign of β-W in comparison to that of platinum [76,152]. In this kind of DC SOT switching experiments, the magnetization reversal attempts are typically assisted by thermal fluctuation for nanoscale MTJ structures during slow current ramps. Therefore, it is important to evaluate the switching current without the thermal assistance in order to determine the SOT contribution. Within the macrospin or rigid monodomain model, the critical current I_c that is observed is dependent on the current ramp rate [153],

$$I_c = I_{c0}\left\{1-\frac{1}{\Delta}\ln\left[\frac{1}{t_0\Delta}\left(\frac{|I_{c0}|}{|\dot{I}|}\right)\right]\right\} \tag{5.2}$$

where I_{c0} is the critical current in the absence of thermal fluctuation, $\dot{I}$ is current ramp rate, Δ is the thermal stability factor that represents the normalized magnetic energy barrier for reversal between the P and AP states, and τ_0 is the thermal attempt time which is usually assumed to be 1 ns. In order to characterize the SOT contribution (I_{c0}) of this device, we measured the mean switching current $\dot{I}$ for varying from 10^{-7}A/s to 10^{-5}A/s, as shown in Fig. 5.4(b). With Eq. (5.2), an averaged zero-fluctuation switching current of $|I_{c0}|$ = 115 μA and $\Delta = 35.6$ were attained from the nearly symmetric SOT switching results. With the W channel width W_{SH} = 480 nm and thickness t_{SH} = 4.4 nm, this current ($|I_{c0}|$) corresponds to a switching current density $J_{c0} = 5.4 \times 10^6$ A/cm^2, more than three times lower than reported originally for a W-based three-terminal -MTJ without the Hf insertion [76] and by far the lowest yet reported for any three-terminal MTJ device with $\Delta > 35$ [148]. This result again highlights the effective role of the ultrathin Hf insertion technique to substantially improve the MTJ performance.

5.2.4 Pulse and write error rate measurements

We demonstrated above the realization of low-current SOT switching in the DC case in the MTJ device. Another critical question is whether fast and reliable switching can be implemented with low amplitude current pulses in these W-based MTJ devices with the Hf insertion, which is required for the application in high-speed cache memory. In order to characterize the short pulse performance of the MTJ device (S), the switching phase diagrams for the two cases, $P \rightarrow AP$ and $AP \rightarrow P$, were measured separately

using a fast pulse measurement method [148], with results shown in Fig. 5.5(a) and 5.5(b).

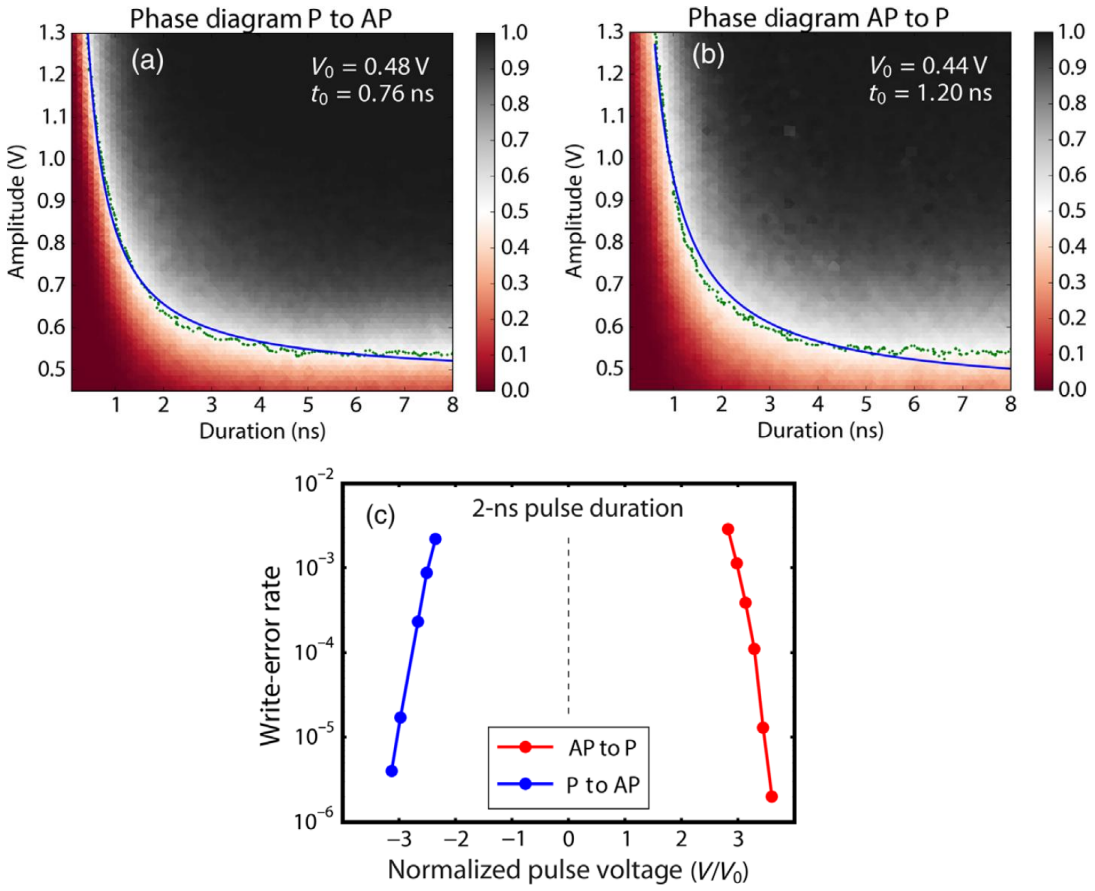

Figure 5.5: Fast and reliable pulse switching of a Hf spacer-Hf dusting MTJ device. Pulse switching phase diagrams and macrospin fits for polarities $P \rightarrow AP$ (a) and $AP \rightarrow P$ (b) respectively with the switching probability scale bar on the right. Each point is a result of 10^3 switching attempts. A characteristic switching time of ~1 ns and a critical voltage of 0.46 V are obtained after fitting 50% probability points (green points) to the macrospin model (blue curve). (c) WER measurement results for 2 ns square pulses applied to the device (a) and (b). Each point is a result of 10^6 switching attempts. Figure reproduced from Shi et al. [148].

Each data point in the switching phase diagram is the statistical result of 1000 switching attempts, and after each set of switching attempts, the switching probability was recorded accordingly, which depends on both the pulse amplitude and duration time. We can evaluate the pulse response of the MTJ by fitting the 50% switching probability boundary between the switching and non-switching regions via the macrospin model [154] as an approximation:

$$V = V_0(1 + \frac{\tau_0}{t}) \tag{5.3}$$

where τ_0 is the characteristic switching time and V_0 is the critical switching voltage. The fits with Eq. (5.3) in Fig. 5.5(a) and 5.5(b) give τ_0 and V_0 to be 0.76 ns and 0.48 V for $P \rightarrow AP$ and 1.20 ns and 0.44 V for $AP \rightarrow P$ respectively. With the channel resistance $R \approx 3.6$ kΩ, the critical switching voltage V_0 corresponds to a short pulse critical switching current (current density) $I_{c0} \approx 120$ μA ($J_{c0} \approx 5.9 \times 10^6$ A/cm^2), which is consistent with the ramp rate results shown in the previous section.

In addition to fast pulse switching, we also examined the reliability of the pulse switching by determining the MTJ's write error rate (WER) that is calculated based on the switching probability P_{switch}, WER = 1 − $P_{switch.}$ In Fig. 5.5(c), it shows the WER results measured with 2 ns pulses on the MTJ device (S), where square switching pulses of increasing voltages to the W channel were applied. For every voltage level we repeated the switching attempts 10^6 times and record P_{switch}, and then calculated WER accordingly. At 2 ns, WER of close to 10^{-6} is achieved for both polarities $P \rightarrow AP$ and $AP \rightarrow P$, which indicates the high reliability in our MTJ structures.

We notice that the observed anti-damping SOT reversal on $\tau_0 \leq 1$ ns timescale is much faster than predicted by the rigid domain, macrospin model. Previous studies in Pt-based MTJs indicate that the in-plane Oersted field H_{Oe} generated by the pulsed current is advantageous in promoting the fast reliable switching because it opposes the anisotropy field H_c of the free layer at the beginning of the reversal [152,155]. In our W-based MTJ devices, due to the opposite sign of the SHE in W, the generated H_{Oe} from the pulse is parallel to H_c at the beginning of the pulse which micromagnetic modeling indicated should be disadvantageous for very fast reversal [152]. In order to determine if there is another effective field, despite the Oersted field, appearing in our sample during SOT switching, we fabricated a W(4)/Hf(0.25)/FeCoB(t_{FeCoB})/Hf(0.1)/MgO/Ta sample (annealed at 240 °C for 1 hour) and determined its SOTs via ST-FMR measurements [73]. The damping-like and the field-like spin-orbit torque efficiencies, ξ_{DL} and ξ_{FL}, of this heterostructure were obtained as $\xi_{DL} = -0.20 \pm 0.03$ and $\xi_{FL} = -0.0364 \pm 0.005$ [148]. This field-like spin torque efficiency ξ_{FL} corresponds to an effective field $-6.68 \times 10^{-11}\,\mathrm{Oe}/(\mathrm{A}/\mathrm{m}^2)$ in the MTJ structure with a 1.8 nm free layer that is oriented in opposition to the Oersted field generated by the electric current, as previously reported for W devices [76], and approximately three times larger. Based on these results, the net transverse field in our W-based MTJ is thereby in opposition to the free layer's in-plane anisotropy field at the beginning of the reversal and hence may be playing an important role in the fast and reliable pulse switching results discussed here.

References

[1] S. A. Wolf, D. D. Awschalom, R. A. Buhrman, J. M. Daughton, S. von Molnar, M. L. Roukes, A. Y. Chtchelkanova, and D. M. Treger, Science **294**, 1488 (2001).

[2] I. Zutic, J. Fabian, and S. Das Sarma, Rev. Mod. Phys. **76**, 323 (2004).

[3] G. Lampel, Phys. Rev. Lett. **20**, 491 (1968).

[4] M. D. Stiles and J. Miltat, *Spin-Transfer Torque and Dynamics. In: Hillebrands B., Thiaville A. (Eds) Spin Dynamics in Confined Magnetic Structures III. Topics in Applied Physics*, vol 101 (Springer, Berlin, Heidelberg, 2006).

[5] D. C. Ralph and M. D. Stiles, J. Magn. Magn. Mater. **320**, 1190 (2008).

[6] M. Johnson and R. H. Silsbee, Phys. Rev. Lett. **55**, 1790 (1985).

[7] J. S. Moodera, X. Hao, G. A. Gibson, and R. Meservey, Phys. Rev. Lett. **61**, 637 (1988).

[8] J. Sinova, S. O. Valenzuela, J. Wunderlich, C. H. Back, and T. Jungwirth, Rev. Mod. Phys. **87**, 1213 (2015).

[9] A. Manchon, H. C. Koo, J. Nitta, S. M. Frolov, and R. A. Duine, Nat. Mater. **14**, 871 (2015).

[10] Y. A. Bychkov and E. I. Rashba, J. Exp. Theor. Phys. Lett. **39**, 78 (1984).

[11] D. Stein, K. Klitzing, and G. Weimann, Phys. Rev. Lett. **51**, 130 (1983).

[12] H. Stormer, Z. Schlesinger, A. Chang, D. Tsui, A. Gossard, and W. Wiegmann,

Phys. Rev. Lett. **51**, 126 (1983).

[13] S. LaShell, B. A. McDougall, and E. Jensen, Phys. Rev. Lett. **77**, 3419 (1996).

[14] A. Varykhalov, D. Marchenko, M. R. Scholz, E. D. L. Rienks, T. K. Kim, G. Bihlmayer, J. Sánchez-Barriga, and O. Rader, Phys. Rev. Lett. **108**, 066804 (2012).

[15] P. D. C. King, R. C. Hatch, M. Bianchi, R. Ovsyannikov, C. Lupulescu, G. Landolt, B. Slomski, J. H. Dil, D. Guan, J. L. Mi, E. D. L. Rienks, J. Fink, A. Lindblad, S. Svensson, S. Bao, G. Balakrishnan, B. B. Iversen, J. Osterwalder, W. Eberhardt, F. Baumberger, and P. Hofmann, Phys. Rev. Lett. **107**, 096802 (2011).

[16] I. M. Miron, G. Gaudin, S. Auffret, B. Rodmacq, A. Schuhl, S. Pizzini, J. Vogel, and P. Gambardella, Nat. Mater. **9**, 230 (2010).

[17] I. M. Miron, K. Garello, G. Gaudin, P.-J. Zermatten, M. V Costache, S. Auffret, S. Bandiera, B. Rodmacq, A. Schuhl, and P. Gambardella, Nature **476**, 189 (2011).

[18] N. Nagaosa, J. Sinova, S. Onoda, A. H. MacDonald, and N. P. Ong, Rev. Mod. Phys. **82**, 1539 (2010).

[19] R. Karplus and J. M. Luttinger, Phys. Rev. **95**, 1154 (1954).

[20] T. Jungwirth, Q. Niu, and A. H. MacDonald, Phys. Rev. Lett. **88**, 207208 (2002).

[21] M. Onoda and N. Nagaosa, J. Phys. Soc. Japan **71**, 19 (2002).

[22] J. Wunderlich, B. Kaestner, J. Sinova, and T. Jungwirth, Phys. Rev. Lett. **94**, 047204 (2005).

[23] M. I. D'yakonov and V. I. Perel, Zh. Eksp. Teor. Fiz. **13**, 657 (1971).

[24] N. F. Mott, Proc. R. Soc. A **124**, 425 (1929).

[25] J. Hirsch, Phys. Rev. Lett. **83**, 1834 (1999).

[26] S. Zhang, Phys. Rev. Lett. **85**, 393 (2000).

[27] Y. K. Kato, R. C. Myers, A. C. Gossard, and D. D. Awschalom, Science **306**, 1910 (2004).

[28] J. Sinova, D. Culcer, Q. Niu, N. Sinitsyn, T. Jungwirth, and A. MacDonald, Phys. Rev. Lett. **92**, 126603 (2004).

[29] G. Guo, S. Murakami, T.-W. Chen, and N. Nagaosa, Phys. Rev. Lett. **100**, 096401 (2008).

[30] T. Tanaka, H. Kontani, M. Naito, T. Naito, D. Hirashima, K. Yamada, and J. Inoue, Phys. Rev. B **77**, 165117 (2008).

[31] M. Gradhand, D. V. Fedorov, P. Zahn, and I. Mertig, Phys. Rev. B **81**, 245109 (2010).

[32] B. Zimmermann, K. Chadova, D. Kodderitzsch, S. Blugel, H. Ebert, D. V. Fedorov, N. H. Long, P. Mavropoulos, I. Mertig, Y. Mokrousov, and M. Gradhand, Phys. Rev. B **90**, 220403 (2014).

[33] J. Smit, Physica **21**, 877 (1955).

[34] L. Berger, Physica **30**, 1141 (1964).

[35] P. Laczkowski, Y. Fu, H. Yang, J.-C. Rojas-Sánchez, P. Noel, V. T. Pham, G. Zahnd, C. Deranlot, S. Collin, C. Bouard, P. Warin, V. Maurel, M. Chshiev, A. Marty, J.-P. Attané, A. Fert, H. Jaffrès, L. Vila, and J.-M. George, Phys. Rev. B **96**, 140405 (2017).

[36] J. C. Slonczewski, J. Magn. Magn. Mater. **159**, L1 (1996).

[37] L. Berger, Phys. Rev. B **54**, 9353 (1996).

[38] A. Brataas, A. D. Kent, and H. Ohno, Nat. Mater. **11**, 372 (2012).

[39] E. B. Myers, D. C. Ralph, J. A. Katine, R. N. Louie, and R. A. Buhrman, Science **285**, 867 (1999).

[40] J. Katine, F. Albert, R. Buhrman, E. Myers, and D. Ralph, Phys. Rev. Lett. **84**, 3149 (2000).

[41] S. Mangin, D. Ravelosona, J. A. Katine, M. J. Carey, B. D. Terris, and E. E. Fullerton, Nat. Mater. **5**, 210 (2006).

[42] S. I. Kiselev, J. C. Sankey, I. N. Krivorotov, N. C. Emley, R. J. Schoelkopf, R. A. Buhrman, and D. C. Ralph, Nature **425**, 380 (2003).

[43] W. Rippard, M. Pufall, S. Kaka, S. Russek, and T. Silva, Phys. Rev. Lett. **92**, 027201 (2004).

[44] M. Tsoi, A. G. M. Jansen, J. Bass, W. C. Chiang, M. Seck, V. Tsoi, and P. Wyder, Phys. Rev. Lett. **80**, 4281 (1998).

[45] M. Madami, S. Bonetti, G. Consolo, S. Tacchi, G. Carlotti, G. Gubbiotti, F. B. Mancoff, M. A. Yar, and J. Åkerman, Nat. Nanotechnol. **6**, 635 (2011).

[46] L. Liu, T. Moriyama, D. C. Ralph, and R. A. Buhrman, Phys. Rev. Lett. **106**, 036601 (2011).

[47] L. Liu, C.-F. Pai, Y. Li, H. W. Tseng, D. C. Ralph, and R. A. Buhrman, Science **336**, 555 (2012).

[48] K. Garello, I. M. Miron, C. O. Avci, F. Freimuth, Y. Mokrousov, S. Blügel, S. Auffret, O. Boulle, G. Gaudin, and P. Gambardella, Nat. Nanotechnol. **8**, 587 (2013).

[49] M. Hayashi, J. Kim, M. Yamanouchi, and H. Ohno, Phys. Rev. B **89**, 144425 (2014).

[50] T. R. Mcguire and R. I. Potter, IEEE Trans. Magn. **11**, 1018 (1975).

[51] D. A. Thompson, L. T. Romankiw, and A. F. Mayadas, IEEE Trans. Magn. **11**, 1039 (1975).

[52] Y.-T. Chen, S. Takahashi, H. Nakayama, M. Althammer, S. Goennenwein, E. Saitoh, and G. Bauer, Phys. Rev. B **87**, 144411 (2013).

[53] H. Nakayama, M. Althammer, Y.-T. Chen, K. Uchida, Y. Kajiwara, D. Kikuchi, T. Ohtani, S. Geprägs, M. Opel, S. Takahashi, R. Gross, G. E. W. Bauer, S. T. B. Goennenwein, and E. Saitoh, Phys. Rev. Lett. **110**, 206601 (2013).

[54] J. Kim, P. Sheng, S. Takahashi, S. Mitani, and M. Hayashi, Phys. Rev. Lett. **116**,

097201 (2016).

[55] G. Binasch, P. Grünberg, F. Saurenbach, and W. Zinn, Phys. Rev. B **39**, 4828 (1989).

[56] M. N. Baibich, J. M. Broto, A. Fert, F. N. Van Dau, F. Petroff, P. Eitenne, G. Creuzet, A. Friederich, and J. Chazelas, Phys. Rev. Lett. **61**, 2472 (1988).

[57] W. P. Pratt, J. S.-F. Lee, J. M. Slaughter, R. Loloee, P. A. Schroeder, and J. Bass, Phys. Rev. Lett. **66**, 3060 (1991).

[58] T. Valet and A. Fert, Phys. Rev. B **48**, 7099 (1993).

[59] M. Julliere, Phys. Lett. A **54**, 225 (1975).

[60] T. Miyazaki and N. Tezuka, J. Magn. Magn. Mater. **139**, L231 (1995).

[61] J. S. Moodera, L. R. Kinder, T. M. Wong, and R. Meservey, Phys. Rev. Lett. **74**, 3273 (1995).

[62] S. Yuasa, T. Nagahama, A. Fukushima, Y. Suzuki, and K. Ando, Nat. Mater. **3**, 868 (2004).

[63] S. S. P. Parkin, C. Kaiser, A. Panchula, P. M. Rice, B. Hughes, M. Samant, and S. H. Yang, Nat. Mater. **3**, 862 (2004).

[64] S. Ikeda, J. Hayakawa, Y. Ashizawa, Y. M. Lee, K. Miura, H. Hasegawa, M. Tsunoda, F. Matsukura, and H. Ohno, Appl. Phys. Lett. **93**, 082508 (2008).

[65] P. M. Haney, H.-W. Lee, K.-J. Lee, A. Manchon, and M. D. Stiles, Phys. Rev. B **87**, 174411 (2013).

[66] A. Brataas, Y. Nazarov, and G. Bauer, Phys. Rev. Lett. **84**, 2481 (2000).

[67] Y. Tserkovnyak, A. Brataas, and G. Bauer, Phys. Rev. B **66**, 224403 (2002).

[68] Y. Tserkovnyak, A. Brataas, G. E. W. Bauer, and B. I. Halperin, Rev. Mod. Phys. **77**, 1375 (2005).

[69] K. Xia, P. J. Kelly, G. E. W. Bauer, A. Brataas, and I. Turek, Phys. Rev. B **65**, 220401 (2002).

[70] Y. Tserkovnyak, A. Brataas, and G. Bauer, Phys. Rev. Lett. **88**, 117601 (2002).

[71] C. H. Back, R. Allenspach, W. Weber, S. S. P. Parkin, D. Weller, E. L. Garwin, and H. C. Siegmann, Science (80-.). **285**, 864 (1999).

[72] S. Mizukami, Y. Ando, and T. Miyazaki, Jpn. J. Appl. Phys. **40**, 580 (2001).

[73] C.-F. Pai, Y. Ou, L. H. Vilela-Leão, D. C. Ralph, and R. A. Buhrman, Phys. Rev. B **92**, 064426 (2015).

[74] J.-C. Rojas-Sánchez, N. Reyren, P. Laczkowski, W. Savero, J.-P. Attané, C. Deranlot, M. Jamet, J.-M. George, L. Vila, and H. Jaffrès, Phys. Rev. Lett. **112**, 106602 (2014).

[75] M.-H. Nguyen, D. C. Ralph, and R. A. Buhrman, Phys. Rev. Lett. **116**, 126601 (2016).

[76] C.-F. Pai, L. Liu, Y. Li, H. W. Tseng, D. C. Ralph, and R. A. Buhrman, Appl. Phys. Lett. **101**, 122404 (2012).

[77] S. Emori, U. Bauer, S.-M. Ahn, E. Martinez, and G. S. D. Beach, Nat. Mater. **12**,

611 (2013).

[78] P. P. J. Haazen, E. Murè, J. H. Franken, R. Lavrijsen, H. J. M. Swagten, and B. Koopmans, Nat. Mater. **12**, 299 (2013).

[79] O. J. Lee, L. Q. Liu, C. F. Pai, Y. Li, H. W. Tseng, P. G. Gowtham, J. P. Park, D. C. Ralph, and R. A. Buhrman, Phys. Rev. B **89**, 024418 (2014).

[80] J. Kim, J. Sinha, S. Mitani, M. Hayashi, S. Takahashi, S. Maekawa, M. Yamanouchi, and H. Ohno, Phys. Rev. B **89**, 174424 (2014).

[81] X. Fan, H. Celik, J. Wu, C. Ni, K.-J. Lee, V. O. Lorenz, and J. Q. Xiao, Nat. Commun. **5**, 3042 (2014).

[82] J. Kim, J. Sinha, M. Hayashi, M. Yamanouchi, S. Fukami, T. Suzuki, S. Mitani, and H. Ohno, Nat. Mater. **12**, 240 (2013).

[83] T. D. Skinner, M. Wang, A. T. Hindmarch, A. W. Rushforth, A. C. Irvine, D. Heiss, H. Kurebayashi, and A. J. Ferguson, Appl. Phys. Lett. **104**, 062401 (2014).

[84] M. Kawaguchi, K. Shimamura, S. Fukami, F. Matsukura, H. Ohno, T. Moriyama, D. Chiba, and T. Ono, Appl. Phys. Express **6**, 113002 (2013).

[85] X. Fan, J. Wu, Y. Chen, M. J. Jerry, H. Zhang, and J. Q. Xiao, Nat. Commun. **4**, 1799 (2013).

[86] K. Garello, I. M. Miron, C. O. Avci, F. Freimuth, Y. Mokrousov, S. Blügel, S. Auffret, O. Boulle, G. Gaudin, and P. Gambardella, Nat. Nanotechnol. **8**, 587 (2013).

[87] X. Qiu, P. Deorani, K. Narayanapillai, K.-S. Lee, K.-J. Lee, H.-W. Lee, and H. Yang, Sci. Rep. **4**, 4491 (2014).

[88] Y. Ou, C.-F. Pai, S. Shi, D. C. Ralph, and R. A. Buhrman, Phys. Rev. B **94**, 140414 (2016).

[89] R. Ramaswamy, X. Qiu, T. Dutta, S. D. Pollard, and H. Yang, Appl. Phys. Lett. **108**, 202406 (2016).

[90] M. Hayashi, J. Kim, M. Yamanouchi, and H. Ohno, Phys. Rev. B **89**, 144425 (2014).

[91] H. X. Yang, M. Chshiev, B. Dieny, J. H. Lee, A. Manchon, and K. H. Shin, Phys. Rev. B **84**, 054401 (2011).

[92] C.-F. Pai, M.-H. Nguyen, C. Belvin, L. H. Vilela-Leão, D. C. Ralph, and R. A. Buhrman, Appl. Phys. Lett. **104**, 082407 (2014).

[93] A. Hoffmann, IEEE Trans. Magn. **49**, 5172 (2013).

[94] W. Zhang, M. B. Jungfleisch, W. Jiang, J. E. Pearson, A. Hoffmann, F. Freimuth, and Y. Mokrousov, Phys. Rev. Lett. **113**, 196602 (2014).

[95] W. Zhang, M. B. Jungfleisch, F. Freimuth, W. Jiang, J. Sklenar, J. E. Pearson, J. B. Ketterson, Y. Mokrousov, and A. Hoffmann, Phys. Rev. B **92**, 144405 (2015).

[96] V. Tshitoyan, C. Ciccarelli, A. P. Mihai, M. Ali, A. C. Irvine, T. A. Moore, T. Jungwirth, and A. J. Ferguson, Phys. Rev. B **92**, 214406 (2015).

[97] J. B. S. Mendes, R. O. Cunha, O. Alves Santos, P. R. T. Ribeiro, F. L. A. Machado,

R. L. Rodríguez-Suárez, A. Azevedo, and S. M. Rezende, Phys. Rev. B **89**, 140406 (2014).

[98] W. Zhang, W. Han, S. Yang, Y. Sun, Y. Zhang, B. Yan, and S. S. P. Parkin, Sci. Adv. **2**, e1600759 (2016).

[99] S. Fukami, C. Zhang, S. Duttagupta, A. Kurenkov, and H. Ohno, Nat. Mater. **15**, 535 (2016).

[100] V. Baltz, A. Manchon, M. Tsoi, T. Moriyama, T. Ono, and Y. Tserkovnyak, Rev. Mod. Phys. **90**, 015005 (2018).

[101] B. F. Miao, S. Y. Huang, D. Qu, and C. L. Chien, Phys. Rev. Lett. **111**, 066602 (2013).

[102] H. Wang, C. Du, P. Chris Hammel, and F. Yang, Appl. Phys. Lett. **104**, 202405 (2014).

[103] D. H. Wei, Y. Niimi, B. Gu, T. Ziman, S. Maekawa, and Y. Otani, Nat. Commun. **3**, 1058 (2012).

[104] Y. Ou, S. Shi, D. C. Ralph, and R. A. Buhrman, Phys. Rev. B **93**, 220405(R) (2016).

[105] J.-C. C. Rojas-Sánchez, N. Reyren, P. Laczkowski, W. Savero, J.-P. P. Attané, C. Deranlot, M. Jamet, J.-M. M. George, L. Vila, and H. Jaffrès, Phys. Rev. Lett. **112**, 106602 (2014).

[106] J.-U. Thiele, L. Folks, M. F. Toney, and D. K. Weller, J. Appl. Phys. **84**, 5686

(1998).

[107] K. M. Seemann, Y. Mokrousov, A. Aziz, J. Miguel, F. Kronast, W. Kuch, M. G. Blamire, A. T. Hindmarch, B. J. Hickey, I. Souza, and C. H. Marrows, Phys. Rev. Lett. **104**, 076402 (2010).

[108] G. E. Bacon, A. E. R. E. Harwell, and J. Crangle, Proc. R. Soc. London, Ser. A **272**, 387 (1963).

[109] T. Saerbeck, H. Zhu, D. Lott, H. Lee, P. R. Leclair, G. J. Mankey, A. P. J. Stampfl, and F. Klose, J. Appl. Phys. **114**, 013901 (2013).

[110] G. X. Miao and G. Xiao, Appl. Phys. Lett. **85**, 73 (2004).

[111] J. Moritz, B. Rodmacq, S. Auffret, and B. Dieny, J. Phys. D. Appl. Phys. **41**, 135001 (2008).

[112] T. Taniguchi, J. Grollier, and M. D. Stiles, Phys. Rev. Appl. **3**, 044001 (2015).

[113] Y. Ou, D. C. Ralph, and R. A. Buhrman, Phys. Rev. Lett. **120**, 097203 (2018).

[114] S. Maat, A. J. Kellock, D. Weller, J. E. E. Baglin, and E. E. Fullerton, J. Magn. Magn. Mater. **265**, 1 (2003).

[115] R. C. O'Handley, *Modern Magnetic Materials - Principles and Applications* (John Wiley & Sons, INC., 2000).

[116] See Supplementary Materials for more information. (n.d.).

[117] F. D. Czeschka, L. Dreher, M. S. Brandt, M. Weiler, M. Althammer, I.-M. Imort, G. Reiss, a. Thomas, W. Schoch, W. Limmer, H. Huebl, R. Gross, and S. T. B.

Goennenwein, Phys. Rev. Lett. **107**, 046601 (2011).

[118] L. Liu, O. J. Lee, T. J. Gudmundsen, D. C. Ralph, and R. A. Buhrman, Phys. Rev. Lett. **109**, 096602 (2012).

[119] J. Kondo, Prog. Theor. Phys. **27**, 772 (1962).

[120] J. P. Jan, Helv. Phys. Acta **25**, 677 (1952).

[121] B. Gu, T. Ziman, and S. Maekawa, Phys. Rev. B **86**, 241303 (2012).

[122] Y. Ohnuma, H. Adachi, E. Saitoh, and S. Maekawa, Phys. Rev. B **89**, 174417 (2014).

[123] Z. Qiu, J. Li, D. Hou, E. Arenholz, A. T. NDiaye, A. Tan, K. Uchida, K. Sato, S. Okamoto, Y. Tserkovnyak, Z. Q. Qiu, and E. Saitoh, Nat. Commun. **7**, 12670 (2016).

[124] L. Frangou, S. Oyarzún, S. Auffret, L. Vila, S. Gambarelli, and V. Baltz, Phys. Rev. Lett. **116**, 077203 (2016).

[125] M. T. Johnson, P. J. H. Bloemen, F. J. a Den Broeder, and J. J. De Vries, Reports Prog. Phys. **59**, 1409 (1996).

[126] B. Dieny and M. Chshiev, Rev. Mod. Phys. **89**, 025008 (2017).

[127] S. Ikeda, K. Miura, H. Yamamoto, K. Mizunuma, H. D. Gan, M. Endo, S. Kanai, J. Hayakawa, F. Matsukura, and H. Ohno, Nat. Mater. **9**, 721 (2010).

[128] D. C. Worledge, G. Hu, D. W. Abraham, J. Z. Sun, P. L. Trouilloud, J. Nowak, S. Brown, M. C. Gaidis, E. J. O'Sullivan, and R. P. Robertazzi, Appl. Phys. Lett.

98, 022501 (2011).

[129] R. Shimabukuro, K. Nakamura, T. Akiyama, and T. Ito, Phys. E **42**, 1014 (2010).

[130] T. Liu, J. W. Cai, and L. Sun, AIP Adv. **2**, 032151 (2012).

[131] J. Torrejon, J. Kim, J. Sinha, S. Mitani, M. Hayashi, M. Yamanouchi, and H. Ohno, Nat. Commun. **5**, 4655 (2014).

[132] C.-F. Pai, M. Mann, A. J. Tan, and G. S. D. Beach, Phys. Rev. B **93**, 144409 (2016).

[133] Y. Ou, D. C. Ralph, and R. A. Buhrman, Appl. Phys. Lett. **110**, 192403 (2017).

[134] L. Baumgarten, C. M. Schneider, H. Petersen, F. Schäfers, and J. Kirschner, Phys. Rev. Lett. **65**, 492 (1990).

[135] J. C. Read, P. G. Mather, and R. A. Buhrman, Appl. Phys. Lett. **90**, 132503 (2007).

[136] P. G. Gowtham, G. M. Stiehl, D. C. Ralph, and R. A. Buhrman, Phys. Rev. B **93**, 024404 (2016).

[137] J. Sinha, M. Hayashi, A. J. Kellock, S. Fukami, M. Yamanouchi, H. Sato, S. Ikeda, S. Mitani, S. Yang, S. S. P. Parkin, and H. Ohno, Appl. Phys. Lett. **102**, 242405 (2013).

[138] N. Miyakawa, D. C. Worledge, and K. Kita, IEEE Magn. Lett. **4**, 1000104 (2013).

[139] H. Meng, R. Sbiaa, C. C. Wang, S. Y. H. Lua, and M. A. K. Akhtar, J. Appl. Phys. **110**, 103915 (2011).

[140] J. Sinha, M. Gruber, M. Kodzuka, T. Ohkubo, S. Mitani, K. Hono, and M. Hayashi, J. Appl. Phys. **117**, 043913 (2015).

[141] T. Liu, J. W. Cai, and L. Sun, AIP Adv. **2**, 032151 (2012).

[142] J. Y. Bae, W. C. Lim, H. J. Kim, T. D. Lee, K. W. Kim, and T. W. Kim, J. Appl. Phys. **99**, 08T316 (2006).

[143] M. S. Gabor, C. Tiusan, T. Petrisor Jr., and T. Petrisor, IEEE Trans. Magn. **50**, 2007404 (2014).

[144] M. Konoto, H. Imamura, T. Taniguchi, K. Yakushiji, H. Kubota, A. Fukushima, K. Ando, and S. Yuasa, Appl. Phys. Express **6**, 073002 (2013).

[145] J. J. Nowak, R. P. Robertazzi, J. Z. Sun, G. Hu, J. H. Park, J. Lee, A. J. Annunziata, G. P. Lauer, R. Kothandaraman, E. J. O Sullivan, P. L. Trouilloud, Y. Kim, and D. C. Worledge, IEEE Magn. Lett. **7**, 4 (2016).

[146] G. L. Humphrey, J. Am. Chem. Soc. **75**, 2806 (1953).

[147] E. J. Huber, E. L. Head, and C. E. Holley, J. Phys. Chem. **68**, 3040 (1964).

[148] S. Shi, Y. Ou, S. V. Aradhya, D. C. Ralph, and R. A. Buhrman, Phys. Rev. Appl. **9**, 011002 (2018).

[149] S. Fukami and H. Ohno, Jpn. J. Appl. Phys **56**, 0802A1 (2017).

[150] M.-H. Nguyen, C.-F. Pai, K. X. Nguyen, D. A. Muller, D. C. Ralph, and R. A. Buhrman, Appl. Phys. Lett. **106**, 222402 (2015).

[151] J. Sun, Phys. Rev. B **62**, 570 (2000).

[152] S. V. Aradhya, G. E. Rowlands, J. Oh, D. C. Ralph, and R. A. Buhrman, Nano Lett. **16**, 5987 (2016).

[153] E. B. Myers, F. J. Albert, J. C. Sankey, E. Bonet, R. a Buhrman, and D. C. Ralph, Phys. Rev. Lett. **89**, 196801 (2002).

[154] J. Z. Sun, R. P. Robertazzi, J. Nowak, P. L. Trouilloud, G. Hu, D. W. Abraham, M. C. Gaidis, S. L. Brown, E. J. O'Sullivan, W. J. Gallagher, and D. C. Worledge, Phys. Rev. B - Condens. Matter Mater. Phys. **84**, (2011).

[155] G. E. Rowlands, S. V. Aradhya, S. Shi, E. H. Yandel, J. Oh, D. C. Ralph, and R. A. Buhrman, Appl. Phys. Lett. **110**, (2017).